



MARMARA UNIVERSITY
FACULTY OF ENGINEERING



MICROSTRUCTURE-MECHANICAL PROPERTY RELATIONSHIP IN ADDITIVELY MANUFACTURED PRODUCTS WITH ALSi10MG BASED MATERIAL

Eren ÜYÜKLÜ, Buğrahan ATAR

GRADUATION PROJECT REPORT

Department of Mechanical Engineering

Supervisor

Prof. Dr. Paşa YAYLA

ISTANBUL, 2022



MARMARA UNIVERSITY
FACULTY OF ENGINEERING



**MICROSTRUCTURE-MECHANICAL PROPERTY RELATIONSHIP
IN ADDITIVELY MANUFACTURED PRODUCTS WITH ALSI10MG
BASED MATERIAL**

by

Eren ÜYÜKLÜ, Buğrahan ATAR

June 2022, Istanbul

**SUBMITTED TO THE DEPARTMENT OF MECHANICAL ENGINEERING IN
PARTIAL FULFILLMENT OF THE REQUIREMENTS FOR THE DEGREE
OF**

BACHELOR OF SCIENCE

AT

MARMARA UNIVERSITY

The author(s) hereby grant(s) to Marmara University permission to reproduce and to distribute publicly paper and electronic copies of this document in whole or in part and declare that the prepared document does not in anyway include copying of previous work on the subject or the use of ideas, concepts, words, or structures regarding the subject without appropriate acknowledgement of the source material.

Signature of Author(s)

A handwritten signature in black ink, appearing to read 'Eren Üyüklu'.

Department of Mechanical Engineering

Certified By

A handwritten signature in blue ink, appearing to read 'Bugrahan Atar'.

Project Supervisor, Department of Mechanical Engineering

Accepted By

Head of the Department of Mechanical Engineering

ACKNOWLEDGEMENT

In the long period of time that passed between the beginning and the delivery of this thesis, there have been many people who have helped us. We would like to mention these people and express our gratitude for each and every of them.

First of all, we would like to express our greatest thanks to our supervisor Prof. Dr. Paşa YAYLA, for the valuable guidance and advice on preparing this thesis and giving us moral and material support.

This thesis is supported by TUBITAK 2209-B University Students Industry-Oriented Research Projects Support Program and Turkish Aerospace Industry Lift Up Industry Focused Undergraduate Study Completion Projects Program. We would like to express our deep sense of gratitude to TUBITAK, Turkish Aerospace Industry and from Turkish Aerospace Industry our industry supervisor Ümit AYTAR and his team.

We would like to kindly thank to Prof. Dr. Recep ARTIR and Semih GÜVEN for their work in the metallurgical laboratory and Lecturer Fatih Serdar SAYIN for scanning electron microscope observation at the Center for Nanotechnology & Biomaterials Applications and Research.

It is impossible to forget Ervo Makina, Karaçık Torna, Freze ve Borvek Atölyesi that helped to machine our test specimens, and Muhittin Hüseyin KOYUNCU for cargo transportation. Moreover, we would like to politely thank Mustafa YORTANLI from Arili Plastic for his help in applying the density test in the Arili Plastic laboratory. Lastly, we would like to express our heartfelt thanks to Yusuf ATAR, who determinately helped us to get our test specimens in the blinking of an eye.

to ATAR & ÜYÜKLÜ families

June, 2022

Eren ÜYÜKLÜ, Buğrahan ATAR

CONTENTS

ACKNOWLEDGEMENT	ii
ABSTRACT	v
SYMBOLS	vii
ABBREVIATIONS	viii
LIST OF FIGURES	x
LIST OF TABLES	xiv
1. INTRODUCTION.....	1
1.1. Aim of the Thesis.....	3
1.2. Literature Research	3
1.3. Additive Manufacturing.....	8
1.3.1. Binder jetting.....	9
1.3.2. Direct energy deposition.....	9
1.3.3. Material extrusion	10
1.3.4. Material jetting.....	10
1.3.5. Vat polymerization	11
1.3.6. Sheet lamination	11
1.3.7. Powder Bed Fusion.....	11
1.3.8. Selective laser sintering.....	11
1.3.8.1. Selective laser melting	12
1.3.8.2. Electron beam melting	13
1.3.8.3. Direct metal laser sintering	13
1.4. Micro- and Macrostructure	14
1.5. Density Measurement	21
1.6. Mechanical Tests	22
1.6.1. Charpy Impact Test.....	22
1.6.2. Tensile Test.....	24
1.6.3. Hardness Test	27
1.7. Fracture Mechanism	29
1.8. Aluminum and AlSi10Mg Alloy	39
2. MATERIAL AND METHOD.....	41
2.1. Sample Preparation	41

2.2.	Archimedes' Density Method	41
2.3.	Micro- and Macrostructure Observation.....	42
2.4.	Hardness Test.....	44
2.5.	Tensile Test.....	44
2.6.	Charpy Impact Test.....	45
3.	RESULTS AND DISCUSSION	47
3.1.	Tensile Test Results	47
3.2.	Charpy Test Results	51
3.3.	Density Measurements.....	56
3.4.	Hardness Test Results	57
3.5.	Microstructure.....	58
3.6.	Fracture Mechanics	66
4.	EVALUATION of CURRENT WORK from MUDEK PERSPECTIVE	89
4.1.	Economic Analysis	89
4.2.	Real-Life Conditions.....	89
4.3.	Producibility.....	89
4.4.	Constraints	90
5.	CONCLUSIONS and RECOMMENDATIONS for FURTHER WORKS.....	91
5.1.	Conclusions of the Current Work	91
5.2.	Recommendations for Further Works.....	93
REFERENCES.....		94

Microstructure – Mechanical Property Relationship in Additively Manufactured Products with AlSi10Mg Based Material

by

Eren ÜYÜKLÜ, Buğrahan ATAR

ABSTRACT

In this thesis, the mechanical property, fracture mechanism, and microstructure relationship of AlSi10Mg produced by laser powder bed fusion were established. Laser powder bed fusion is an additive manufacturing method that is an innovator technique. Since additive manufacturing is a new technique, utilizing materials requires studies investigating the mechanical properties, fracture mechanism, and microstructure. This is vital because these characteristics are used before choosing the materials to manufacture the desired parts.

Elasticity, plasticity, strength, toughness, brittleness, ductility, and impact were investigated for this purpose. The tensile test, the Charpy impact test, the hardness test, and the density test were applied to identify the mechanical properties of AlSi10Mg specimens. Tensile test specimens were prepared according to ISO 6892 and Charpy impact test samples were prepared according to ISO 148. After that, fracture mechanics and microstructure were observed via an optical microscope and a scanning electron microscope. Finally, these results were related to each other.

As a result of tensile, Charpy impact test results and fracture mechanisms, laser powder bed additively manufactured AlSi10Mg alloy exhibited ductile-brittle transition material. As-built additively manufactured AlSi10Mg demonstrated higher yield strength, ultimate tensile strength, microhardness but less density than as-built cast-produced AlSi10Mg.

Eklemeli İmalat ile Üretilen AlSi10Mg Bazlı Ürünlerde Mikroyapı – Mekanik Özellik İlişkisi

by
Eren ÜYÜKLÜ, Buğrahan ATAR

ÖZET

Bu tezde, toz yataktaki füzyon yöntemiyle üretilmiş AlSi10Mg合金ının, mekanik özellik, kırılma mekanizması ve mikroyapı ilişkileri kurulmuştur. Lazer toz yatak füzyon tekniği yenilikçi bir eklemeli imalat yöntemidir. Eklemeli imalat yeni bir üretim tekniği olduğundan dolayı, kullanılan malzemelerin mekanik özellik, kırılma mekanizması ve mikroyapısı araştırılmaya gereksinim duymaktadır. Bu nitelikler, istenilen parça üretimine karar verirken kullanıldığından dolayı büyük bir önem arz etmektedir.

Amacımız için elastisite, plastisite, dayanım, tokluk, gevreklik, süneklik ve darbe özelliklerini incelenmiştir. AlSi10Mg numunelerinin bu mekanik özelliklerini ortaya çıkartabilmek için, çekme testi, Charpy darbe testi, sertlik testi ve yoğunluk testi uygulandı. Çekme test numuneleri ISO 6892 standartlarına ve Charpy darbe test numuneleri ISO 148 standartlarına göre hazırlandı. Daha sonra, kırılma mekaniği ve mikroyapı, optik mikroskop ve tarayıcı elektron mikroskopu ile gözlemlendi. En sonunda da bu sonuçlar birbirleriyle ilişkilendirildi.

Çekme testi, Charpy darbe testi ve kırılma mekanizmasının sonuçlarından, lazer toz yatak füzyon eklemeli imalat ile üretilmiş AlSi10Mg合金ı hem sünek hem de gevrek bir özellik gösterdi. Eklemeli imalatla üretilmiş AlSi10Mg, dökümle üretilmiş AlSi10Mg ile kıyaslandığında daha yüksek akma mukavemetine, çekme mukavemetine, mikrosertlige ve daha az yoğunluğa sahip olduğunu gösterdi.

SYMBOLS

p : Density

W : Weight

P : Load

π : Pi number

D : Diameter

C_P : Correction factor

L : Length

E : Modulus of elasticity

m : Mass

g : Gravitational acceleration

h : Height

ABBREVIATIONS

3D	: Three Dimensional
Al	: Aluminum
AM	: Additive Manufacturing
AlSi10Mg	: Aluminum Silicon Magnesium Alloy
ASTM	: American Society for Testing and Materials
CAD	: Computer-Aided Design
DED	: Direct Energy Deposition
DIN	: Deutsches Institut für Normung
DMLS	: Direct Metal Laser Sintering
EDX	: Energy Dispersive X-Ray Analysis
FS	: Fracture Stress
HAZ	: Heat Affected Zone
HBW	: Brinell Hardness
HIP	: Hot Isostatic Pressing
HK	: Knoop Hardness
HR	: Rockwell Hardness
HV	: Vickers Hardness
ISO	: International Organization for Standardization
Mg	: Magnesium
OM	: Optical Microscope
PBF	: Powder Bed Fusion
SEM	: Scanning Electron Microscope
Si	: Silicon
SLS	: Selective Laser Sintering
SLM	: Selective Laser Melting

SR	: Stress Relieved
UTS	: Ultimate Tensile Stress
YS	: Yield Stress
GC	: Gravity Casting
HPVDC	: High Pressure Vacuum Die Casting

LIST OF FIGURES

Figure 1. 1 AM processes	9
Figure 1. 2 Selective laser melting	12
Figure 1. 3 Electron beam melting	13
Figure 1. 4 Direct metal laser sintering	14
Figure 1. 5 Microstructure of AlSi10Mg.....	15
Figure 1. 6 Inner and outer boundaries regions of AlSi10Mg.....	16
Figure 1. 7 Fine, coarse and heat effected zones of AlSi10Mg.....	16
Figure 1. 8 Heat effected zone of AlSi10Mg.....	17
Figure 1. 9 Boundary regions of AlSi10Mg	17
Figure 1. 10 Laser scans	18
Figure 1. 11 Fish scale morphology	18
Figure 1. 12 Overlapping melt pools	19
Figure 1. 13 Laser scan tracks	19
Figure 1. 14 67 Degree of scanning type of additively manufactured material	20
Figure 1. 15 Layer-by-layer morphology	20
Figure 1. 16 Fish scale morphology	21
Figure 1. 17 (a) V-Notch, (b) Keyhole-Notch, (c) U-Notch.....	23
Figure 1. 18 Position of the specimen in the (a) Izod impact test, (b) Charpy impact test	23
Figure 1. 19 Examples of Stress-Strain Graph	24
Figure 1. 20 Stress-Strain Graph of as-built and post-processed additively manufactured AlSi10Mg	25
Figure 1. 21 Most common building directions of the AM process	26
Figure 1. 22 Vickers hardness tester.....	28
Figure 1. 23 Cup and cone, ductile, and brittle fracture mechanism, respectively.....	30
Figure 1. 24 Examples of ductile and brittle fracture mechanisms	31
Figure 1. 25 Example of ductile-brittle mixed fracture mechanism	31
Figure 1. 26 Examples of fracture mechanisms (ductile, ductile-brittle combined and brittle)	32
Figure 1. 27 Cup and cone fracture mechanism	32
Figure 1. 28 OM observation of as-built additively manufactured AlSi10Mg.....	34

Figure 1. 29 OM observation of HIP processed additively manufactured AlSi10Mg	34
Figure 1. 30 SEM images of the tensile fracture surfaces for the as-built additively manufactured AlSi10Mg alloy	35
Figure 1. 31 SEM images of the tensile fracture surfaces for the HIPped additively manufactured AlSi10Mg alloy	36
Figure 1. 32 Examples of brittle and ductile mechanism at the end of Charpy impact tests	37
Figure 1. 33 OM observation of Charpy fracture surface of additively manufactured as-built AlSi10Mg.....	37
Figure 1. 34 OM observation of Charpy fracture surface of additively manufactured HIPped AlSi10Mg	37
Figure 1. 35 SEM images of the impact fracture surfaces for the as-built additively manufactured AlSi10Mg alloy	38
Figure 1. 36 SEM images of the impact fracture surfaces for the additively manufactured HIPped AlSi10Mg alloy	39
Figure 1. 37 Aluminum parts.....	40
Figure 2. 1 Density measurement device Mettler AJ100	42
Figure 2. 2 Nikon Epiphot 300	43
Figure 2. 3 Nikon SMZ1500.....	43
Figure 2. 4 Zeiss Evo Ma 10.....	44
Figure 3. 1 Stress-strain curve	47
Figure 3. 2 Ultimate tensile stress, fracture stress, yield stress and elongation graph....	48
Figure 3. 3 Average stress–strain curve.....	49
Figure 3. 4 Force-Time curves.....	51
Figure 3. 5 Energy-Time curves	52
Figure 3. 6 Energy-Time curve specimen 1.....	52
Figure 3. 7 Energy-Time curve specimen 2.....	53
Figure 3. 8 Energy-Time curve specimen 3.....	53
Figure 3. 9 Energy-Time curve specimen 4.....	54
Figure 3. 10 Energy-Time curve specimen 5.....	55
Figure 3. 11 Laser scan tracks	58
Figure 3. 12 Void-free laser scan tracks	59

Figure 3. 13 Pores on the laser scans	59
Figure 3. 14 Fish scale morphology as a result of layer-by-layer manufacturing process	60
Figure 3. 15 Magnified fish scale morphology	60
Figure 3. 16 SEM observed microstructure (1500X)	61
Figure 3. 17 SEM observed microstructure (3000X)	62
Figure 3. 18 SEM observed microstructure (5000X)	63
Figure 3. 19 SEM observed fine microstructure (15000X)	64
Figure 3. 20 SEM observed coarse microstructure (15000X)	65
Figure 3. 21 EDX (Energy Dispersive X-Ray) Analysis (800X)	66
Figure 3. 22 Specimens after tensile test	67
Figure 3. 23 Tensile specimen 3	67
Figure 3. 24 Side view of fractured part of specimen 3	68
Figure 3. 25 Top view of fractured part of specimen 3	68
Figure 3. 26 Optically observed side view of fracture surface of specimen 3	69
Figure 3. 27 Optically observed side view of fracture surface of specimen 3	69
Figure 3. 28 Optically observed top view of fracture surface of specimen 3	70
Figure 3. 29 SEM observed fracture surface of specimen 3 (42X)	70
Figure 3. 30 SEM observed fracture surface of specimen 3 (200X)	71
Figure 3. 31 SEM observed fracture surface of specimen 3 (3000X)	72
Figure 3. 32 Tensile specimen 4	73
Figure 3. 33 Side view of fractured part of specimen 4	73
Figure 3. 34 Top view of fractured part of specimen 4	74
Figure 3. 35 Optically observed side view of fracture surface of specimen 4	74
Figure 3. 36 Optically observed side view of fracture surface of specimen 4	75
Figure 3. 37 Optically observed top view of fracture surface of specimen 4	75
Figure 3. 38 SEM observed fracture surface of specimen 4 (42X)	76
Figure 3. 39 SEM observed fracture surface of specimen 4 (400X)	76
Figure 3. 40 SEM observed fracture surface of specimen 4 (3000X)	77
Figure 3. 41 Tensile specimen 5	77
Figure 3. 42 Side view of fractured part of specimen 5	78
Figure 3. 43 Optically observed side view of fracture surface of specimen 5	78

Figure 3. 44 Optically observed side view of fracture surface of specimen 5.....	79
Figure 3. 45 Optically observed top view of fracture surface of specimen 5.....	79
Figure 3. 46 SEM observed fracture surface of specimen 5 (42X)	80
Figure 3. 47 SEM observed fracture surface of specimen 5 (150X)	80
Figure 3. 48 SEM observed fracture surface of specimen 5 (3000X)	81
Figure 3. 49 Charpy Impact Tested Specimens	81
Figure 3. 50 Optically observed side view of Charpy specimen 1	82
Figure 3. 51 Optically observed top view of Charpy specimen 1	82
Figure 3. 52 SEM observed fracture surface of Charpy specimen 1 (41X)	83
Figure 3. 53 SEM observed fracture surface of Charpy specimen 1 (200X)	83
Figure 3. 54 Optically observed side view of Charpy specimen 2	84
Figure 3. 55 SEM observed fracture surface of Charpy specimen 2 (42X)	84
Figure 3. 56 SEM observed fracture surface of Charpy specimen 2 (200X)	85
Figure 3. 57 SEM observed fracture surface of Charpy specimen 2 (3000X)	86
Figure 3. 58 Optically observed top view of Charpy specimen 2	87
Figure 3. 59 Optically observed side view of Charpy specimen 3	87
Figure 3. 60 Optically observed top view of Charpy specimen 3	88
Figure 4. 1 Total weight of specimens	90

LIST OF TABLES

Table 1. 1 Impact Energy of AlSi10Mg	24
Table 1. 2 HBW for SLM AlSi10Mg	29
Table 1. 3 Vickers Hardness Number for SLM AlSi10Mg	29
Table 2. 1 Chemical composition of the AlSi10Mg Powder	41
Table 3. 1 Tensile Test Results	50
Table 3. 2 Charpy Impact Test Results.....	56
Table 3. 3 Vickers microhardness analysis.....	57
Table 3. 4 EDX Analysis	65
Table 4. 1 Expenses	89

1. INTRODUCTION

Additive manufacturing (AM) is a promising manufacturing method. It has many advantages which conventional methods do not have. These advantages can be listed as follows: material and molding savings (almost zero material waste), rapid prototyping, production of complex shapes with the unrivalled design of freedom, high geometrical accuracy, low weight, as well as reduction of expensive tools. However, conventional methods are material, energy, and time-consuming. Moreover, geometrically complex parts that can be fabricated in AM cannot be produced by conventional methods. For those reasons, AM is widely used in the aerospace and automotive industries [1] [2] [3] [4].

AM methods, according to the American Society for Testing Materials, are divided into seven groups: powder bed fusion (PBF), directed energy deposition (DED), sheet lamination, binder jetting, material extrusion, material jetting, and vat polymerization. The first four of them are involved in metal processing. Metal processing with AM is generally used with different kinds of alloys such as titanium, stainless steel, nickel, and aluminum (Al) alloys [1] [5].

One of the main methods of AM is PBF, which includes the melting and sintering process with different sources such as laser, electron, and heat. In this technique, powder materials are placed on a platform in layers. Every layer is fused by a laser source on the necessary lines. This procedure goes on until acquiring the final part [6].

Al alloys are highly preferred in AM since they have beneficial properties such as low density, lightweight, high strength, superior corrosion resistance, machinability, and high thermal and electrical conductivity. In particular, AlSi10Mg alloys are primarily used and fit with laser PBF. Casting and welding processes can be applied to these alloys because of their eutectic Al-Si microstructure. Also, age hardening can be applied with the presence of Magnesium (Mg). These are the reasons why AlSi10Mg alloys are preferred for producing technologically complex and economically sustainable parts. Hence, they are seen in automobiles, ships, submarines, aeronautics, and space largely [2] [4] [7].

The processing of Al alloys with AM, nevertheless, has challenges that can be classified into two parts: powder-related and process-induced problems. Due to the high reflection

of the laser beam from the surface of Al powders, the high heat transfer rate as a result of high thermal conductivity and low infrared absorption requires higher laser power. Additionally, inclusions in the powder and the high reactivity of Al with oxygen can be attributed to powder-related issues. Porosity, lack of fusion, and epitaxial growth of grains can be attributed to process-induced challenges. These problems affect the mechanical properties of the AlSi10Mg alloys. To deal with challenges and to improve mechanical properties, processing parameters such as hatching distance, scanning speed, the orientation of the building, and the temperature of the building are changed/parametrized and post-heat treatment methods such as hot isostatic pressing (HIP), T6, and T5 are applied to the fabricated AM parts [3] [8].

Mechanical properties are influenced by bond forces between atoms and the microstructure. Therefore, mechanical properties can be improved with the change of microstructure. Primarily, elasticity, plasticity, strength, hardness, toughness, brittleness, ductility, fatigue, creep, stiffness, and impact identify mechanical properties of materials. Mechanical tests provide an unveiling of these properties. These test methods are classified into two groups due to loading types: static load and dynamic load. If the applied force remains constant, it is called a "static load." Otherwise, it is called dynamic load. Mechanical tests under static load are tensile, compression, bending, torsion, hardness, and creep tests. On the other hand, under dynamic load, applied tests are fatigue and Charpy impact tests.

Microstructure is a structural foundation that can be investigated by microscopes. Generally, optical microscopes (OM), scanning electron microscopes (SEM), and electron backscattered diffraction (EBSD) are used for this purpose. The microstructure of a material directly affects the mechanical and physical properties of materials such as strength, hardness, fatigue, porosity, and toughness. Material qualification and the checking of fatigue resistance are vital in the aerospace industry. Many failures in aircraft exist because of fatigue behavior. The microstructure of as-built AM AlSi10Mg alloys, due to rapid cooling and solidification, contains fine networks of Si particles. The microstructure of the AM-produced parts, when compared to the casting process, differs from the cast-produced ones. Due to slow cooling, relatively coarser Si particles appear in contrast to the ultra-fast cooling of the AM process. The ultrafine microstructure determines higher hardness and tensile strength [3] [4] [8].

1.1. Aim of the Thesis

The importance of AM has been increasing due to its ability to eliminate the limits of design. Primarily, it will take an important place in the future with improving technology. There are various materials that can be used with AM. They can be listed as Al alloys, titanium alloys, steels, polymers, and ceramics. Since AM is a modern technique, these materials are required to investigate microstructure and mechanical properties to obtain the best material characterization.

The aim of this thesis is to investigate the microstructure, mechanical properties, and fracture mechanism of an AM AlSi10Mg alloy produced by laser PBF. Within the scope of the thesis, tensile tests, Charpy tests, density tests, and hardness tests are applied. Also, microstructure and fracture surfaces are observed with OM and SEM. At the end of the report, microstructure and how it affects mechanical properties are concluded. This is the main compass of the paper.

1.2. Literature Research

Many studies have been conducted to investigate the microstructure and mechanical properties of AlSi10Mg manufactured using the laser PBF process.

Annalisa Pola et al. studied the heat treatment effects of direct metal laser sintered (DMLS) and cast them in terms of microstructure hardness, density, and tensile properties. T6 was selected as a heat treatment method with different solution temperatures in the range of 1 to 9 hours (480, 510, 540) and different ageing temperatures (160, 180). The optimum performance of heat-treated samples for both AM and casting processes was 540 °C after 1 h, 65 °C water quenching, and 2 h ageing at 180 °C with a 2 percent density decrement. With the optimum solution of heat treatment, yield strengths were comparable with the AM but the ultimate tensile strengths were largely diminished. Furthermore, in terms of elongation, the AM was still the highest one and the casting the last one [1].

Onur Ertuğrul et al. studied the effects of stress-relieved (SR), T6, HIP, and HIP+T6 with different ageing times on additively manufactured (direct metal laser sintering) AlSi10Mg samples in terms of microstructure, mechanical properties, and fracture mechanism. To analyze pore diameter, pore area, circularity, and inner porosity, two software packages

were used. The T6-only applied samples (4 h aged) showed the highest inner porosity, while the HIPed-only samples had the lowest inner porosity percentage. This was what was expected because HIP tends to close inner porosities. Also, the increment of pore volume is attributed to entrapped gas enlargement during the heat treatment process. There was no significant change in relative density between the SR, HIP, and HIP+aged samples, while T6-only samples showed the lowest density due to the presence of higher pores. While HIP has an ability to close inner porosity, it slightly increased the surface porosity, but thanks to additional heat treatment, such an effect was diminished. Additionally, SR samples were the lowest, and T6-only samples showed the highest surface porosity. Besides, the microstructure of samples verifies the aforementioned structure of pores. In terms of hardness, the hardest sample was HIP+4h aged with a 5.8% decrement in elongation with respect to SR ones, which means the material is no longer ductile, and the softest one was HIP. Compared to T6-only with SR ones, yield strength for T6-only increases due to precipitation hardening, but tensile strength and ductility are lower than SR ones due to higher amounts of surface porosity and bigger inner pores. Furthermore, as it is compared with HIP+4h aged with T6-only, the positive effect of tensile and yield strength is attributed to the HIP that affects pore size and volume. In all tests, HIP+12h was selected to demonstrate the over-ageing zone [3].

M.M. Attallah et al. investigated the effects of post-processing heat treatments (HIP and/or T6), powder recycling, machining, and build orientation on additively manufactured (SLM) samples in terms of macro- and microstructure, voids, mechanical properties, and fractography on additively manufactured (SLM) samples of voids created by using recycled powder was higher than the new powder due to moisture present during the recycling process. Also, voids in the longitudinal section were higher than in the cross-section as AM is a layer-wise process. AlFeSi precipitated in T6 only samples that strengthened, but the rate of strength was less than round Si precipitation. They discovered that horizontally oriented samples have greater tensile and yield strengths than vertically oriented samples. Besides, HIP+T6 has higher strength than T6-only and as-fabricated samples, and that is attributed to the collapsing voids of the HIP process. Furthermore, machined samples showed more positive effects on UTS, YS, and strain than un-machined ones. Oxide layers were present on the void surfaces, and HIPping was

not able to remove oxide layers but collapse them. Irregularly shaped voids in T6-only samples disappeared in the HIP process [4].

M. Haghshenas et al. investigated the effect of the different cooling rates by utilizing different kinds of cooling media, which are water quenched, furnace cooled, and air-cooled after solutionizing for 2 hours at a temperature of 540 C. In that study, for cast and additively manufactured (SLM) parts microstructure, mechanical properties such as hardness, indentation depth and stress, plasticity index, and wear resistance are examined. After heat treating, in both AM and cast samples, the size of Si particles is coarsened, but the size of Si particles is bigger than AM due to the initial finer structure of additively manufactured parts. Moreover, by using the electron backscatter diffraction (EBSD) method, it is seen that there is no difference in the texture of the SLM AlSi10Mg. FC samples have the softest material hardness because they have the slowest cooling rate. Also, indentation depth and hardness, plasticity index is the highest and wear resistance is the lowest for the furnace-cooled samples, both in additively manufactured and cast processes. On the other hand, SLM and WQ-cast parts are found to be the hardest [8].

R.K. Everett et al. studied the microstructure and mechanical properties of special AlSi10Mg parts produced with laser PBF by using spatial data analysis. The AlSi10Mg parts were autocorrelated regarding grain size, modulus, and strengths. They used variograms for spatial data analysis and applied micro tensile tests. As a result of this study, they found spherical ranges for ultimate and yield strengths. Also, mechanical properties and microstructure are considerably impacted by local geometry [9].

Brandl et al. examined the microstructure, fatigue, and fracture behavior of AlSi10Mg that is produced by selective laser melting and then machined. They considered the building direction and heat treatment effects. They announced that the microstructure appeared to be a cellular dendritic structure of -Al and the Si particles as interdendritic. After T6 heat treatment, Si particles seemed globular, and the microstructure was not anisotropic. On the other hand, fatigue resistance strongly depends on building direction. They applied bending, tension, and compression tests to investigate mechanical properties. They demonstrated that the fatigue limit highly correlates with static tensile strength [10].

Y. Zhou, F. Ning, P. Zhang et al. analyzed the curvature effects on microstructure, mechanical, and surface properties of the AlSi10Mg parts manufactured by laser PBF. They applied tensile tests based on the ASTM E8 standard. In conclusion, they proved that the surface quality and dimension of the grain increase as the curvature increases. When considering the mechanical property, they observed the optimized failure positions at the highest curvatures [11].

L. Zhou et al. compared the microstructure and hardness of selective laser melted and cast AlSi10Mg as-built and after T6 solution heat treatment. The microstructure of as-cast AlSi10Mg was observed as α -Al particles in dendritic structure and α -Al + Si eutectic lamellar. After T6 solution heat treatment, Si particles became spheroidized. The Vickers hardness test proved that the hardness of as-cast is lower than T6 heat-treated AlSi10Mg. On the other hand, they showed selective laser melted characteristics as follows: As-built patterns of selectively laser melted AlSi10Mg, the Si peaks are very small. This means that most of the Si particles were highly saturated. The Si peaks increased until 2 hours after the heat treatment. After that, there was not any change. As-built additively manufactured AlSi10Mg includes a columnar pattern and a fish scale pattern, respectively, in transverse and longitudinal cross-sections. They also investigated the grain and cell structure via transmission electron microscopy. All grains were observed as Al cells, and Si particles were very thin. After the solution heat treatment, Si particles get coarsened. That's why the columnar and fish scale structures do not exist anymore. It is observed that cell borders within the grain disappeared via transmission electron microscopy. The highest and lowest hardness value is shown respectively in as-built AlSi10Mg and after 1 hour of the heat treatment, respectively [12].

J. Wu et al. observed the microstructure and strength of selectively laser melted AlSi10Mg using scanning electron microscopy, transmission electron microscopy, and scanning electron microscopy. The microstructure includes columnar and equiaxed grains. However, columnar grains are much larger than equiaxed grains. That's why they focused on columnar grains, which consist of long cells. It also encompasses a cell-like structure. This cell-like structure is the cross-section of long cells. They unveiled the reason why selectively laser melted AlSi10Mg has high strength. It is because of the fineness of the eutectic Al-Si structure and the cells consisting of Si [13].

X. Liu et al. used EBSD, an OM, and a SEM to investigate the effects of laser power on the microstructure of AlSi10Mg produced by selective laser melting. They observed columnar and equiaxed grains. Regarding electron backscattered diffraction observations, melt pool and equiaxed grains are visible due to extended grains. They proved that the grain size is meager at low laser power compared to higher laser powers. Three different temperature areas appeared, which are higher than the liquidus temperature, between the liquidus and solidus temperature, and lower than the solidus temperature due to the application of the laser. In the first temperature area, powder converted to solid from liquid, and delicate areas were observed. The second temperature zone material was semi-solid, and the zones were coarser. In the final temperature zone, Si particles became bigger [14].

M. Liu et al. examined how microstructure, defects, and mechanical properties are affected by different layer thicknesses while keeping the other processing parameters the same. They demonstrated how changes in relative density with different layer thicknesses. The eutectic Al-Si particles remained the same, and a dendritic coarser microstructure was observed for all thicknesses. Columnar grain characteristics change due to different layer thicknesses. Tensile tests were applied in accordance with ISO 6892 (International Organization for Standardization) standards. They showed how the tensile property changes due to layer thickness. In the conclusion of their study, the tensile property was seen in a V-shaped, which means that it first decreased and then increased due to increasing layer thickness [15].

X. Lin and N. Kang et al. investigated the microstructure, mechanical properties, and fracture mechanism of additively manufactured (SLM) AlSi10Mg alloy at elevated temperatures. Test temperatures were 25, 100, 200, 300, and 400. The high strength of additively manufactured parts is attributed to three fundamental concepts: grain boundary strengthening due to alloy element presence, solid solution strengthening, and dislocation strengthening. According to this definition, the yield strength of additively manufactured parts is the sum of grain boundary strengthening, dislocation strengthening, solid solution strengthening, and Orowan strengthening. From heated at 100 °C and 200 °C for 0.5 h, the microstructure almost did not change. After heating at 300 °C for 0.5 h, Si particles precipitated and coarsened. That effect was more visible at 400 °C for 0.5 h. An inverse

proportion was detected between yield strength and temperature. Also, the fracture mechanism from the brittle-ductile fracture is converted into a ductile fracture [16].

Nachum Frage et al. investigated the effect of post-process heat treatments on micro- and macrostructure, fatigue life, and fractography. The additively manufactured (SLM) samples were subjected to stress relief for 2 hours, HIP at 250 °C for 2 hours, and HIP at 500 °C for 2 hours. In terms of yield stress (YS), fracture stress (FS), and hardness, the as-built sample showed the highest strength, while SR+ HIP at 500 °C for 2 h is the lowest. The elevated temperature of HIP demonstrated that it is smaller in size but higher in some pores, a ductile type of fractography with relatively deep and larger pores. S-N was demonstrated thanks to the rotating-beam machine, as well as stress the intensity factor was estimated and compared with the literature [17].

1.3. Additive Manufacturing

AM is an innovative manufacturing method that is called by different names, such as 3D (three dimensional) printing, direct digital manufacturing, and rapid prototyping. Firstly, it appeared in 1987 using the source of a laser. Generally, metals, thermoplastics, ceramics, and biochemical materials are used in 3D printing. All the AM methods begin with the CAD (computer aided design) model. Then, it is converted to the .STL format. After that, the model is prepared for printing. This occurs by setting the model and cutting, assigning supports (in some methods), and applying HIP or heat treatment. AM methods are classified into seven categories regarding ISO/ASTM 52900 (American Society for Testing and Materials) as shown in Figure 1.1.

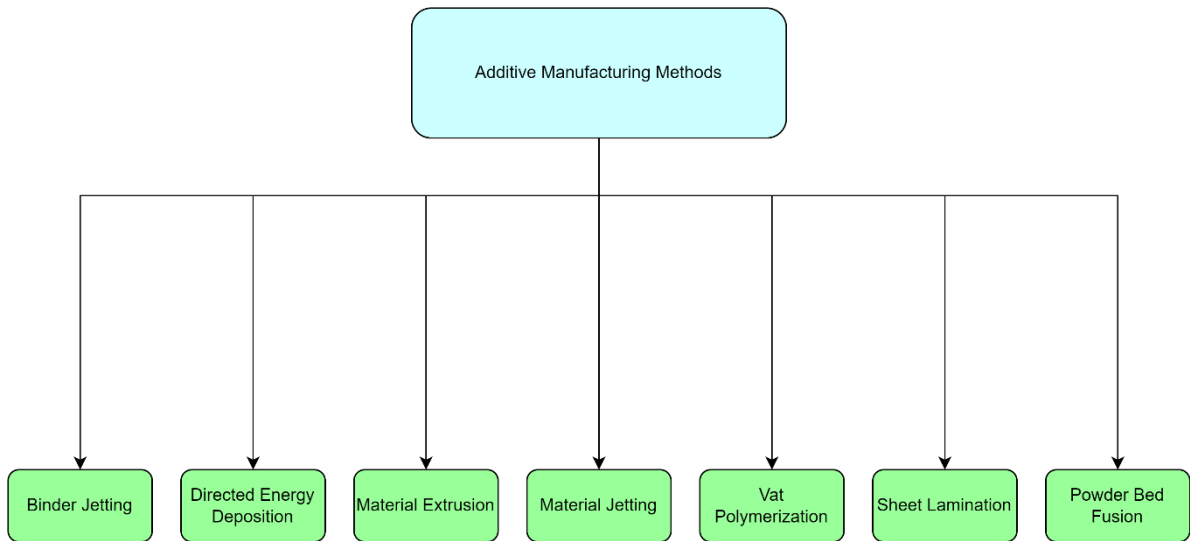


Figure 1. 1 AM processes

1.3.1. Binder jetting

The binder jetting method is also called inkjet. Powder material and a binder are used in this AM type. The binder supplies the adhesiveness between the material and the layers. The powder is laid on the building platform. The inkjet printhead moves through the x and y axes to create a layer. After completing a layer, the platform is moved down. Then, the other layer of powder is laid over the last layer. This process is repeated until the final part is acquired. Unlike other types of AM, there is no need to heat. Metals, composites, or ceramics are used in this 3D printing technique.

Binder jetted parts can have various colors, but their geometrical shape is limited.

1.3.2. Direct energy deposition

Direct energy deposition (DED) includes two types of deposition, which powder and wire deposition. The manufacturing process occurred as follows. Crude metal is melted to the desired points with the deposition of a laser or electron beam source. It can be fed by wire or powder, and the process is named due to the feeding material. After melting the desired line, a new layer is added and melted on demand trace. This operation goes on until the part is created. As an energy source, a laser is used in powder deposition-based rapid prototyping techniques. In this method, primarily metals are used as material types. It is advantageous for producing complex geometrical shapes and small parts. It is classified into four different processes. They are direct laser fabrication, laser AM, direct metal

deposition, and laser engineered net shaping. Entirely, they have the same initial deposition process that occurs in the liquid metal pool. The difference is about adjusting the atmosphere in a glove box. In laser engineered net shaping and direct laser fabrication methods, deposition happens with controlled air in the glove box. On the other hand, the wire deposition-based technique is very efficient in producing larger components and high accuracy parts. The energy source can be a laser, an electron beam, or an arc-based wire. In terms of surface finish, microstructure, and deposition rates, W.U.H. Syed et al. [18] compared wire feeding and powder feeding-based deposition AM methods. In their study, nearly identical microstructural specimens took place for both methods. In powder deposition components, some porosity was observed. The wire-based deposition method showed less consistent surface finish and deposition efficiency than powder-feeding.

1.3.3. Material extrusion

Material extrusion is also known as fused deposition modeling. It uses a polymer filament fed into the desired line by extruding a nozzle or an orifice. Heating and depositing play an essential role in this process. It provides production parts with complex geometrical shapes. Polymers, plastics, and thermoplastics are widely produced via this method. It has some advantages, such as being cost-effective and time-saving. This technique is the most reliable and low-cost 3D printing technique for thermoplastic materials [19]. On the other hand, there are some disadvantages to the thickness of the layer and surface properties. That's why studies focused on improving the surface quality of the parts that are acquired by material extrusion. Ashutosh Kumar Gupta, Krishnanand and M. Taufik investigated how important the process parameters and post-processing impacts are on surface properties [20].

1.3.4. Material jetting

Material jetting can be called poly-jet printing. The droplets of the material are deposited via UV light onto the desired area. Plastics and polymers are widely used. The main benefits of this method are high-quality mechanical and surface properties. To acquire these benefits, setting the building direction and orientation is vital. S. Tyagi, A. Yadav, and S. Deshmukh showed the importance of building direction and orientation on mechanical and surface properties [21].

1.3.5. Vat polymerization

The vat polymerization process contains ultraviolet light which converts liquid polymers into solid phases. The process is called photopolymerization. Polymers and plastics primarily take place. The benefits are good surface roughness, high geometrical accuracy, and a fast process. This process is investigated in three different methods: stereolithography, digital light processing, and masked stereolithography. In stereolithography, a laser source provides an occurring photopolymerization process. On the other hand, digital light processing has a laser beam technology to apply photopolymerization. It gives better printing properties than the other vat polymerization methods. Masked stereolithography contains a light-emitting diode for the light source and a liquid crystal display to give shape to the light.

1.3.6. Sheet lamination

Sheet lamination comprises two different manufacturing processes that are laminated objects and ultrasonic rapid prototyping. The first commercialized 3D printing method is laminated object manufacturing. In this method, paper and adhesive take place. The adhesive provides high strength for the material. A4 papers are layer by layer laminated with a laser source. Besides, ultrasonic AM utilizes metal sheets that are ultrasonically welded to each other. The general advantages are that they are economical and practical material handling. Moreover, the cutting speed is very high, so it is a time saver. Paper and sheet metal are commonly used in this AM type.

Since we used the PBF AM technique, it will be examined in detail.

1.3.7. Powder Bed Fusion

The PBF process is implemented in four different methods: selective laser sintering (SLS), selective laser melting (SLM), electron beam melting (EBM), and DMLS. The laser PBF (L-PBF) contains SLS and SLM since the laser is used as an energy source.

1.3.7.1. Selective laser sintering

The commercialization of the PBF process began with SLS. The procedure for this method is as follows: Firstly, powder layers are spread on the build area using a roller. The temperature of the powder is lower than the melting point of the material, and the

process occurs in a chamber containing nitrogen gas to make the oxidation as limited as possibly. The laser sinters powders in the desired direction. Then, a new powder layer is spread with the roller. This procedure goes on until acquiring the final part [22]. Polymers are widely utilized.

SLS offers qualified mechanical properties. However, partial surfaces include porosity. This porosity can be eliminated by some processes, such as HIP.

1.3.7.2. Selective laser melting

The SLM procedure is very similar to SLS. Unlike SLS, powders are melted and fused. The high melting point and the transition from ductile to brittle are significant properties to make the production practical. Alloys of steel, nickel, titanium, and Al are seen in this method. Al alloys and selective laser melting are perfect couples. Because of this fact, these alloys offer lightweight, low laser absorptivity, and high thermal conductivity.

The final parts can have very complex shapes and excellent mechanical force capability. On the other hand, the roughness of the surfaces is high; that's why they need post-processing.

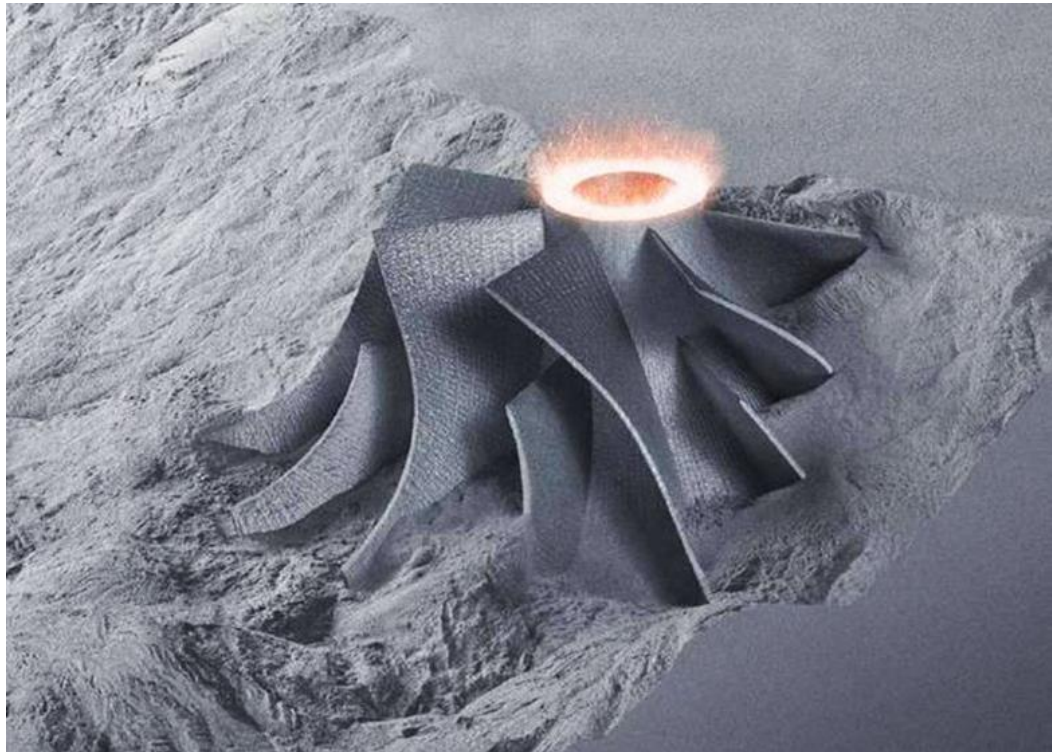


Figure 1. 2 Selective laser melting [50]

1.3.7.3. Electron beam melting

The EBM is a PBF method that uses an electron beam to fuse material particles. This technique utilizes a process that is quite like selective laser melting since they both melt powders. The difference is the energy source. Metal alloys are primarily seen in this AM type. In general, Ti-6Al-4V and Ti-48Al alloys are preferred.

EBM has significant productivity and cost-cutting advantages. Nonetheless, it has some limitations regarding surface properties and available material usage. Therefore, post-processing techniques are beneficial for surface quality.

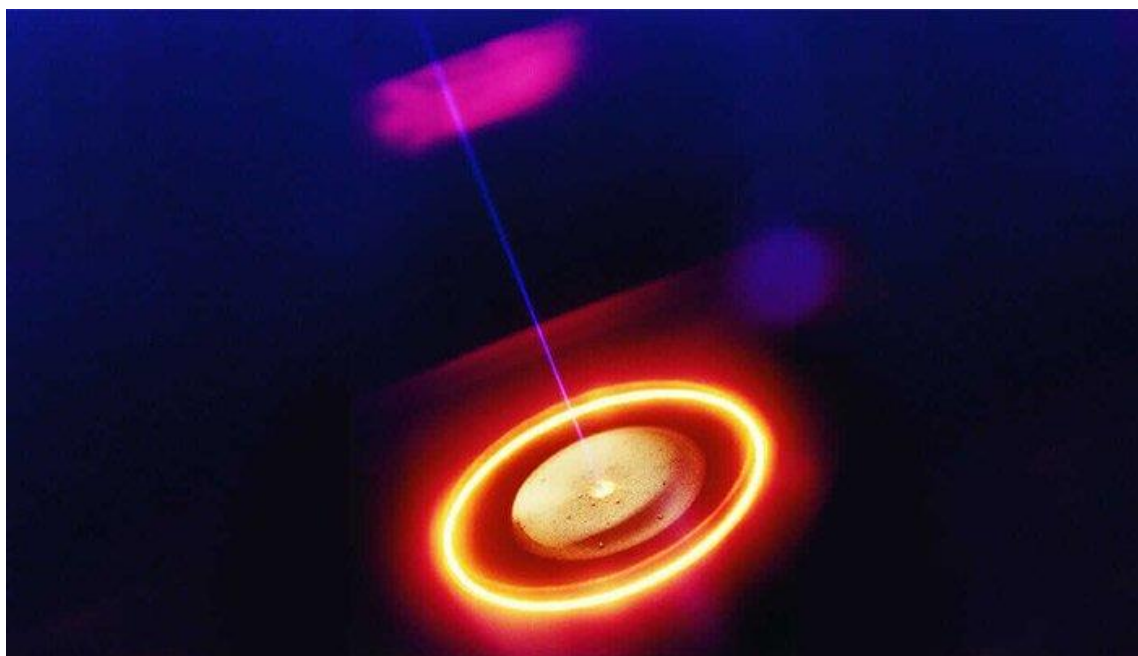


Figure 1. 3 Electron beam melting [23]

1.3.7.4. Direct metal laser sintering

DMLS offers the ability to produce metal parts with a 3D computer model. During the process, heat and pressure are used. Al and titanium alloys are manufactured via DMLS.

The main advantages of this method are designing complex shapes, and less manufacturing time. In all directions, the last parts have good mechanical properties. Unsintered metal powders can be reused. On the other hand, this method has some drawbacks that are porous parts. The other disadvantage is not being able to produce large parts.



Figure 1. 4 Direct metal laser sintering [51]

1.4. Micro- and Macrostructure

Examination of a structure consists of two main subjects: microstructure and macrostructure examination, respectively. According to the ANSI-AWS A3.0-2001, micro-examination is defined as a metallographic examination where a prepared surface is examined at high magnification, however, macro-examination is to examine a prepared surface at low or no magnification [24]. Therefore, in microstructural observation grains can be easily seen with microscopes, whilst macrostructure used to be familiar with the profile of a prepared surface.

Microstructure is a paramount subject that governs mechanical properties of any material such as tensile strength, hardness, elongation, hardness also fatigue strength. Additively manufactured AlSi10Mg parts have ultrafine microstructure characterized by dendritic cellular a-Al phase and fibrous Si particles compared to cast-produced AlSi10Mg counterparts. The extremely fine microstructure is a result of rapid solidification that is an inherent property of the additively manufacturing process. Ultrafine microstructure means a high volume of grain boundaries that promotes to able to hinder dislocation motion.

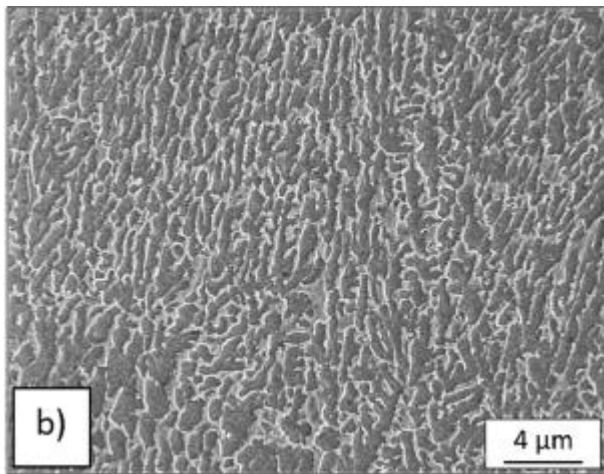


Figure 1. 5 Microstructure of AlSi10Mg [1]

Microstructure is dependent on production parameters such as building plate temperature, energy density, layer thickness and can be easily altered. Moreover, sometimes the geometry of a particular part can affect the microstructure, different geometry can have different microstructures [25].

Layer-wise process intrinsically adds a new layer on the top of former layers. At the end of each layer, both previous and new ones are melted and solidified together that creating unique micro and macrostructure [26], [27]. Moreover, with step-by-step layering technique material is reheated the heating process has an effect similar to artificial ageing, as a result, Mg₂Si precipitation is encouraged, and strength is increased [1]. However, the fast-melting process can be a starting point that induces faults such as pores and channels [26]. Also, different local thermal histories and temperature distribution around the molten pools cause microstructural heterogeneity. Heterogeneity is characterized by α-Al dendrites [2], [16]. Furthermore, due to its building process additively manufactured parts have high residual stresses.

When microstructure of additively manufactured AlSi10Mg is observed, three main areas are seen: fine fusion cellular structure, relatively coarse fusion zone, although the sample mainly shows fine microstructure, and heat affected zone (HAZ), respectively. Pool borders where multiple thermal cycles take place has coarser microstructure. Relatively globular pores are observed in the fine regions, however, in coarse regions relatively small pores which are probably formed as a result of shrinkage during solidification [17].

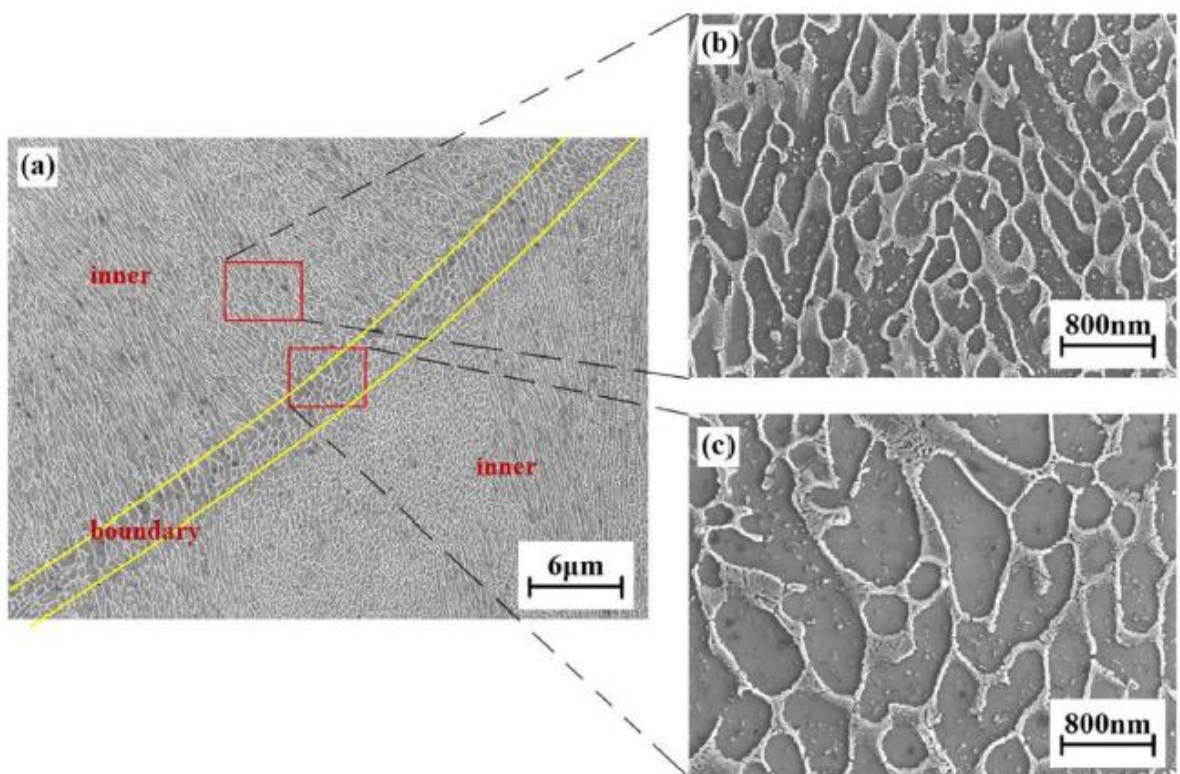


Figure 1.6 Inner and outer boundaries regions of AlSi10Mg [16]

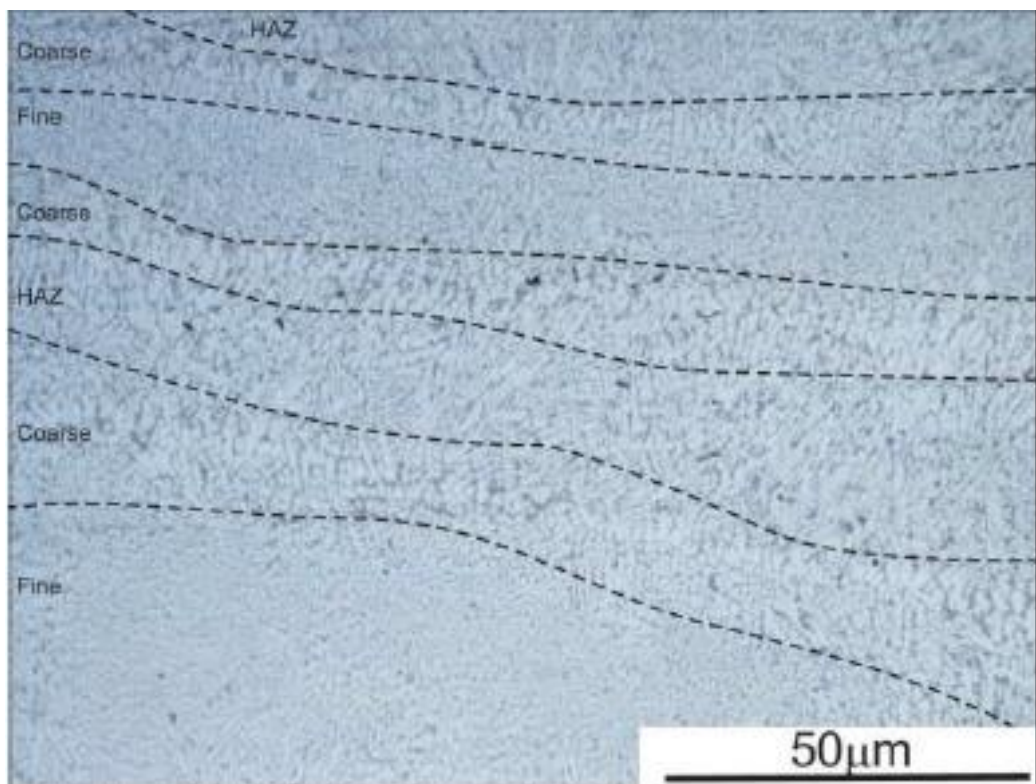


Figure 1.7 Fine, coarse and heat effected zones of AlSi10Mg [25]

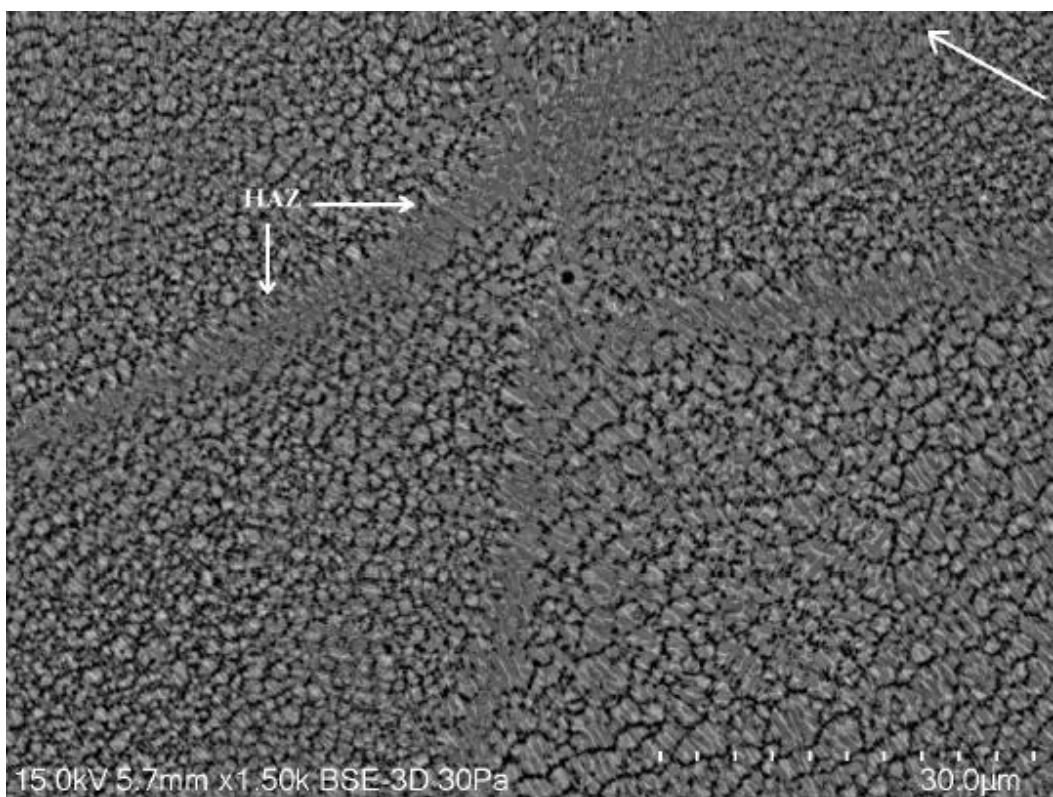


Figure 1. 8 Heat effected zone of AlSi10Mg [25]

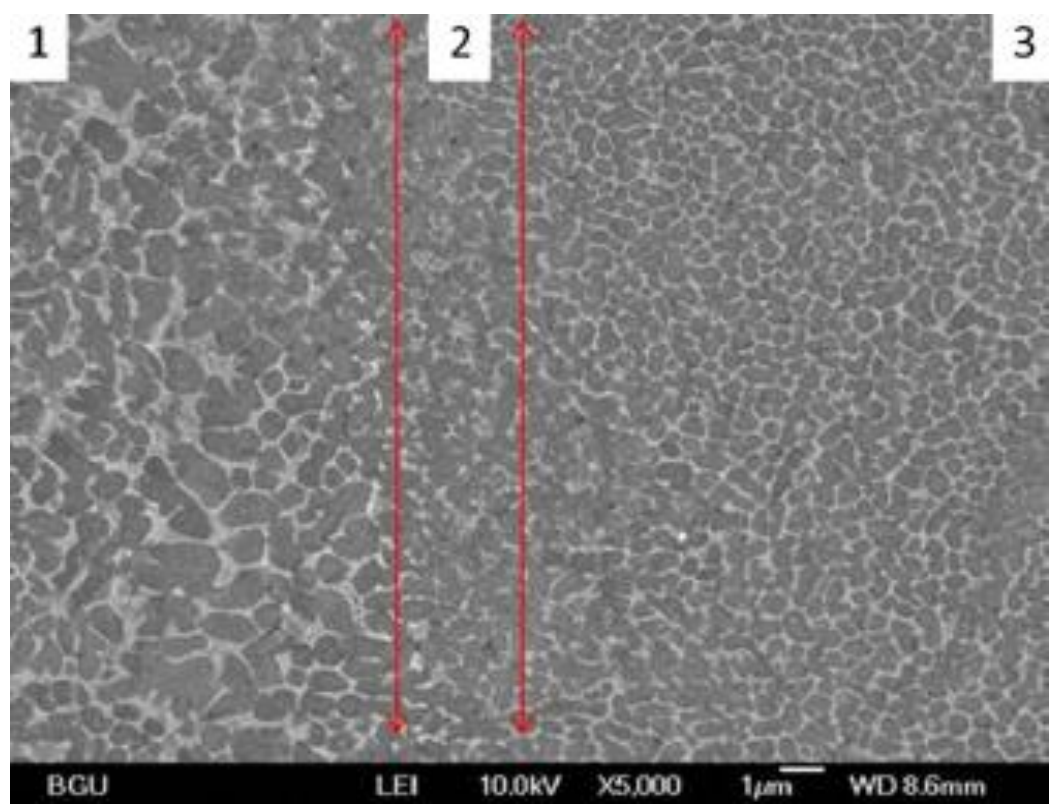


Figure 1. 9 Boundary regions of AlSi10Mg [26]

When macrostructure of additively manufactured AlSi10Mg is observed, top view shows the ellipsoid shape of laser tracks showing variation in different layers and side view demonstrates the half-cylindrical shape of overlapping melt pools, in other words, fish scale, morphology. Different kinds of observations are shown in the below figures.

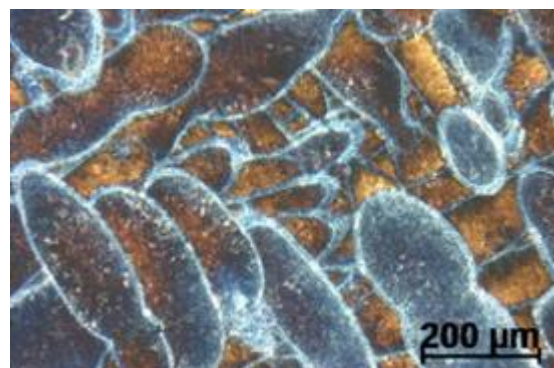


Figure 1. 10 Laser scans [4]

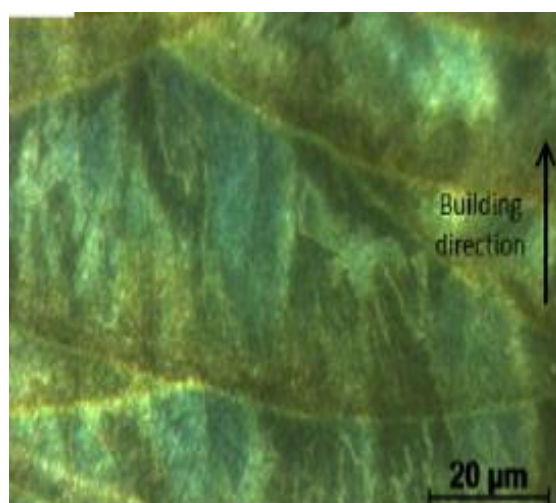


Figure 1. 11 Fish scale morphology [4]

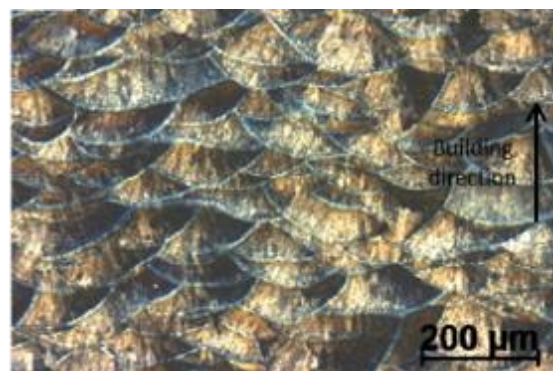


Figure 1. 12 Overlapping melt pools [4]

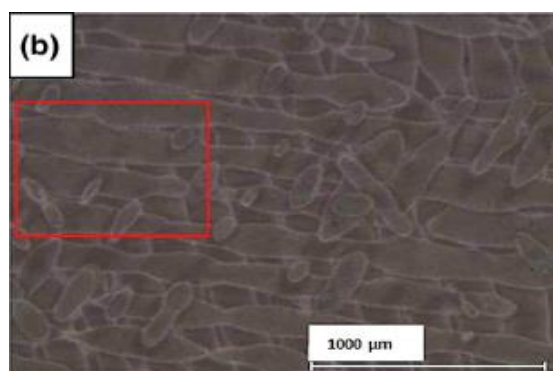


Figure 1. 13 Laser scan tracks [26]

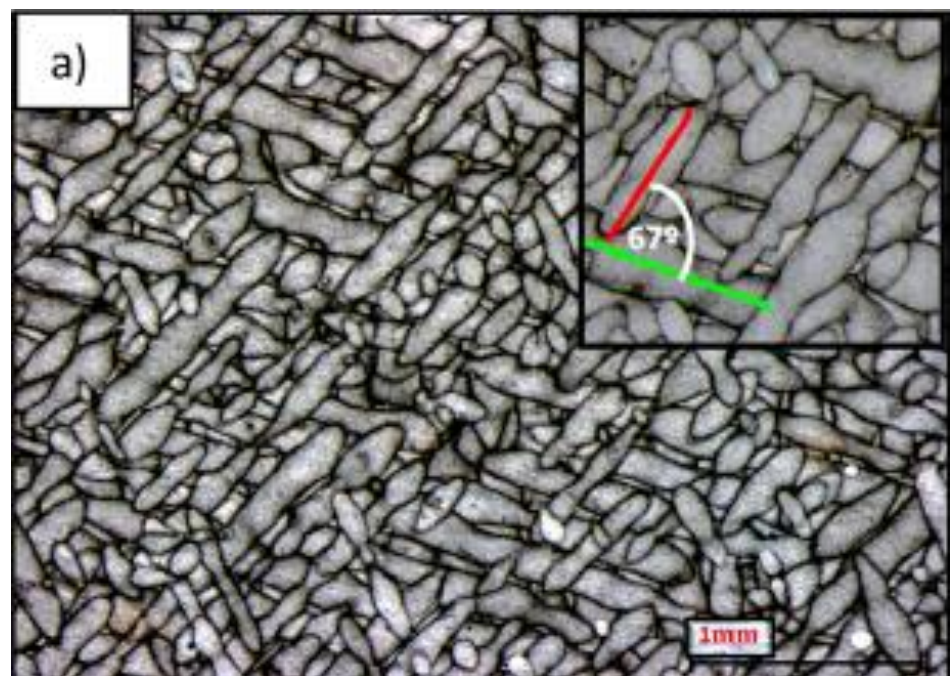


Figure 1. 14 67 Degree of scanning type of additively manufactured material [27]

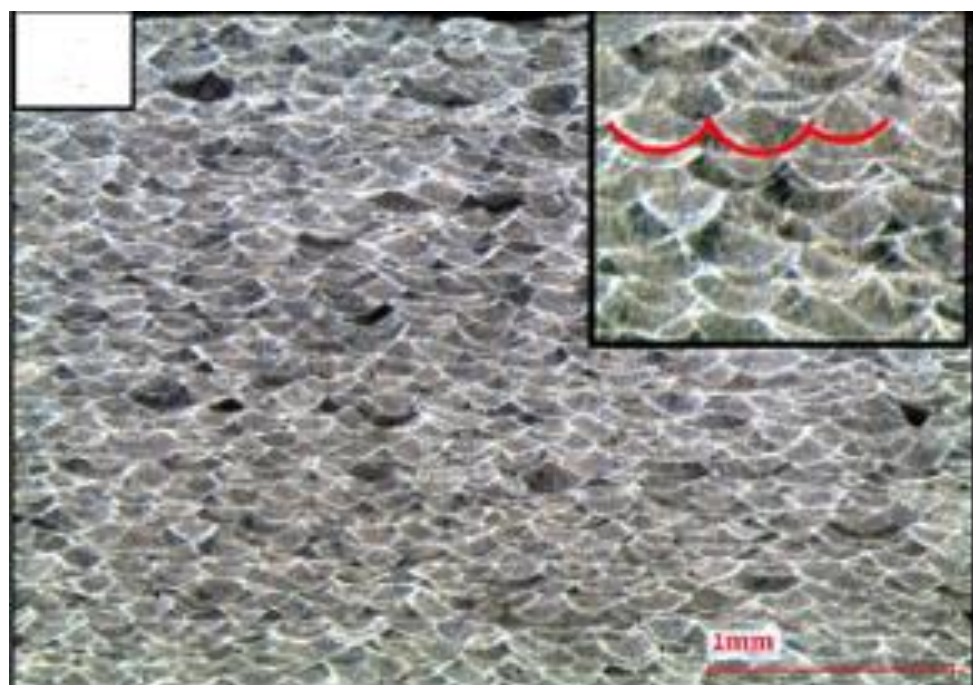


Figure 1. 15 Layer-by-layer morphology [27]

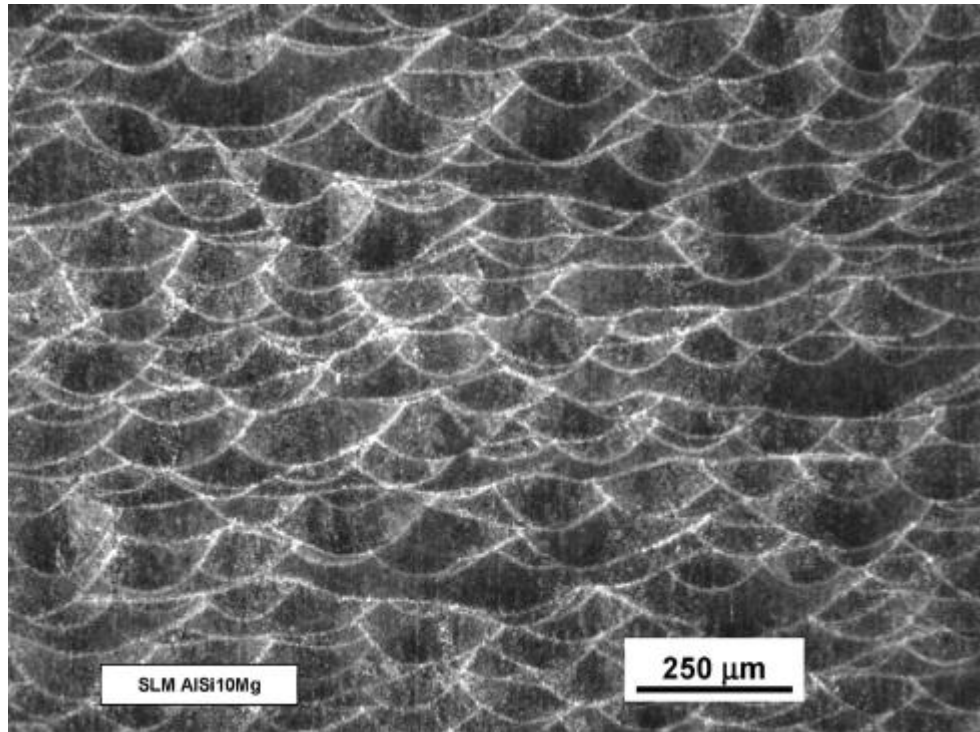


Figure 1. 16 Fish scale morphology [8]

The location of the starting point for the fracture is attributed to the microstructure, but when it comes to fracture mechanism, the macrostructure plays a more dominant role. [27] If microstructure is controlled, as a result, mechanical properties are controlled. Since AlSi10Mg is heat treatable alloy, usually heat treatment effects are used to control it.

1.5. Density Measurement

Density is a characteristic property of a material. Due to its light density and excellent mechanical properties, AlSi10Mg is preferred. The density of a material has an essential effect to understand porosity level, in other words, the results of density measurements are used for determining porosity level. Because of this reason, the concept of relative density is used. Higher relative density points lesser porosity level. For applications that require high mechanical property, and thus minimal porosity level, higher relative density is fundamental [1].

In the literature [1], [2], [28], [17], [25], [26] density measurements were performed by Archimedes' method with suitable holding and weigh scale systems. As stated by Archimedes, immersed body in a fluid subjected to buoyancy force which is an upward direction, is equal to the weight of displaced fluid. At this method, both in pure water and

in air samples were weighted. Then, by using the equation below, the density of a sample is calculated.

$$\text{Buoyancy Force} = W_{air} - W_{water} = \text{Weight of the displacement liquid}$$

$$\rho_{sample} = \rho_{water} \cdot \frac{W_{air}}{W_{air} - W_{water}} = \rho_{water} \cdot \frac{W_{air}}{\text{Buoyancy Force}}$$

Also, in the literature, [1], [26], [25], [17], [28] the density of additively manufactured AlSi10Mg is approximately taken as 2.7 g/cm³. According to recently published studies, the density of additively manufactured AlSi10Mg is increased by the laser power parameter [28]. Also, the density of AM AlSi10Mg decreases with temperature, although the density of cast AlSi10Mg does not significantly change with heat treatment processes. This is attributed to a side effect of the AM process, the growth of hydrogen porosities. However, due to the limited presence of hydrogen porosities related to casting density, this was not affected significantly.

1.6. Mechanical Tests

1.6.1. Charpy Impact Test

The Charpy impact test is one of the under dynamic load test procedures. It was invented by George Charpy in 1900 [29]. It is used to verify how much energy material absorbs during fracture. The absorbed energy is a measurement of the toughness of the material. The other purpose of this test is examining the relationship between the material ductility and brittleness. The procedure of this test can be listed as follows. Firstly, a sample is prepared regarding standards. The prepared sample is placed on the supports. Then, the hammer is raised, released, and apply a sudden force on the material, respectively. After that, a notch is created on the material. The most general notch shapes are U-notch and V-notch. Rarely, notch also can be a form of keyhole.

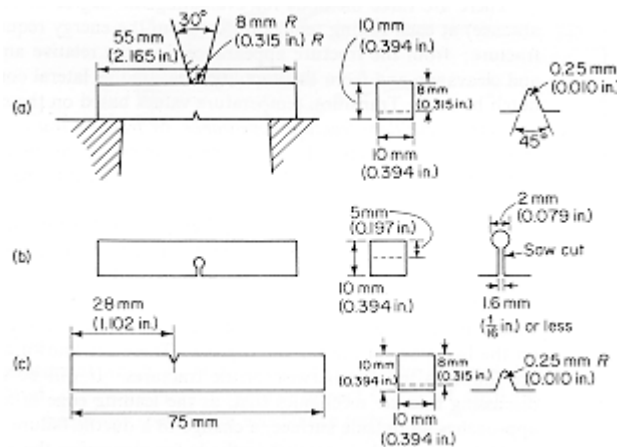


Figure 1. 17 (a) V-Notch, (b) Keyhole-Notch, (c) U-Notch [30]

There is also another impact test method called the Izod impact strength test. English engineer Edwin Gilbert Izod expressed this test in 1903. Both impact tests follow the same procedure and have the same aim. The main difference between the Izod impact test and the Charpy impact test is the arrangement of the material on the supports. In the Izod impact test, the specimen is placed vertically. On the other hand, the specimen is positioned horizontally in the Charpy impact test.

Some studies investigated that impact energy is changed regarding applied heat treatment for selectively laser melted AlSi10Mg. The highest impact energy is seen with HIP at 500 °C treatment, typical T5 at 300 °C, as-built, and modified T5 at 200 °C, as shown in Table 1.1. [27]. Despite a change in microstructure, T6 heat treatment does not affect impact energy [31]. The as-produced AlSi10Mg showed more peak force than cast AlSi10Mg [32].

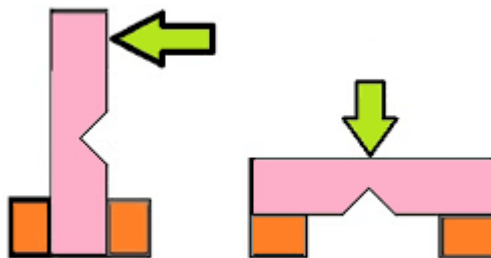


Figure 1. 18 Position of the specimen in the (a) Izod impact test, (b) Charpy impact test

Table 1. 1 Impact Energy of AlSi10Mg

	As-built	Modified T5 - 200°C	Typical T5- 300°C	HIP-500°C
Impact Energy (J)	4 ± 1	2 ± 1	7 ± 1	20 ± 1

1.6.2. Tensile Test

Tensile testing is a destructive process giving information about the mechanical properties such as modulus of elasticity, strain, yield strength, ultimate tensile strength, FS, fracture strain, resilience, and toughness. Necessary parameters, for example, dimensions and shapes, and test procedures to conduct a tensile test are identified by ASTM, ISO, and DIN (Deutsches Institut für Normung) standards. As samples are prepared, using gripping ends, a sample is connected to the test machine. Then, defining strain rate, force is applied until the test sample breaks; during that time, force, and elongation are recorded simultaneously, forming a stress-strain curve [33], [34], [35], [36].

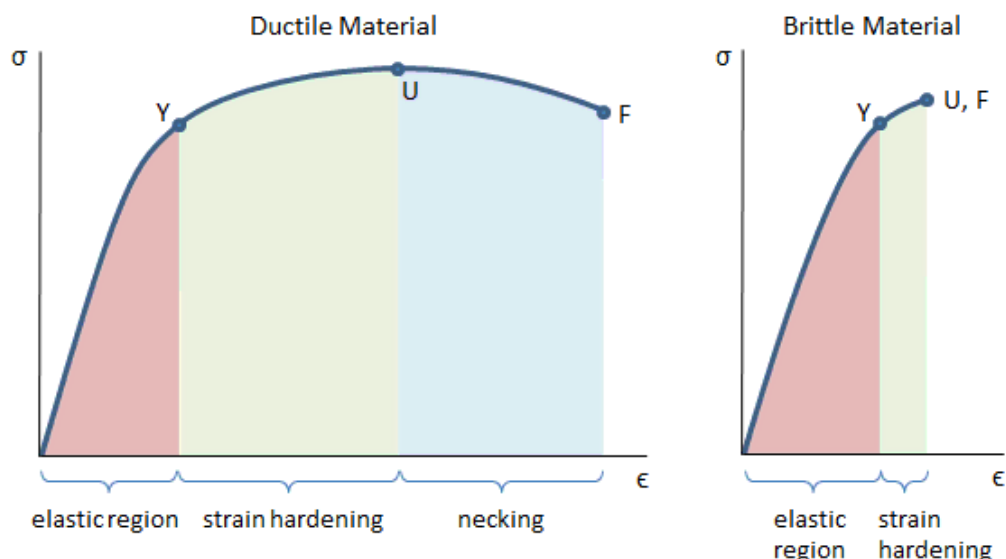


Figure 1. 19 Examples of Stress-Strain Graph [37]

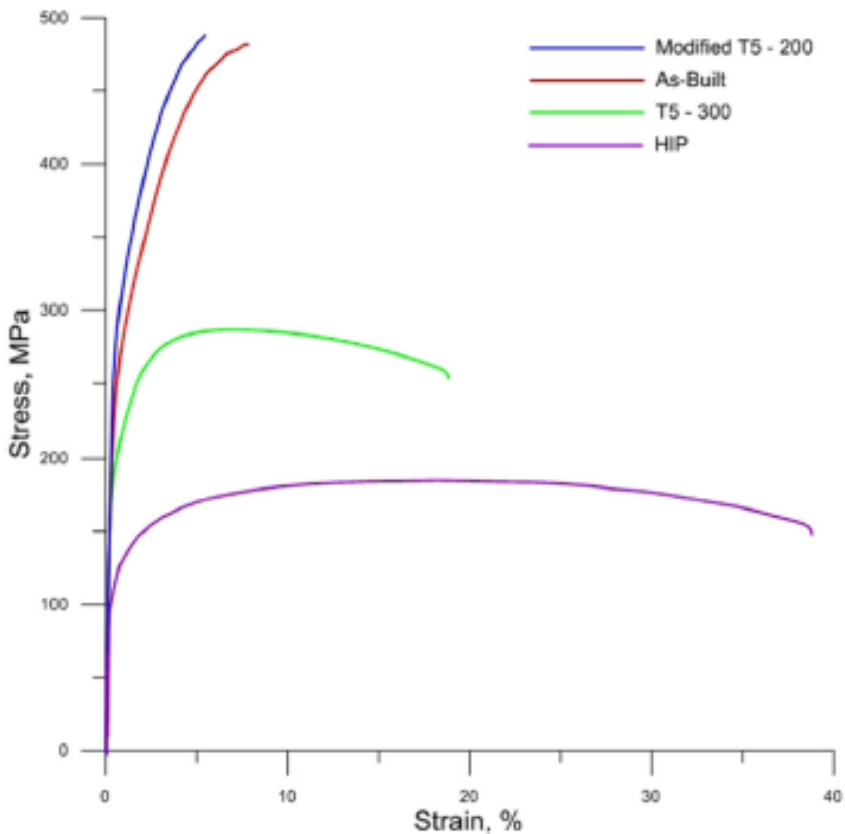


Figure 1. 20 Stress-Strain Graph of as-built and post-processed additively manufactured AlSi10Mg [27]

Mechanical properties found thanks to the tensile test are directly dependent on the ultrafine microstructure of additively manufactured AlSi10Mg, which is defined by α -Al phase and fibrous Si particles. Therefore, researchers investigate tensile properties in which treatments are applied to samples. For example, properties of building directions are examined. The most common built angles are 0° (parallel specimen) and 90° (horizontal specimen). It is found that [25], [26] and [1] horizontal specimens exhibit higher elongation than vertical ones. Also, [1] stated that horizontally produced AM samples exhibit higher tensile properties. Not only the effect of build direction but also heat treatments have been investigated by recent research. It is stated that T6 does not affect the yield strength but leads to a significant decrement in ultimate tensile strength [1]. Since HIP treatment is conducted at very high-temperature, unique macro- and microstructures are erased, and then the yield strength of the sample is significantly reduced [27]. Also, yield strengths of T5 heat-treated samples are lower compared to the as-built AM [25], [27]. However, modified T5 heat-treated samples showed higher yield

strength and ultimate tensile strength. In the consideration of recent studies, yield strength and ultimate tensile strength of the as-built additively manufactured AlSi10Mg material exhibited 240-320 MPa and 450-470 MPa, respectively [27], [25], [17], [16].

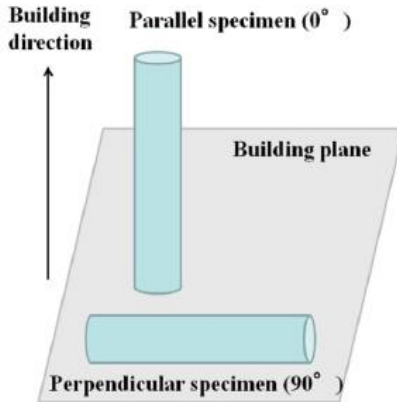


Figure 1. 21 Most common building directions of the AM process [25]

Tensile tests not only give information about the tensile strength but also the modulus of elasticity, and elongation. As-built sample modulus of elasticity is calculated at 65-75 GPa in the literature [27], [25], [17], [16], [26]. Elongation significantly increases after the HIP process. However, modified T5 heat treatment samples exhibit lower elongation than AB.

Additionally, tensile properties are significantly affected by the porosity level of a sample [28]. Melt pool boundaries, intragranular cell boundaries, and grain boundaries affect tensile properties [25]. Some studies show the effect of reinforced graphene content on the tensile and yield strength of AM AlSi10Mg. Also, the strength of a material can be increased by cold working and strain hardening.

Additively manufactured AlSi10Mg, compared to gravity cast AlSi10Mg, exhibits higher tensile strength, and elongation. In contrast to the AM process, with heat treatment methods, gravity cast samples demonstrate higher tensile strength and hardness. However, irrespective of heat treatment methods, cast samples showed very brittle-like behavior [25].

1.6.3. Hardness Test

Hardness is a mechanical property of materials that measure their resistance to plastic deformation. It is related to other mechanical properties such as ductility, brittleness, elasticity, plasticity, strain, and strength of materials. There are two groups to test the hardness, which are macro hardness and microhardness. Macro hardness is measured by the Rockwell hardness test (HR), and Brinell hardness number (HBW). On the other hand, microhardness is determined by Knoop hardness (HK) and Vickers hardness tests (HV).

The Rockwell hardness test is a well-known test method that gives more precise results than the other test methods. It is applied regarding to the ASTM E-18 standard. It is essential to clean the material and indenter. The surface of the material must be straight and perpendicular to the penetrator for indenting material with the penetrator of the machine.

The Brinell hardness test is widely utilized to investigate the hardness of materials such as metals and alloys. Generally, the known diameter of the steel ball is used with a specific force to measure hardness. The diameter of the indenter D (mm), the diameter of indentation d (mm), and the applied load (kN), hence BHN is calculated by the following equation:

$$BHN = \frac{2P}{\pi D(D - \sqrt{D^2 - d^2})}$$

The Vickers hardness test allows measuring the hardness of all metals. A load is applied to get an indentation by using the diamond indenter. The occurring depth determines the value of hardness for the material. This method can be utilized for both microhardness and macro hardness.



Figure 1. 22 Vickers hardness tester [52]

HK is utilized to determine the microhardness of fragile materials. A diamond indenter supplies an application of a load to the material on a point. HK is calculated by the following equation with a known load P, correction factor C_P, and the length of indentation L:

$$HK = \frac{P}{C_P L^2}$$

There are studies investigating the microhardness and macro hardness. The as-built SLM AlSi10Mg has higher hardness value by comparing to cast AlSi10Mg. Also, Brinell hardness values are acquired regarding to some post-processes as follows [32]:

Table 1. 2 HBW for SLM AlSi10Mg

Hardness (HBW)	
As – Built	125 ± 1
Annealed	87 ± 1
T6	104 ± 1
HIP ₅₀	79 ± 1
HIP ₅₀ + T6	99 ± 2
HIP ₁₅₀	83 ± 1
HIP ₁₅₀ + T6	111 ± 1

As seen above the table, post-processes directly affect the hardness value of AlSi10Mg. All the post-processes decreased the HBW. The hardest part is as-built AlSi10Mg, according to studies by M. Giovagnoli et al. This is also the conclusion that hardness depends on the fine microstructure and ductility of the material. P. Wei et al. demonstrated that the hardness of selectively laser melted AlSi10Mg is critically developed by fine microstructure and that it is also harder than cast AlSi10Mg [38].

On the other hand, the microhardness value is improved by modified T5 heat treatment at 200 °C as a result of Vickers tests. After the T5 heat treatment, the best microhardness value is shown from the as-built alloy [27].

Table 1. 3 Vickers Hardness Number for SLM AlSi10Mg
Hardness (HV)

As – Built	125 ± 5
T5 - 200 °C	132 ± 5
T5 - 300 °C	110 ± 5
HIP - 500 °C	60 ± 5

Moreover, the as-built SLM AlSi10Mg showed the highest hardness value comparing to solution heat treatment with 30 minutes, 1 hour, 2 hours, and 4 hours [12]. YS increases as hardness increases [8]. Hardness increases as graphene is added to the material and it is not impacted by laser power variation to process parameter [28].

1.7. Fracture Mechanism

Fracture, namely, depends on the separation process between layers with traces of track segments which is originating from the scanning of the laser. Morphology of fracture is

characterized by the mode of cracks propagation and origin location of cracks. Through the weak points, fracture originates and propagates. Typically, a fracture advances in three levels, crack initiation of the surface, planar crack propagation and catastrophic final fracture. The morphology of fracture surfaces was investigated to clarify the origin of crack formation and fracture surface propagation [27], [17].

In failure analysis, the below steps are considered [39].

- Observation with a naked eye of failed parts
- Non-destructive tests
- Mechanical tests

with the following procedure:

- Macroscopic and microscopic investigation and analysis
- Metallographic specimen preparation and investigation of these samples
- Determination of failure mechanism
- Fracture mechanism analysis

Fracture mechanism, as it is aforementioned, can be observed on macro and microscale. In microscale mainly observed with SEM that can scan 20000 times magnified surfaces.

Mainly, there are two types of fractures: brittle and ductile fractures. Brittle fractures are characterized by no or little plastic deformation. On the other hand, ductile fracture involves plastic deformation.

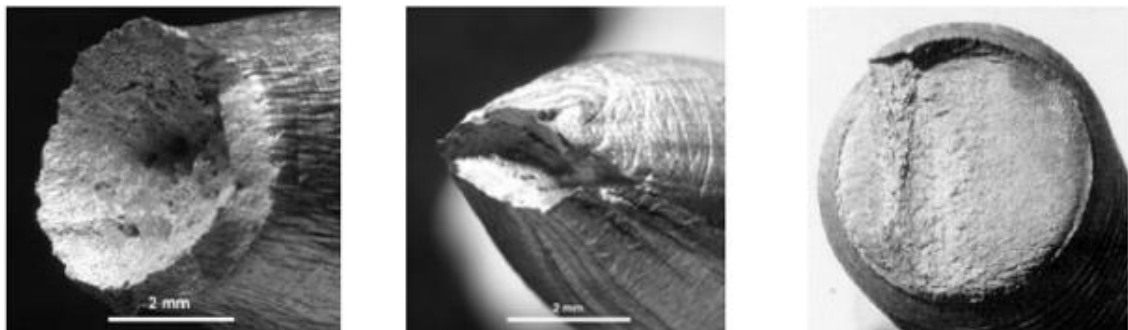


Figure 1. 23 Cup and cone, ductile, and brittle fracture mechanism, respectively [55]



Figure 1. 24 Examples of ductile and brittle fracture mechanisms [56]

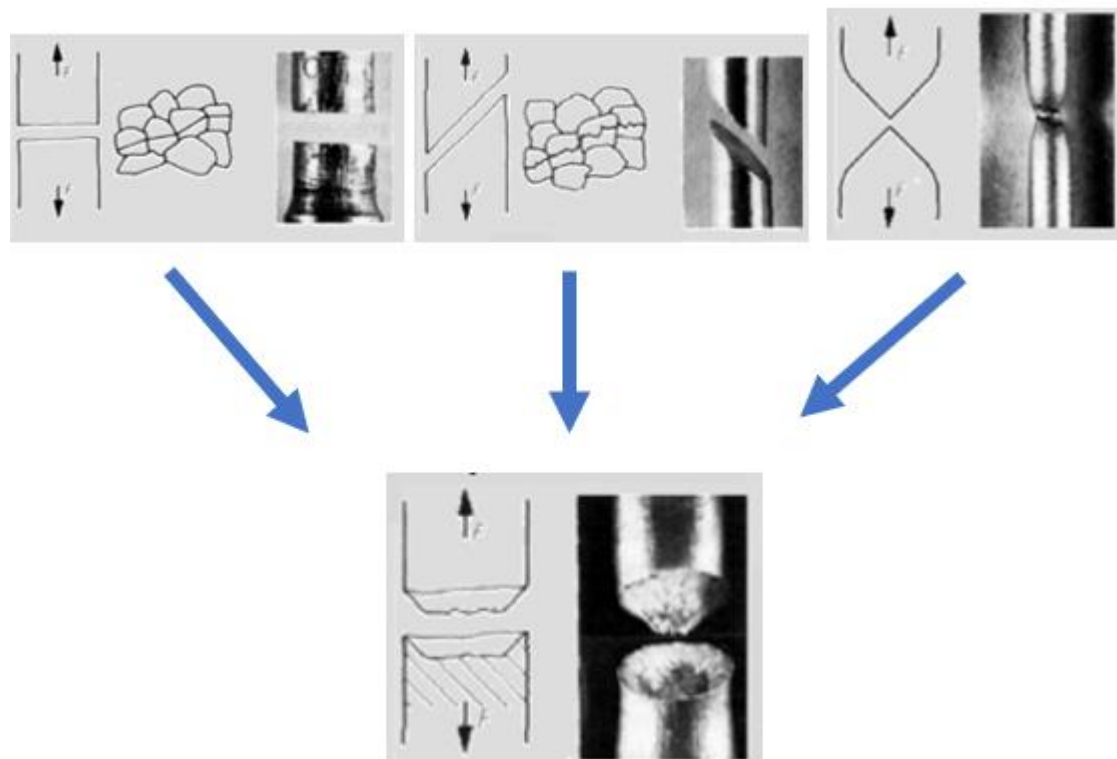


Figure 1. 25 Example of ductile-brittle mixed fracture mechanism [55]

Structural aerospace metals are usually failed by ductile fracture processes including a certain amount of elongation. Commonly, brittle fractures are undesirable because it occurs without warning and may cause catastrophic results, however for ductile fractures, failures take time with the presence of plastic deformation and absorb large amounts of energy. Also, in a ductile manner, fractures commonly take place as a result of microvoid coalescence while brittle ones have cleavage fractures characterized by intergranular crack propagation. Furthermore, in SEM observation, ductile fractures exhibit small but deep samples and, brittle fractures demonstrate relatively large but shallow samples.

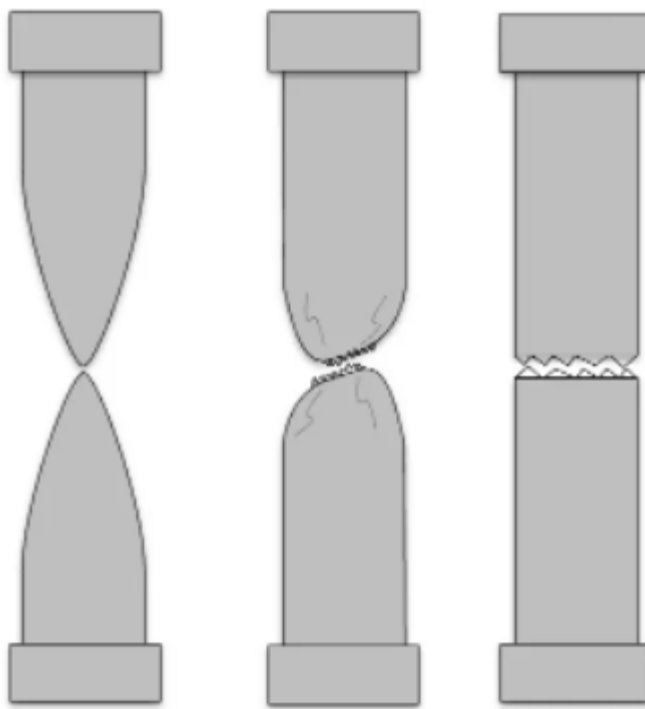


Figure 1.26 Examples of fracture mechanisms (ductile, ductile-brittle combined and brittle) [57]

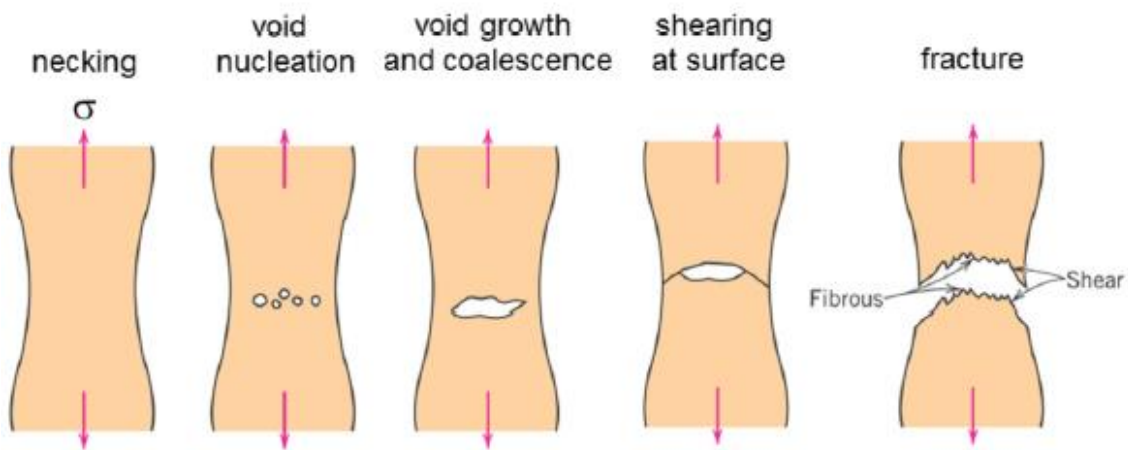


Figure 1.27 Cup and cone fracture mechanism [58]

A fracture can be affected both microstructure and macrostructure. However, according to [27], starting fracture locations are governed by microstructure and fracture mechanisms are dominantly directed by the macrostructure. Also, it should be noted that irrespective of post-process conditions, fracture mode never changes entirely. It is based on micro-void coalescence and dimples.

In the literature, fracture mechanism is mainly observed on tensile specimens with less investigation of Charpy test. In both observations for tensile and Charpy tests, there are common points. Si particles show importance since their number and size affect the fracture mechanism. Because fine Si particles hinder dislocation motion, dislocations concentrate around Si particles and cause stress concentration. Pores mainly nucleate around Si particles, by decohesion of the particle-matrix interface or by particle fracture, and because of plastic straining of the surrounding Al matrix pores grow. It is assumed that the as-fabricated samples fail along with the dendrite cell network, where the fracture initiates due to the higher hardness of the Si enriched network and its reduced ductility compared to the Al enriched cells. Therefore, it is extensively reported that fractures preferentially use the eutectic Si path which is more brittle than the Al matrix. In other words, the bigger size of Si particles could be crucial for the lifetime of the AM AlSi10Mg [1] [4] [16] [27].

When tensile specimens are observed, short and discontinuous track segments are seen. Also, relatively large but shallow dimples represent low ductility and high strength of the material. As it is forementioned, the separation process of layers could be resulted in less elongation or more elongation, depending on the strength of a material. If the material has higher strength, visible and shorter track segments are seen. Also, oxide layers which are observed on the as-built void surfaces are shown after the fractured tensile samples. However, tensile fracture surfaces show varying morphology with respect to different kinds of post-process. For example, the HIP treatment process erases micro and macrostructure, resulting in huge and deep dimples with coarsening Si particles, which is correlated with low stress and high elongation conditions. As a result, HIPped materials show largely ductile fractures. Sometimes, HIP is used to remove oxide films but it does not entirely remove oxide films, only collapses it, therefore still oxide layer remains. Thanks to HIP, some of oxide films within the material can be disrupted and broken by plastic deformation. As a result, closing internal voids enables to consolidate the material by bonding Al surfaces without oxide [4] [27].

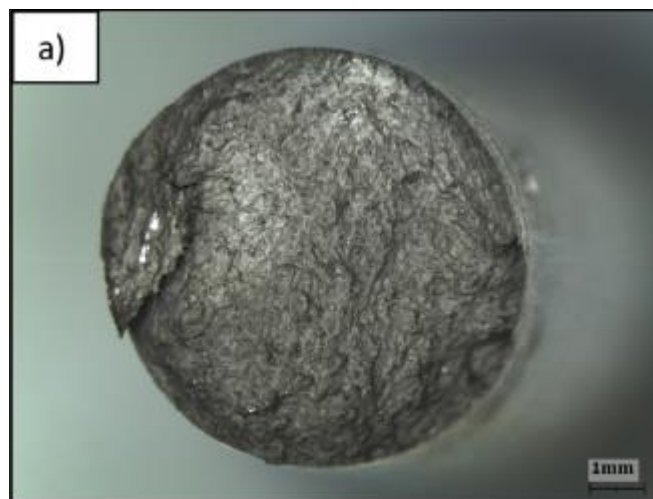


Figure 1. 28 OM observation of as-built additively manufactured AlSi10Mg [27]



Figure 1. 29 OM observation of HIP processed additively manufactured AlSi10Mg [27]

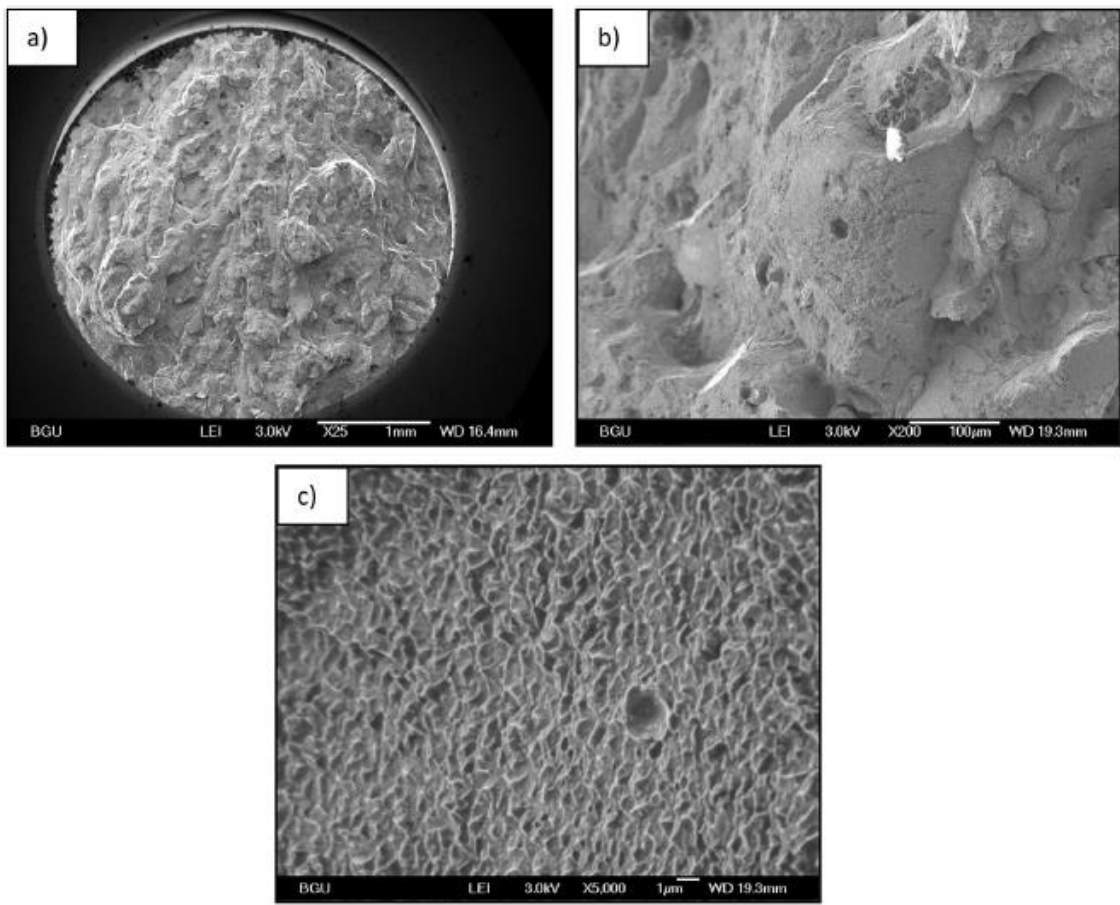


Figure 1. 30 SEM images of the tensile fracture surfaces for the as-built additively manufactured AlSi10Mg alloy [27]

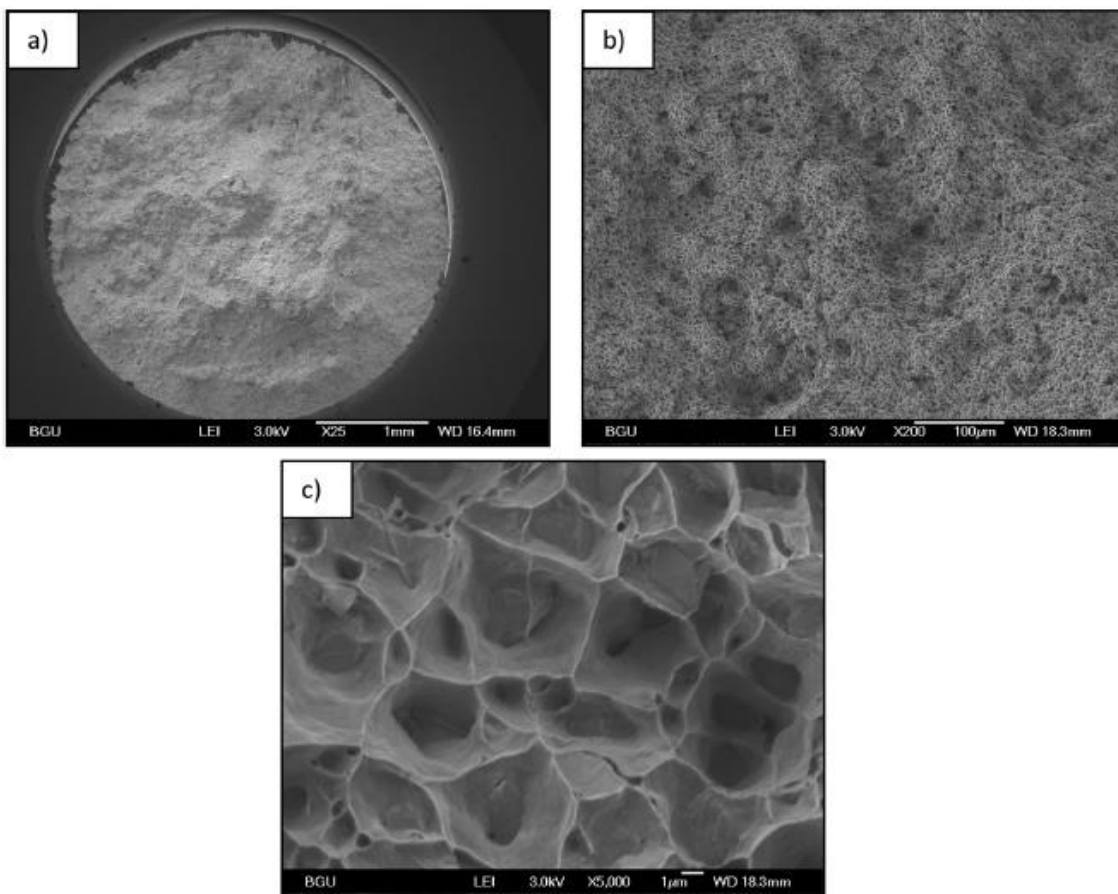


Figure 1. 31 SEM images of the tensile fracture surfaces for the HIPped additively manufactured AlSi10Mg alloy [27]

When Charpy specimens are observed, compared to tensile specimens high degree of deformation are seen. Macrostructures of Charpy specimens show that track segments at the end of the fracture for as-built condition. Also, at microstructure track segments and many nucleation sites are observed. Moreover, higher magnification shows canals and shallow dimples. On the other hand, similar to tensile test results HIP erases traces of the hatching strategy and exhibit larger elongation.

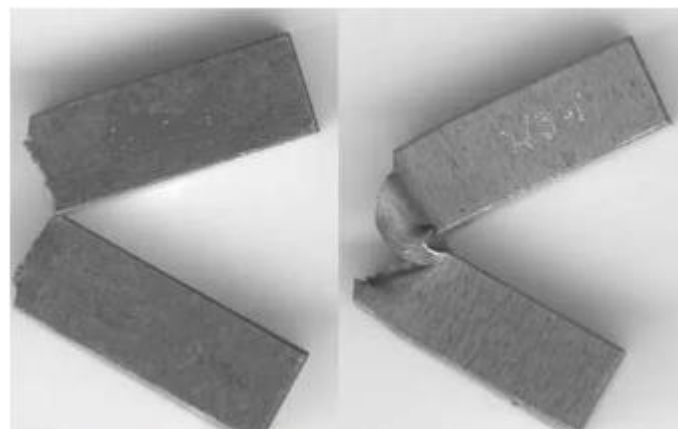


Figure 1. 32 Examples of brittle and ductile mechanism at the end of Charpy impact tests [59]



Figure 1. 33 OM observation of Charpy fracture surface of additively manufactured as-built AlSi10Mg [27]



Figure 1. 34 OM observation of Charpy fracture surface of additively manufactured HIPped AlSi10Mg [27]

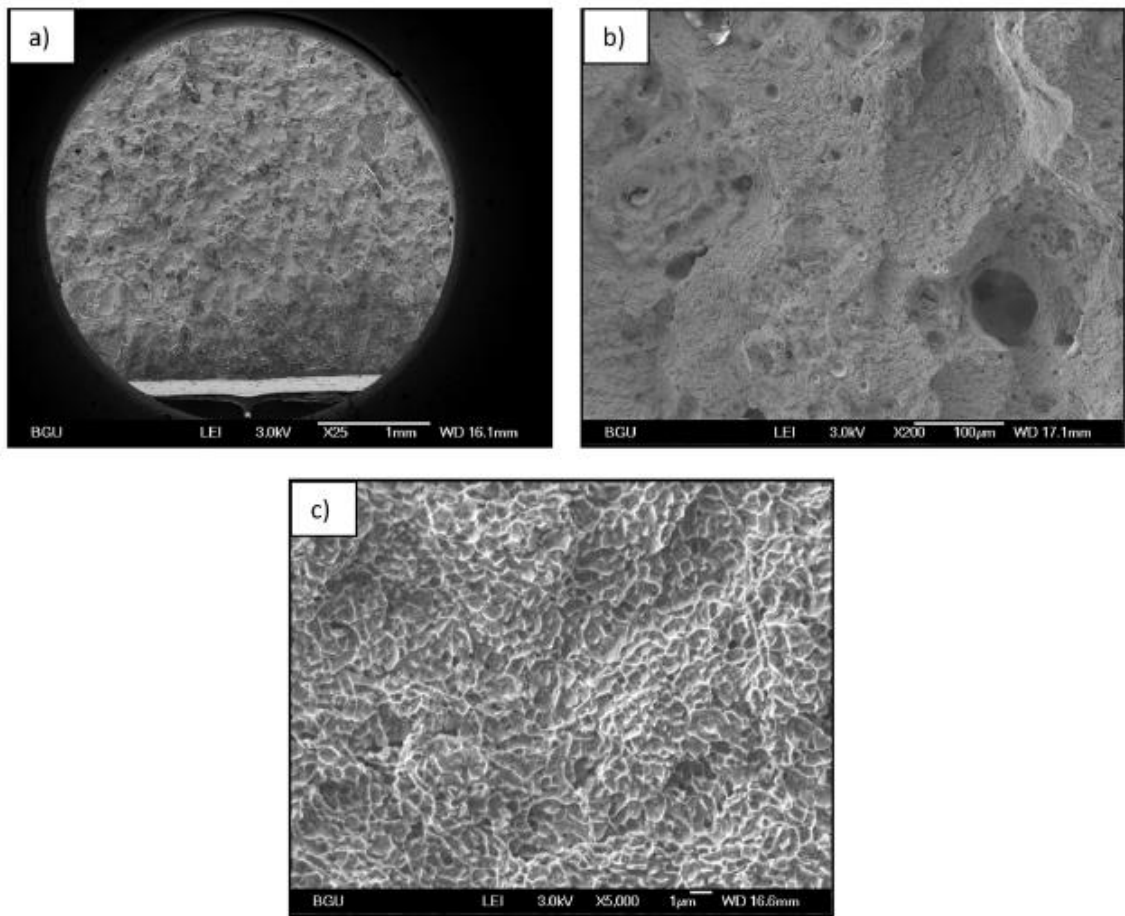


Figure 1. 35 SEM images of the impact fracture surfaces for the as-built additively manufactured AlSi10Mg alloy [27]

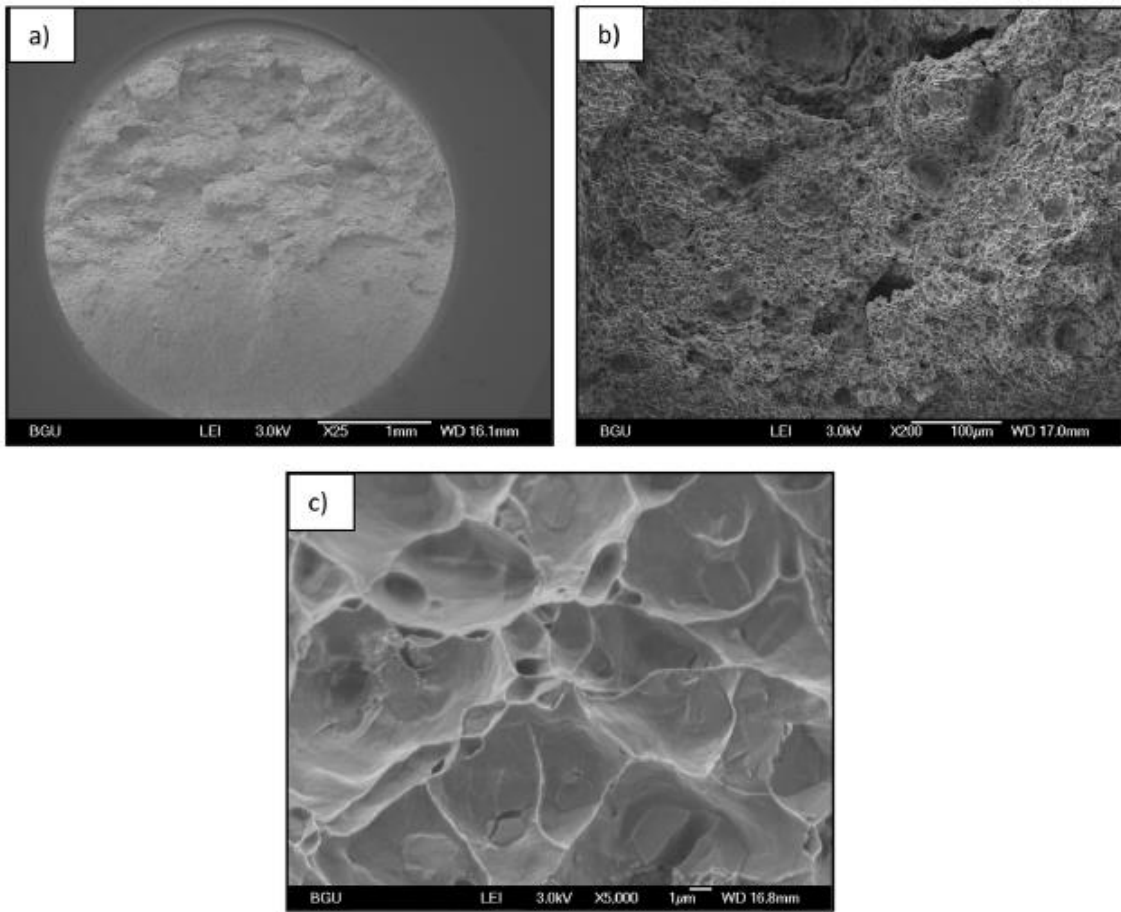


Figure 1.36 SEM images of the impact fracture surfaces for the additively manufactured HIPped AlSi10Mg alloy [27]

As a result, generally in the literature, both in tensile and Charpy tests, ductile-brittle mixed fracture surfaces with increasing temperature are converted into ductile fractures.

1.8. Aluminum and AlSi10Mg Alloy

Al is one of the most utilized metals. Window frames, buildings, electronic devices, industry, ships, submarines, vehicles, especially aeronautics, and space parts are places that Al is widely used. It has so many benefits, such as lightweight, weldability, and machinability. These are the reasons why Al is widely used. On the other hand, there are some drawbacks, for example cost and overall strength, when compared to some other materials.

Pure Al has unqualified mechanical properties. Therefore, some other elements combine with Al to form Al alloys. These alloys are mainly composed of Al, with minor amounts

of additional elements. Generally, added elements are silicon, magnesium, zinc, iron, and copper. These additional elements contribute to alloys with respect to high strength, corrosion resistance, and electrical and thermal conductivity.



Figure 1. 37 Aluminum parts [53]

AlSi10Mg is the most preferred Al alloy in the aerospace and automotive industries thanks to its beneficial properties such as low density, lightweight, corrosion resistance, and high strength-to-weight ratio. These properties come from its Al-Si eutectic microstructure. Also, laser PBF allows easily controllable microstructure. That's why they compromise and make a perfect couple together. To acquire qualified deposition [7], the spherical morphology of AlSi10Mg powders is required while producing. The other advantage of this couple is that powders are not wasted after the process. They can be recycled. The process parameters such as laser power, scanning speed, hatching distance, beam radius, and layer thickness should be optimized to get the best mechanical properties [40]. Also, the process environment should have an oxygen level below 0.2% to prevent oxidation.

2. MATERIAL AND METHOD

One of the most utilized additively manufactured materials is alloys. Microstructure control is easier with AM compared to conventional manufacturing methods. AlSi10Mg alloys have superior mechanical properties, and lightweight. That's why the microstructure and mechanical property relationship are significant, and additively manufactured AlSi10Mg is promising. Scientific research has been continued to determine and improve the microstructure and mechanical property relationship [2, 12, 14, 15, 28].

The chemical composition of the AlSi10Mg is seen in Table 2.1.

Table 2. 1 Chemical composition of the AlSi10Mg Powder [41]

Al	Si	Fe	Cu	Mn	Mg	Zn	Ti
Balance	9.00-11.00	0.55	0.05	0.45	0.20-0.45	0.10	0.15

2.1. Sample Preparation

Tensile test and Charpy test specimens were machined by the wire erosion method. A milling machine was used for the notch and radius of Charpy test specimens.

Metallographic specimens to investigate microstructure were prepared by the following steps: cutting samples with an abrasive cut off machine, bakelite model; coarse, medium, and fine grinding (600-800-1000 grits), polishing, etching with Keller's reagent (1% HF, 1.5% HCl, 2.5% HNO₃ and 95% H₂O) for 30 sec.

2.2. Archimedes' Density Method

The densities of samples were measured by Mettler AJ100 with Archimedes' principle.

$$\rho_{sample} = \rho_{ethanol} \cdot \frac{W_{air}}{W_{air} - W_{ethanol}}$$

In the beginning, samples were cut with a handsaw. Then, samples were filed to get rid of burrs in the material. Firstly, the weight of each sample was measured. Then, their weights were measured in ethanol. We were given the density of the ethanol as 0.8050 g/cm³. So, we were able to calculate the density of samples.



Figure 2. 1 Density measurement device Mettler AJ100

2.3. Micro- and Macrostructure Observation

Microstructural analysis was observed with OM (Nikon Epiphoto 300) and SEM (Zeiss Evo Ma 10). Also, fracture mechanism was observed with OM (Nikon SMZ1500) and SEM (Zeiss Evo Ma 10).



Figure 2. 2 Nikon Epiphot 300 [60]



Figure 2. 3 Nikon SMZ1500 [61]



Figure 2. 4 Zeiss Evo Ma 10 [62]

2.4. Hardness Test

Since the specimen thickness dimension is subsized, Vickers microhardness was measured via Future Tech FM-340c. Three specimens were subjected to a 200 g load for 10 seconds.

2.5. Tensile Test

Samples used in the tensile test are machined by wire erosion following TS EN ISO 6892-1. As an exception, grip lengths of samples are taken longer to place in the test machine properly. Tensile tests were conducted using Shimadzu AGS-X 50 kN by using Trapezium X software. As a strain rate of 1 mm/min is selected and 5 tensile samples are used. During the test, strain measurement was monitored by video extensometer.



Figure 2. 5 Shimadzu AGS-X 50 kN Tensile Test Machine [54]

2.6. Charpy Impact Test

Charpy specimens were machined regarding TS EN ISO 148-1. Since we had insufficient materials, we used subsized dimensions. Specimen dimensions are 2.5 mm x 10 mm x 55 mm. We applied the Charpy test with Instron CEAST 9050. A computer was connected to the machine, and CWMMain software was used to acquire force-time and energy-time graphs. The V notch was 2 mm at 45°. Tests were performed at room temperature.

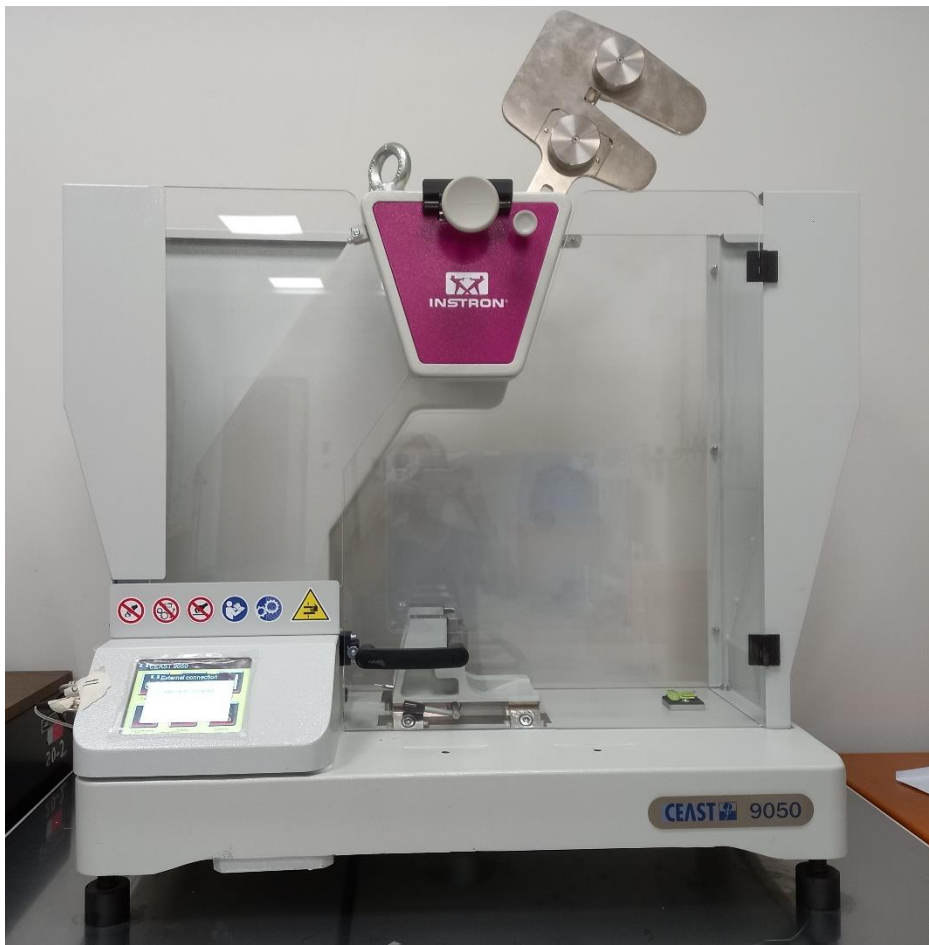


Figure 2. 6 Instron CEAST 9050

3. RESULTS AND DISCUSSION

3.1. Tensile Test Results

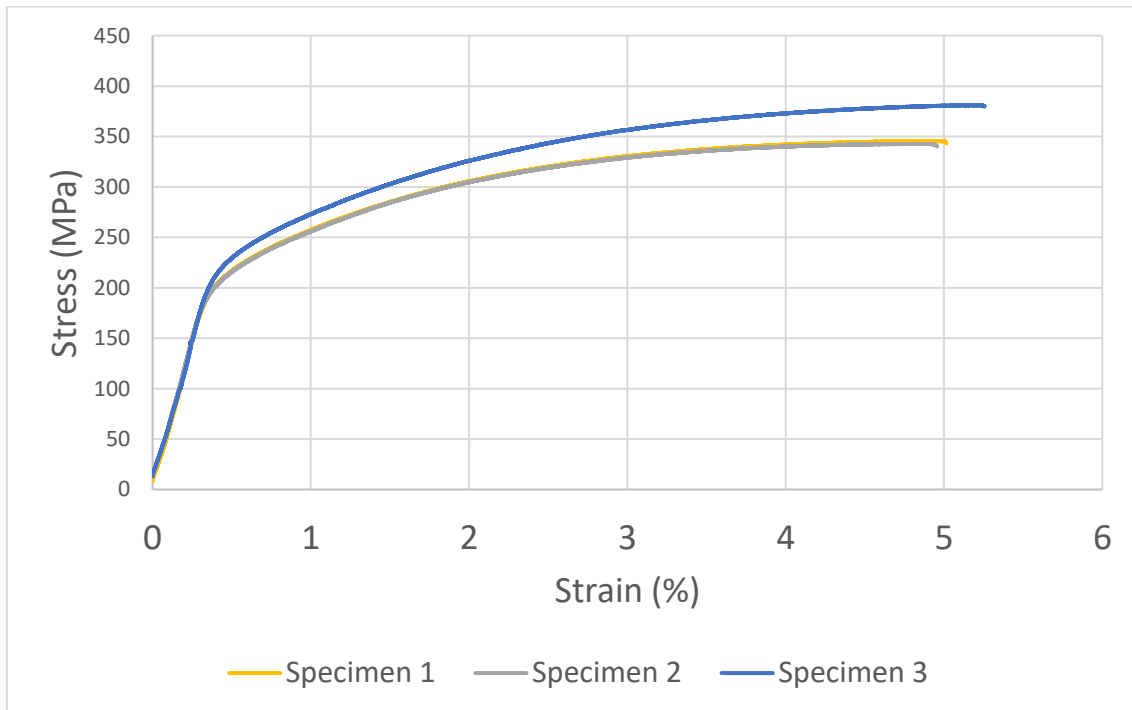


Figure 3. 1 Stress-strain curve

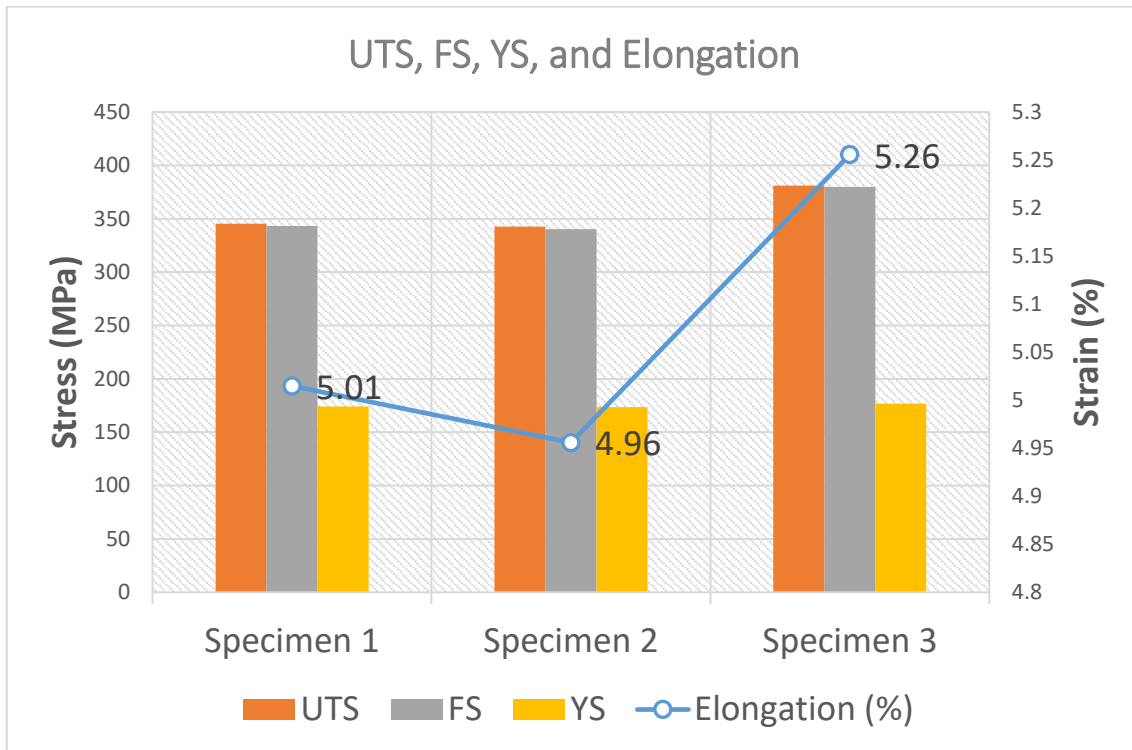


Figure 3. 2 Ultimate tensile stress, fracture stress, yield stress and elongation graph

Specimen 1, specimen 2, and specimen 3 represent specimen 3, specimen 4, and specimen 5, respectively. AlSi10Mg parts, which are produced by laser PBF process machined and acquired three tensile specimens due to ISO 6892. Force was applied until the specimens broke. Specimens were broken at a 45° angle. Regarding observations, Figure 3.1 shows the stress-strain curve resulting from the tensile test. The elongation is recorded by a video extensometer. The cross-sectional area of the specimens is 15.5025 mm^2 .

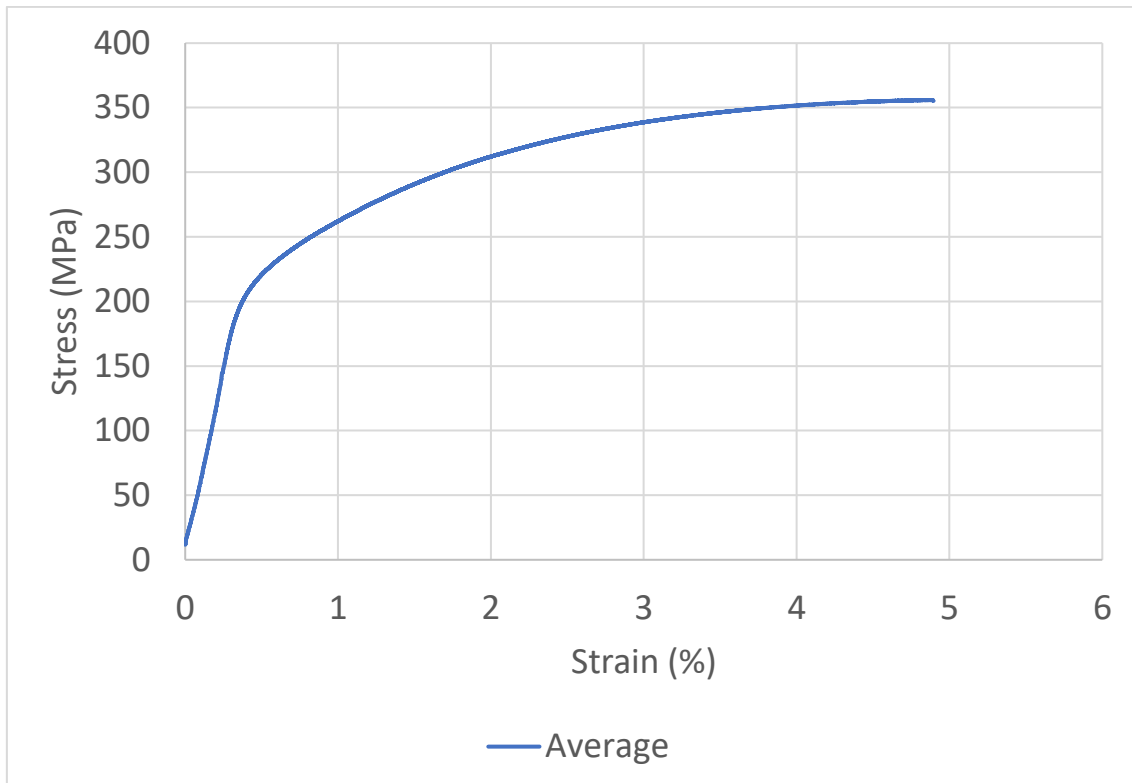


Figure 3. 3 Average stress–strain curve

Following the tensile test, mechanical properties were investigated in detail. YS and strain, ultimate stress and strain, FS and strain, modulus of elasticity were determined. Regarding the stress–strain curves, average values are as follows: The YS is approximately 175 MPa, and yield strain is 0.35%. The UTS is 356 MPa and the ultimate strain is 4.98%. The FS is 354 MPa, and fracture strain is 5%. The modulus of elasticity is 62 GPa. Since the specimens could not resist breaking so much, we can say that the material is close to brittle. On the other hand, after reaching the plastic region, the specimens did not break directly. Therefore, the material showed some ductile properties. So, additively manufactured AlSi10Mg is a mixed type of ductile–brittle. It behaves as both brittle and ductile. These results are close to the outputs of R.K. Everett et al. [9] by using auto-correlated AlSi10Mg parts. Y. Zhou, F. Ning, P. Zhang et al. demonstrated the tensile properties of as-built curved surface and as-built flat surface specimens. The flat surface specimen results are consistent with our findings [11]. J.N. Domfang Ngnekou et al. found similar results, demonstrating that yield strength increases with hardness [42]. Also, when the results were compared with as-built cast-produced AlSi10Mg, as-built additively manufactured AlSi10Mg has higher yield stress, and ultimate tensile stress,

which can be attributed to the manufacturing method. However, in some cases, as-built AM AlSi10Mg demonstrated less elongation than as-built cast-produced ones possibly due to process parameters.

Table 3. 1 Tensile Test Results

	Yield Stress (MPa)	Yield Strain (%)	Ultimate Stress (MPa)	Ultimate Strain (%)	Fracture Stress (MPa)	Fracture Strain (%)	Modulus of Elasticity (GPa)
Average	174.83±1.00	0.30±0.001	356.45±12.37	4.978±0.212	354.42±22.09	5.076±0.092	62.033±1.225
GC [1]	112±10	-	210±8	-	-	3.9±1.0	-
GC [63]	99		193			6.52	114
GC [64]	115		183			2	
HPVDC [64]	170		320			8	

Uncertainty is calculated with the sample standard deviation and standard error of the mean formulas.

3.2. Charpy Test Results

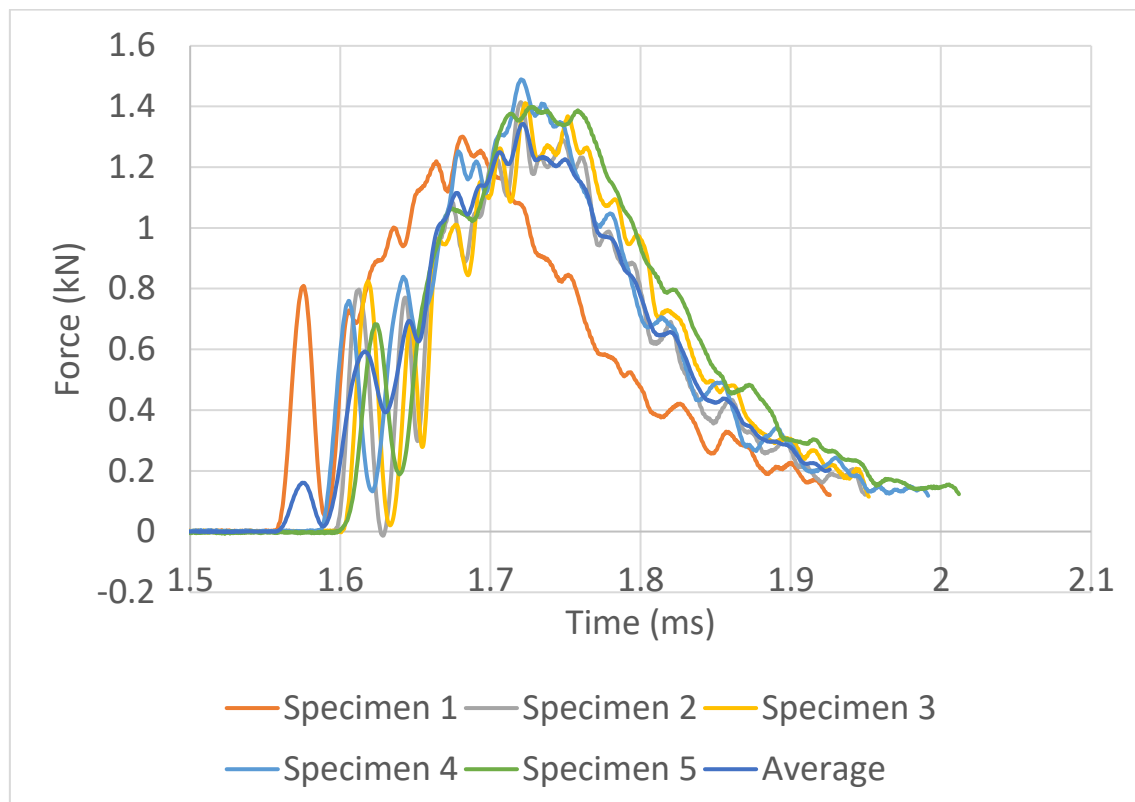


Figure 3.4 Force-Time curves

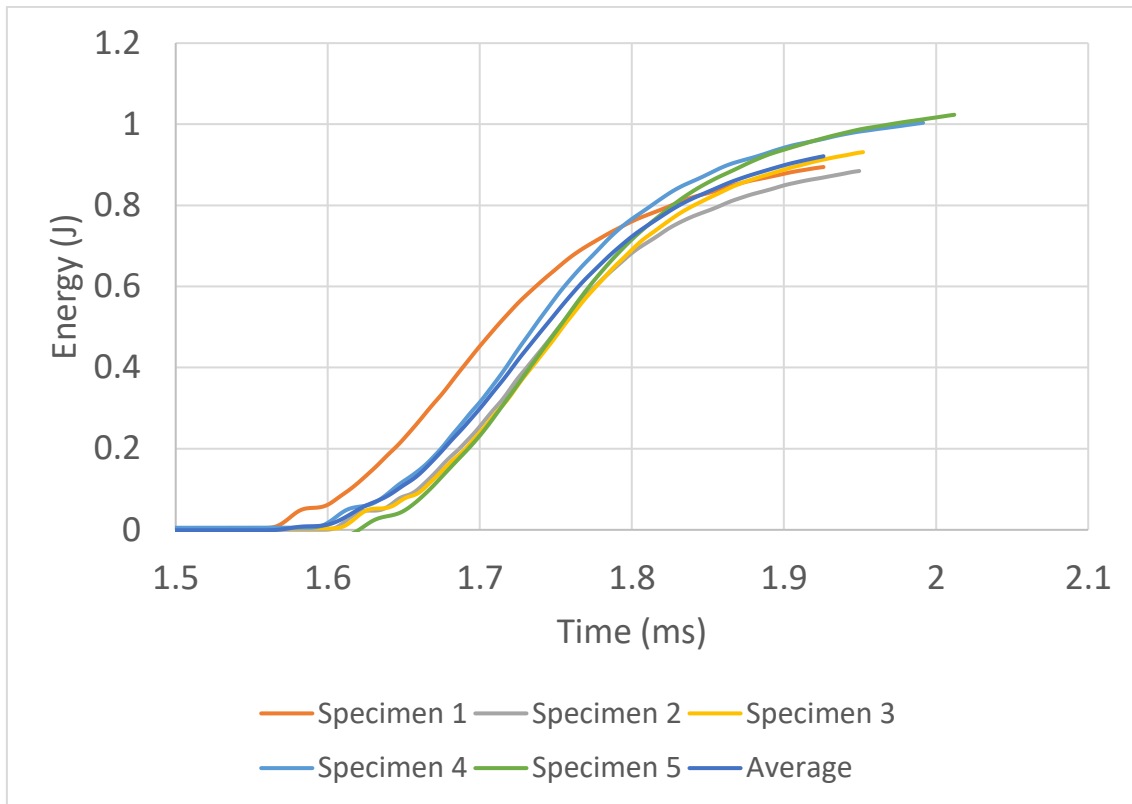


Figure 3.5 Energy-Time curves

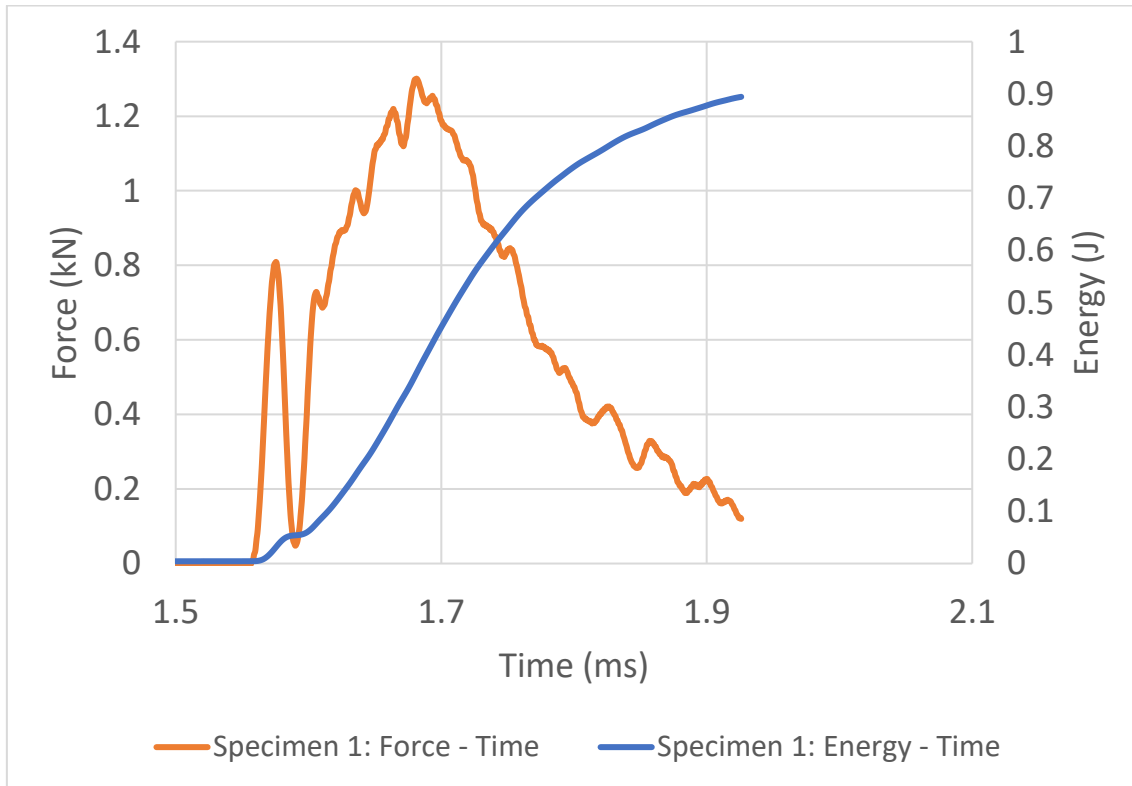
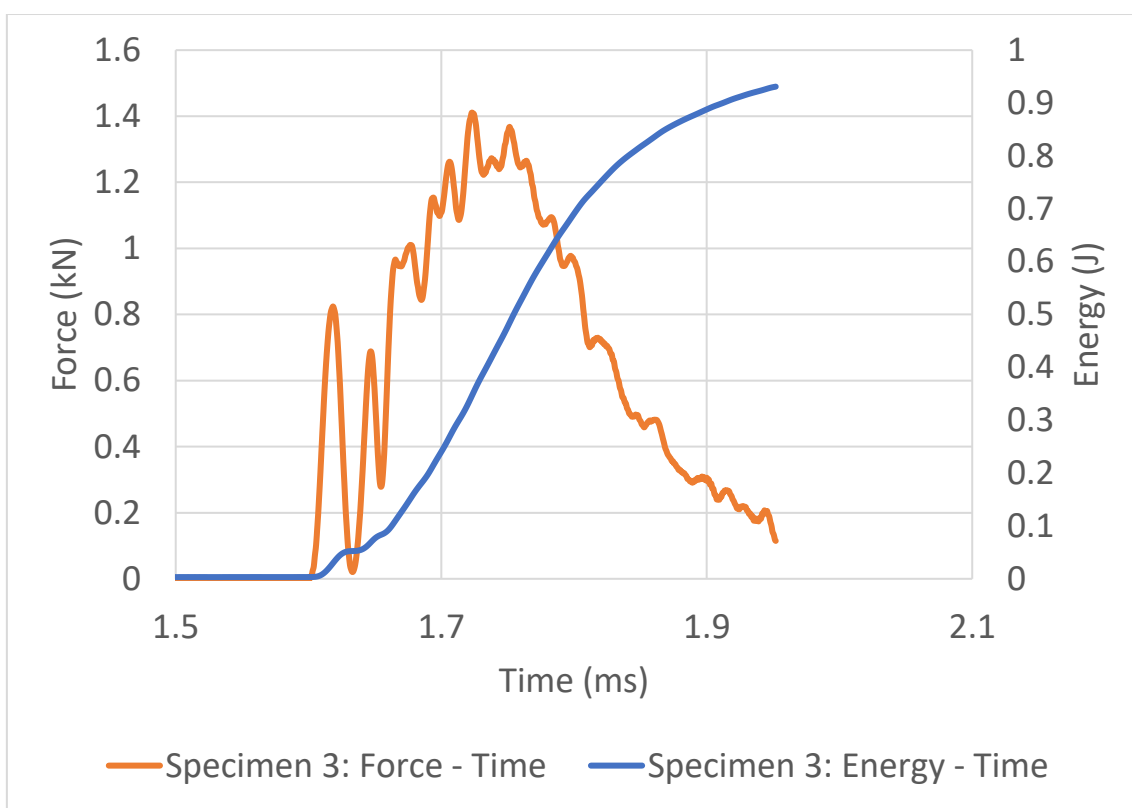
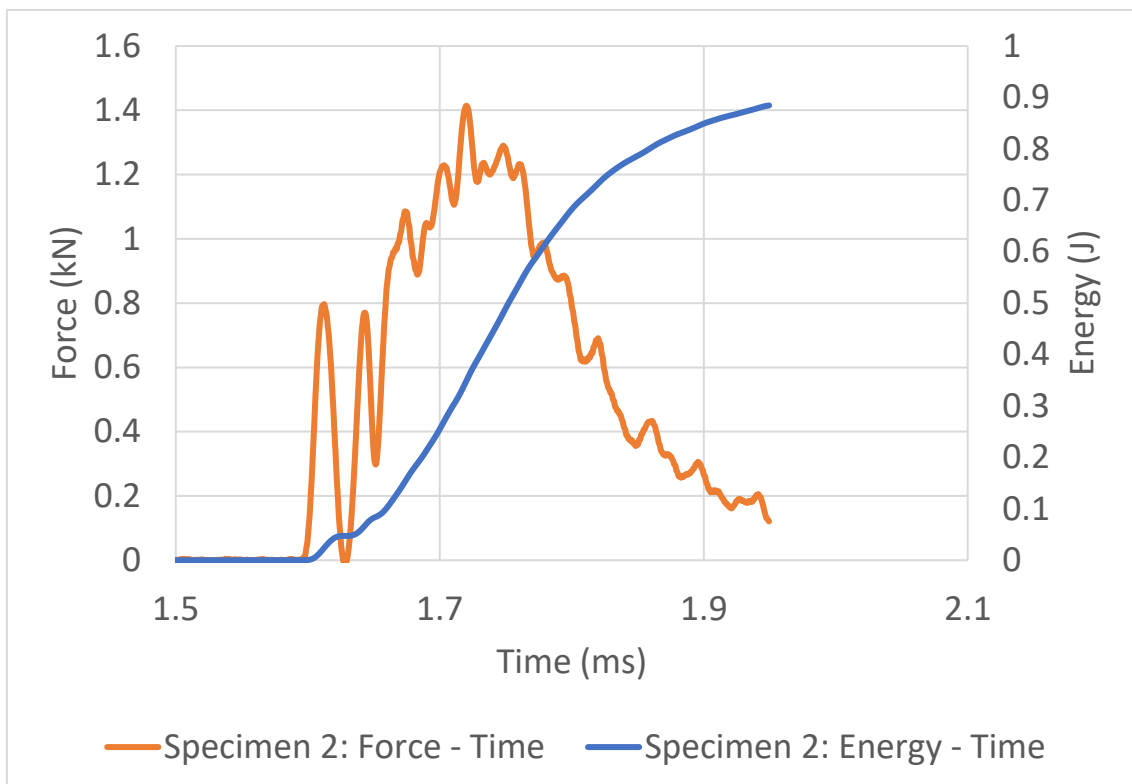


Figure 3.6 Energy-Time curve specimen 1



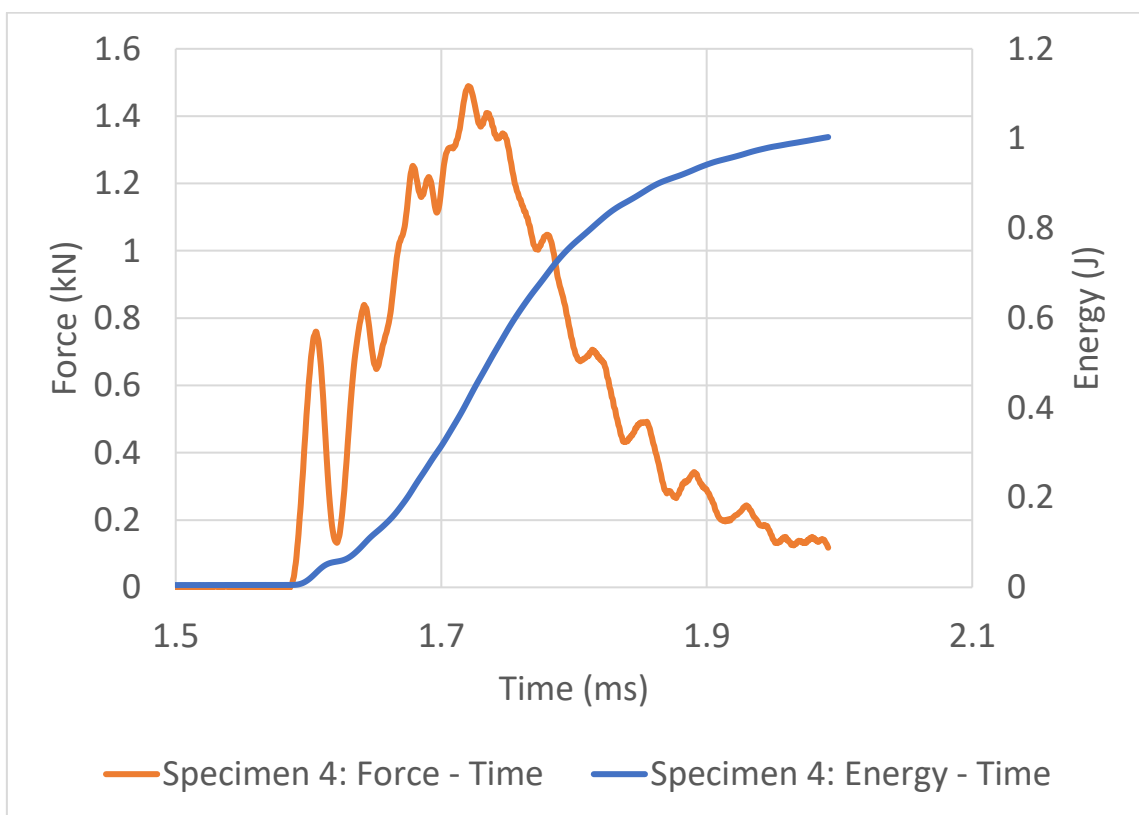


Figure 3. 9 Energy-Time curve specimen 4

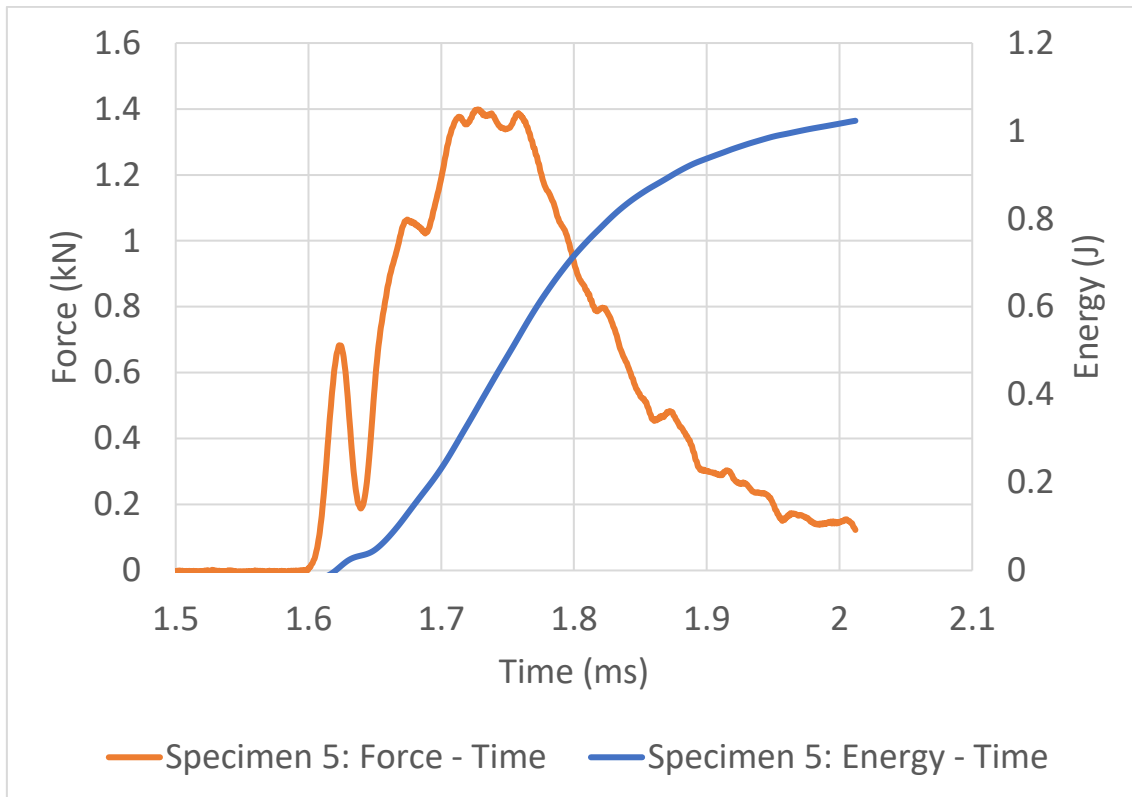


Figure 3. 10 Energy-Time curve specimen 5

In the Charpy impact test, the absorbed energy is calculated from the basic energy conversation theorem. The following formula is used to find absorbed energy:

$$E = m \cdot g \cdot (h - h')$$

Here, m is the pendulum's mass, g is the gravitational acceleration, h is the height of the pendulum release, and h' is the maximum reaching the height of the pendulum after the impact.

As a result of Charpy impact tests, we acquired force-time and energy-time graphs for five as-built additively manufactured AlSi10Mg. We examined maximum load, crack initiation resistance, crack propagation resistance, total crack resistance, maximum displacement, and absorbed energy per area for each sample in Table 3.2. At room temperature, the average maximum load was 1.40 kN, the average crack initiation resistance was 0.102 J/cm^2 , the average crack propagation resistance was 0.135 J/cm^2 , the average total crack resistance was 0.237 J/cm^2 , the average maximum displacement was 7.46 mm, the average absorbed energy per area was 0.038 J/mm^2 . The acquired values well-suit the literature results [32, 31]. While the elongation increases, the

absorbed energy is also increased except between specimens 1 and 2. T. However, when considering the other specimens, this situation does not exist. If this were valid for all specimens, we could say that the material is entirely ductile [27]. The Charpy impact test results indicate that the material is both ductile and brittle.

Table 3. 2 Charpy Impact Test Results

	Maximum Load (kN)	Crack Initiation Resistance (J/cm ²)	Crack Propagation Resistance (J/cm ²)	Total Crack Resistance (J/cm ²)	Maximum Displacement (mm)	Absorbed Energy per Area (J/mm ²)
Specimen 1	1.30	0.093	0.131	0.224	7.31	0.036
Specimen 2	1.41	0.095	0.126	0.221	7.40	0.035
Specimen 3	1.41	0.095	0.138	0.233	7.41	0.037
Specimen 4	1.49	0.115	0.136	0.251	7.56	0.040
Specimen 5	1.40	0.111	0.144	0.255	7.64	0.041
Average	1.40	0.102	0.135	0.237	7.46	0.038
GC [63]	-	-	-	-	-	0.038

Since subsized specimens were used in Charpy impact tests, absorbed energy per area gives more sensible results to compare results with casting. The average results of absorbed energy per area equal the results of [63] gravity casting absorbed energy per area.

3.3. Density Measurements

Density is measured via Mettler aj100 with Archimedes' principle on four specimens. The density value can be calculated by the following equation. The average density of as-built additively manufactured AlSi10Mg is 2.6355 g/cm³ which is less than the density of the as-built gravity casting AlSi10Mg [1] (2.669 g/cm³). Less density of additively manufactured products can be attributed to the porosity level which is the inherent property of the additive manufacturing process.

$$\rho_{sample} = \left(0.8050 \frac{g}{cm^3} \cdot \frac{0.6764g}{0.2066g} \right) = 2.6355 \frac{g}{cm^3}$$

The theoretical density of AlSi10Mg is 2.68 g/cm³. The relative density is equal to the ratio of the absolute density to the theoretical density. So, we can determine the relative density as follows:

$$\rho_{relative}(\%) = \frac{\rho_{absolute}}{\rho_{theoretical}} = \frac{2.6355 \frac{g}{cm^3}}{2.6800 \frac{g}{cm^3}} = 0.98 = 98\%$$

Relative density is equal to 98%. These values are adoptable with the other AM AlSi10Mg studies [10, 38, 43].

3.4. Hardness Test Results

Utilized specimens for the hardness test were Charpy impact test specimens. Three specimens' HV were measured seven times. After that, the average value and the standard deviation were calculated. The first specimen's average HV is acquired as 104.10. The second specimen's average HV is 105.90. The last specimen's average HV value is 107.61. These values are shown in the following table.

Table 3. 3 Vickers microhardness analysis

	Average HV	Standard Deviation of HV
Specimen 1	104.10	1.91
Specimen 3	105.90	1.34
Specimen 5	107.61	2.21
GC [63]	67	3
GC [64]	87	2
HPVDC [64]	95	5

When these results were compared with cast AlSi10Mg, PBF AlSi10Mg has higher microhardness values than cast AlSi10Mg [63], [64].

3.5. Microstructure

Results are taken from the OM, with a low magnification rate, in both view, top and side respectively. The top view showed that laser scan tracks in ellipsoid shape and the side view exhibits overlapping layers in half-cylinder shape, it is also called fish scale. Also, from the top view figure (3.11, 3.12 and 3.13) it is clearly understood that the scanning direction is at 45° degrees.

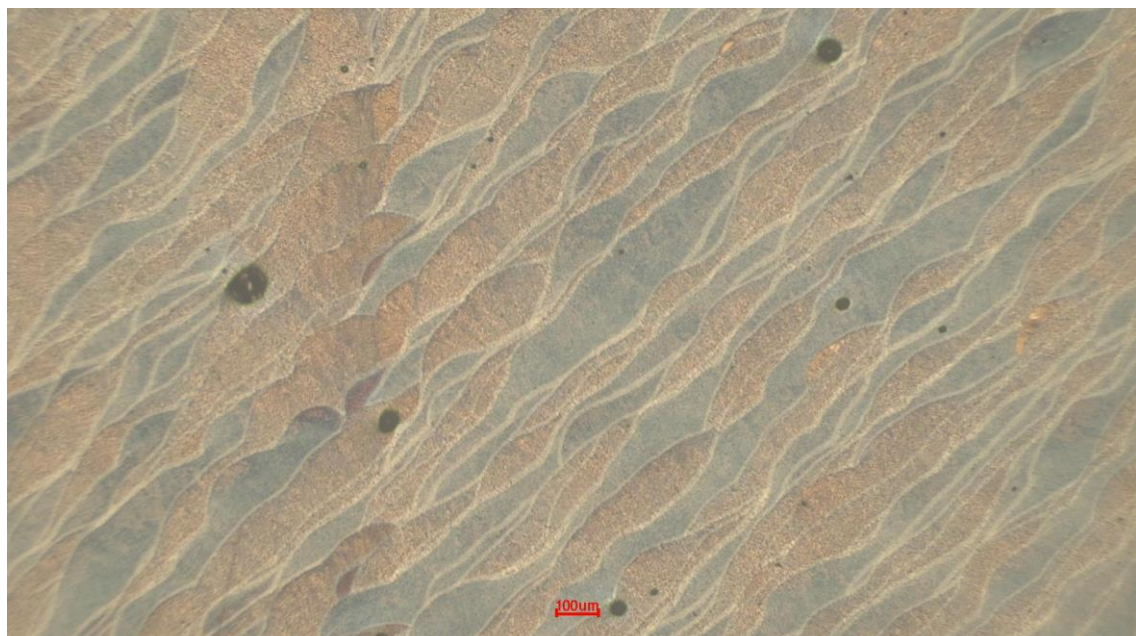


Figure 3. 11 Laser scan tracks



Figure 3. 12 Void-free laser scan tracks

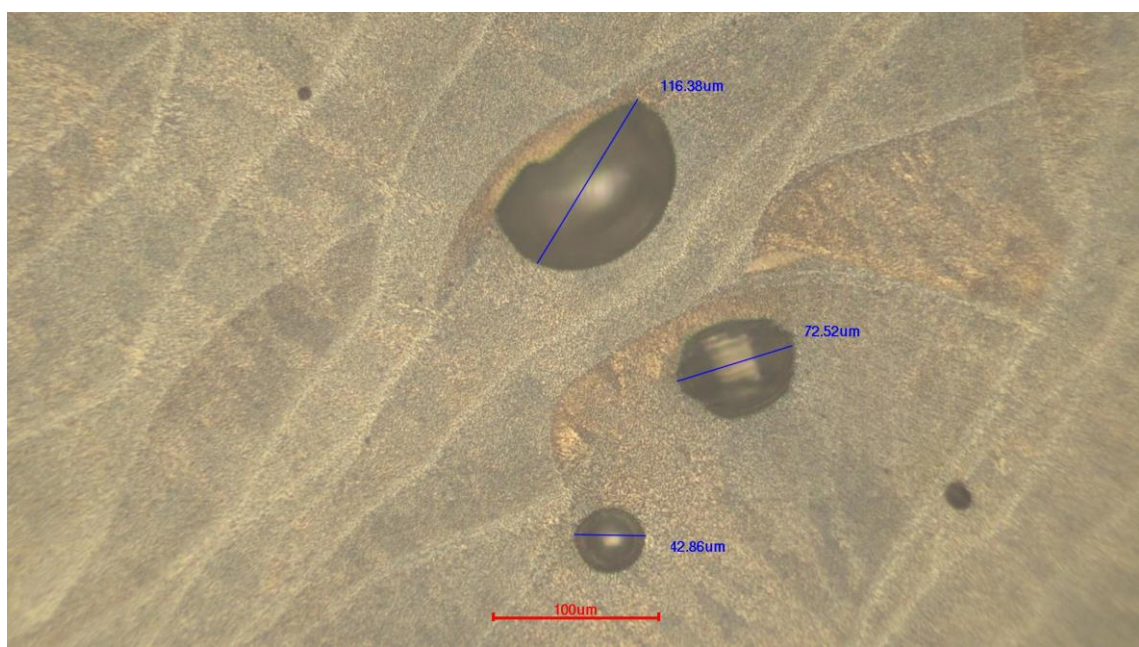


Figure 3. 13 Pores on the laser scans

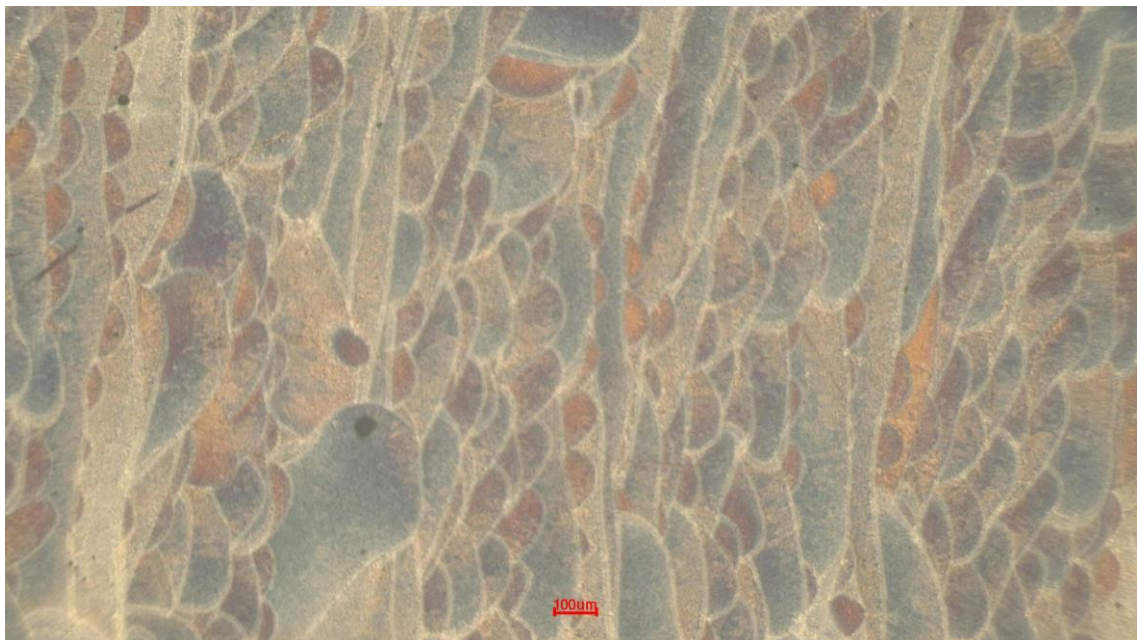


Figure 3. 14 Fish scale morphology as a result of layer-by-layer manufacturing process



Figure 3. 15 Magnified fish scale morphology

Additionally, the microstructure of the material is investigated by SEM. Below figure 3.16 shows the microstructure of AlSi10Mg with 1.5K magnification. Here, the fine and coarse regions were shown. Also, HAZ was observed.

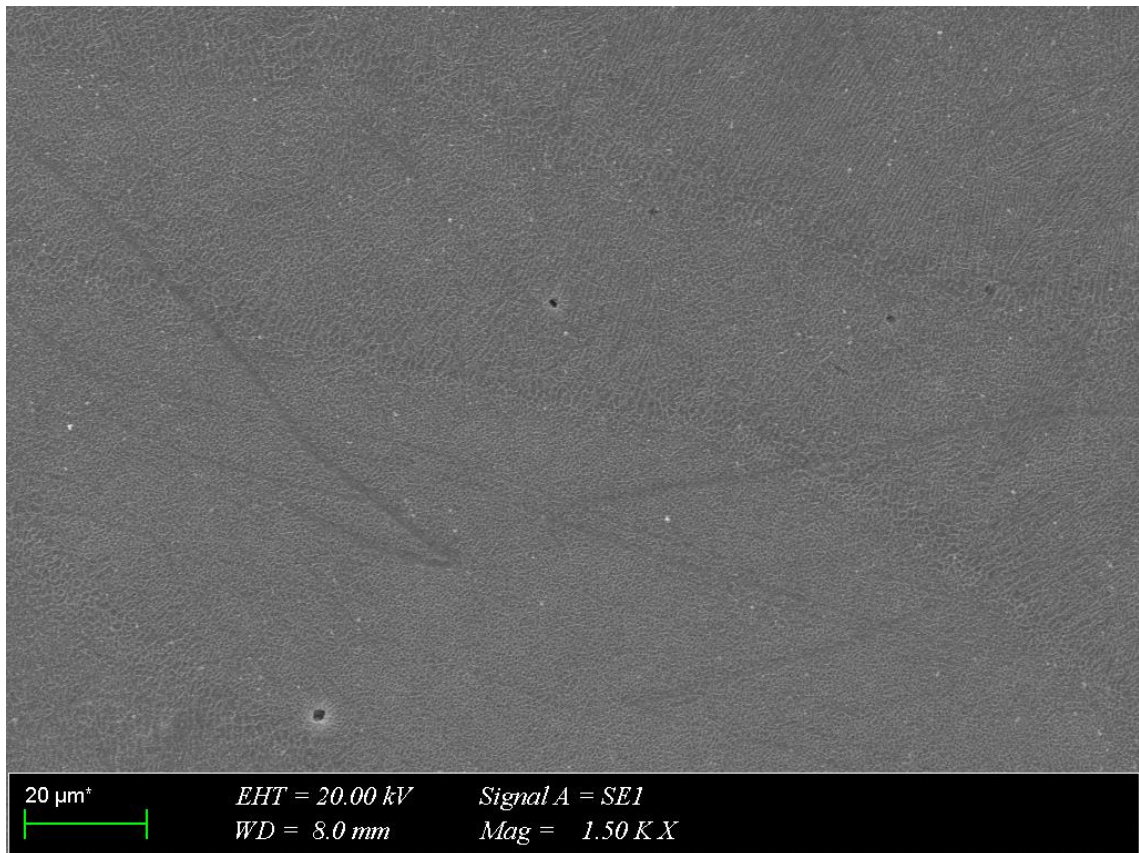


Figure 3. 16 SEM observed microstructure (1500X)

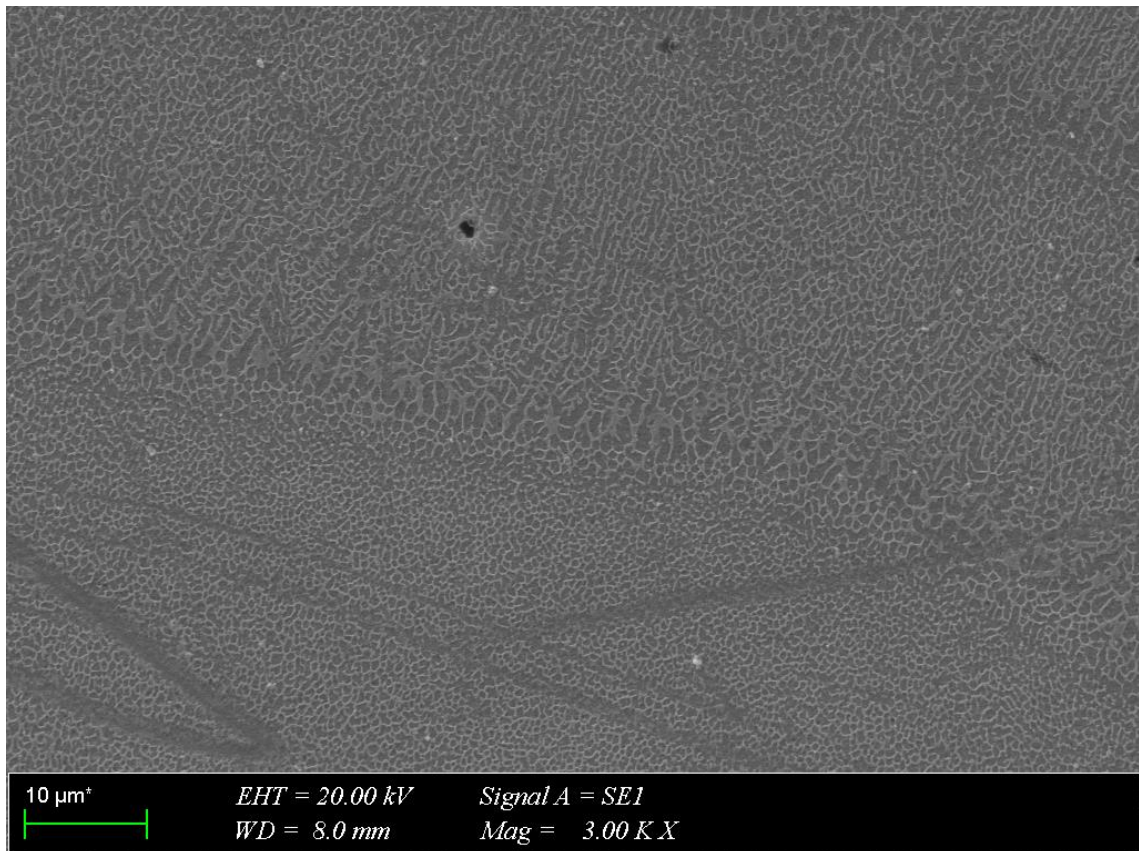


Figure 3. 17 SEM observed microstructure (3000X)

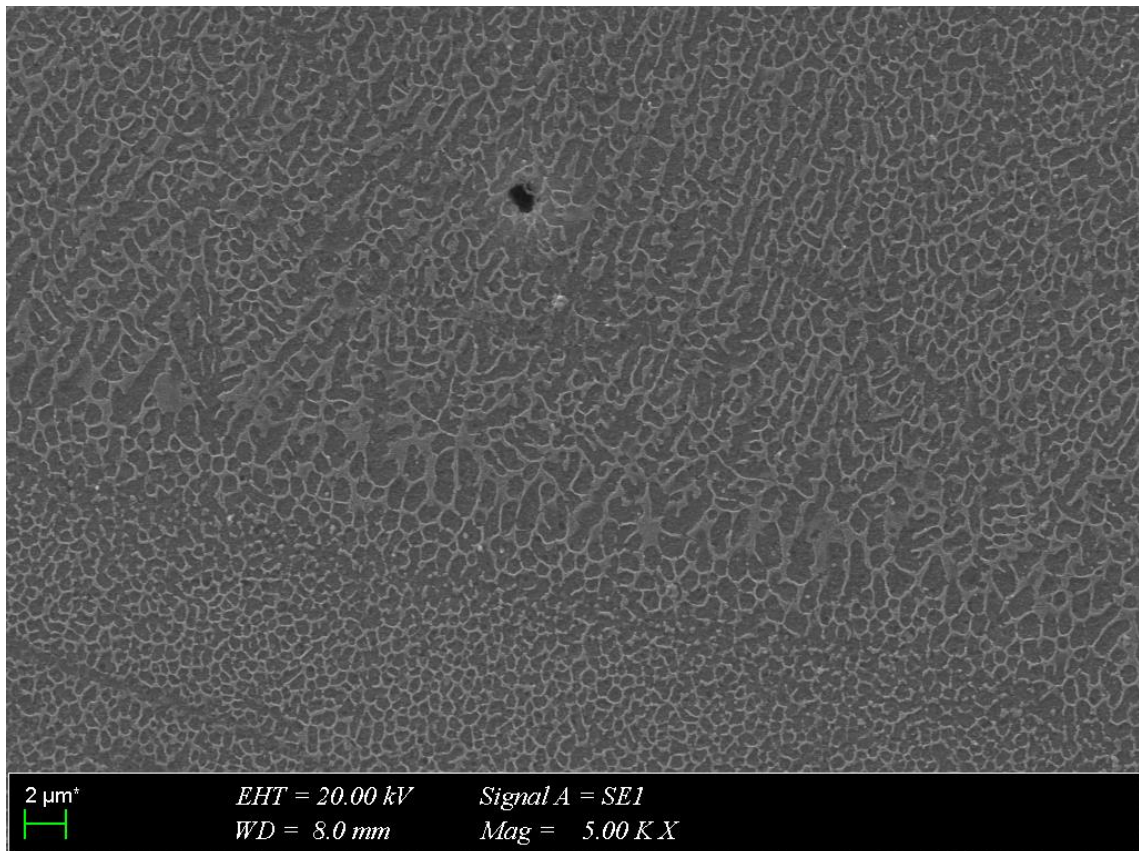


Figure 3. 18 SEM observed microstructure (5000X)

Figures 3.17 and 3.18 show the microstructure with 3K and 5K magnification, respectively. In these figures, the microstructure can be seen closer.

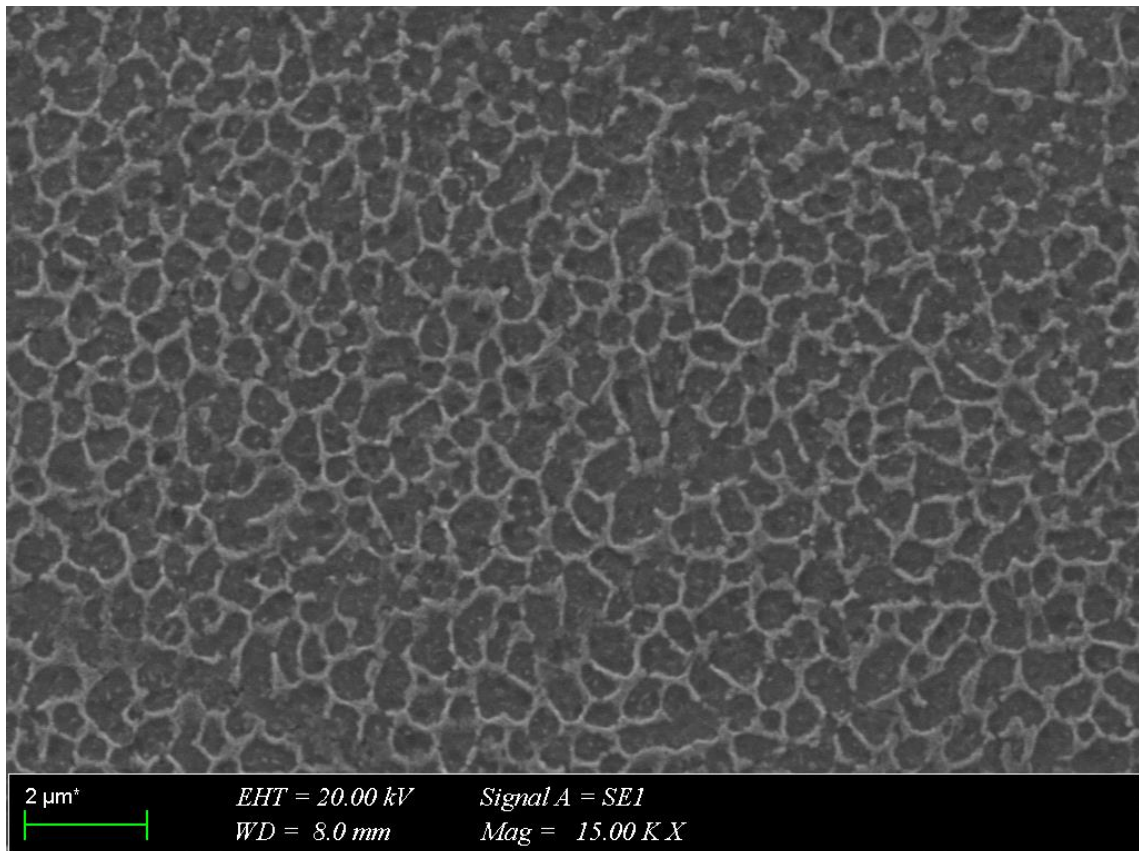


Figure 3. 19 SEM observed fine microstructure (15000X)

Figure 3.19 shows the fine Al-Si dendrites. Also, below figure 3.20 exhibits coarse Al-Si dendrites.

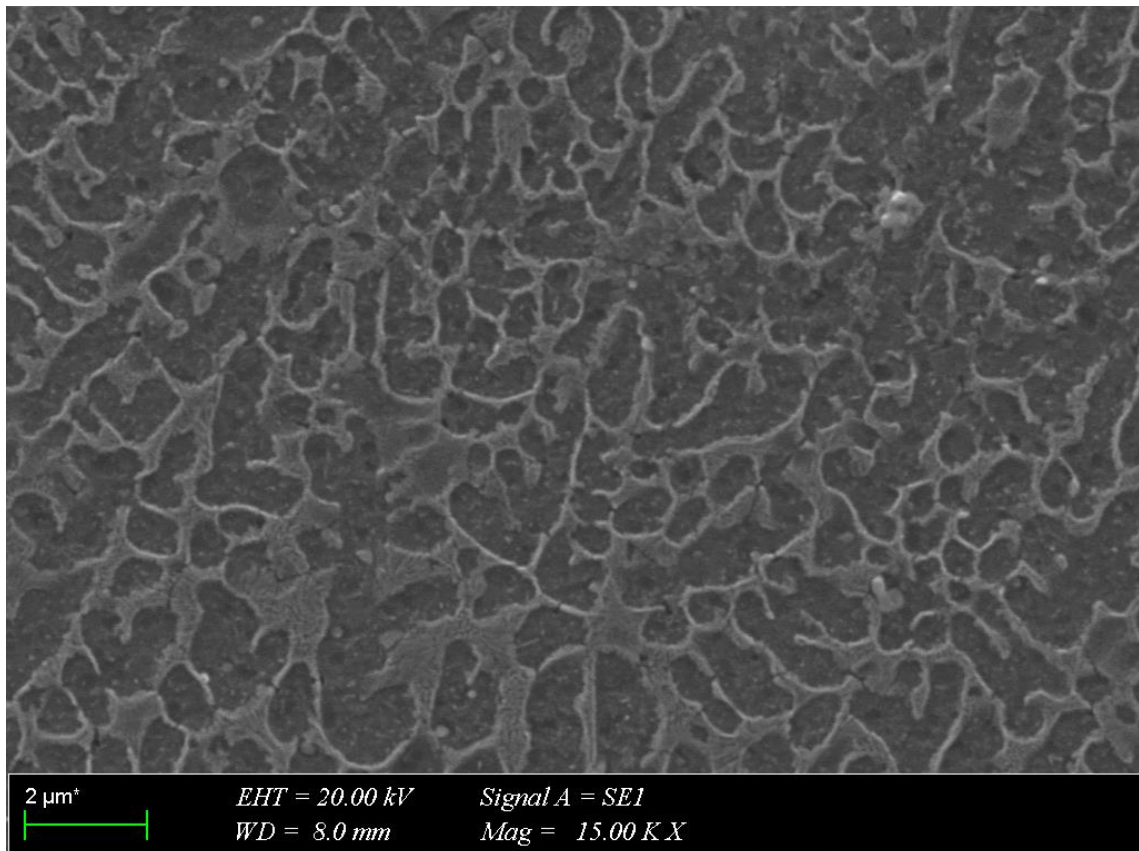


Figure 3. 20 SEM observed coarse microstructure (15000X)

In the above figures, small pores also were observed. To investigate the chemical composition of the pore and the material, Energy Dispersive X-Ray Analyses were done.

Table 3. 4 EDX Analysis

	Al	Si	O	Cu	Total Weight (%)
Spectrum 1	89.48	10.52	-	-	100
Spectrum 2	60.15	5.79	5.74	28.32	100

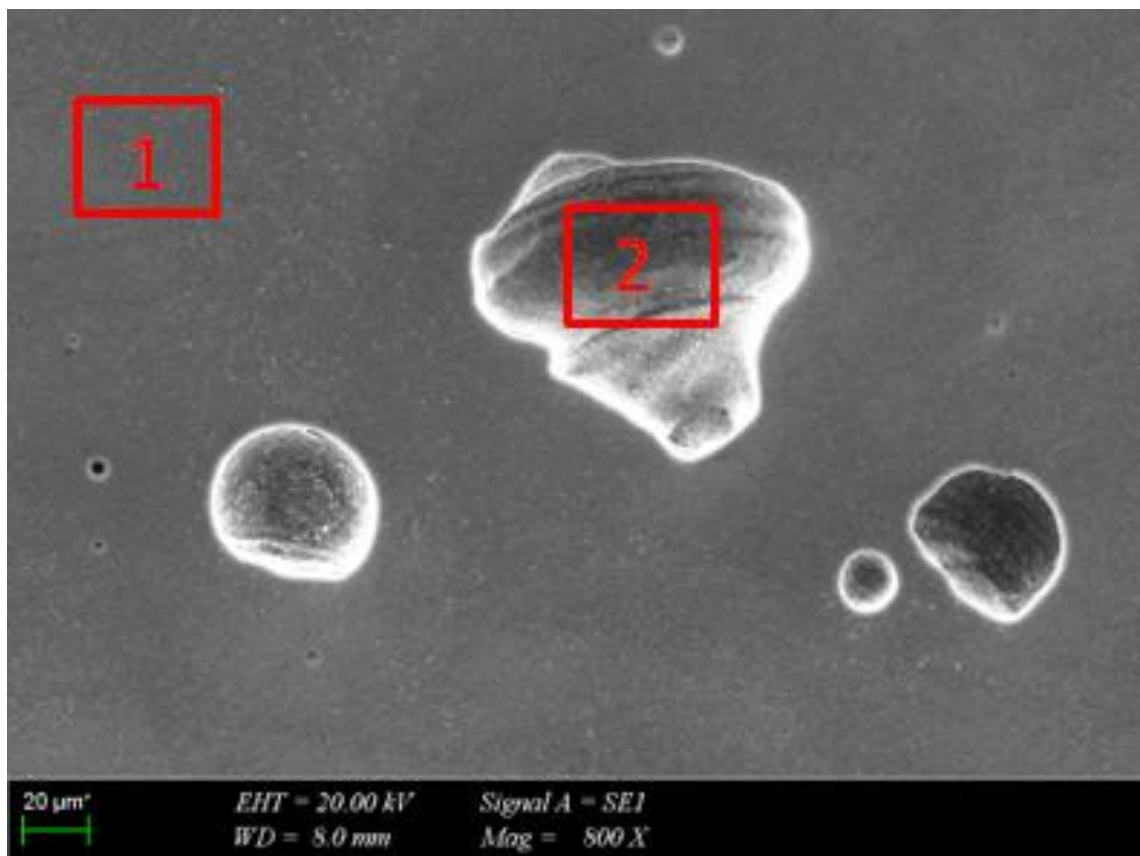


Figure 3. 21 EDX (Energy Dispersive X-Ray) Analysis (800X)

Figure 3.21 shows examples of pores. Circle-like shaped and irregularly shaped pores were the results of entrapped gas and the lack of fusion problem.

3.6. Fracture Mechanics

In this section, fracture mechanisms of additively manufactured AlSi10Mg as a result of tensile and Charpy tests, are observed with the OM and SEM. To investigate properly, three samples of tensile and Charpy fracture surfaces are used.



Figure 3. 22 Specimens after tensile test

3.6.1. Tensile Fracture Surfaces

In figure 3.23, the fracture mechanism of specimen 3 is shown. On a macro scale, it can be understood that fracture does not take place with decreasing in the cross-sectional area of the specimen. However, fibrous fractures with 45 degrees are seen between the failed parts. Furthermore, as separated parts are examined by OM, shear lips and similar to cup and cone mechanism is understood.



Figure 3. 23 Tensile specimen 3

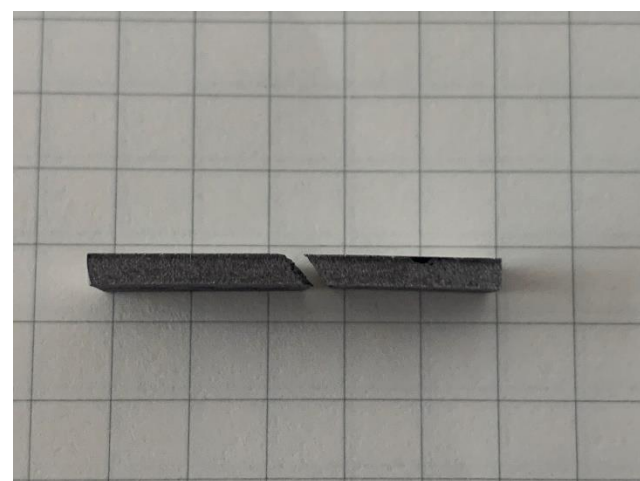


Figure 3. 24 Side view of fractured part of specimen 3



Figure 3. 25 Top view of fractured part of specimen 3

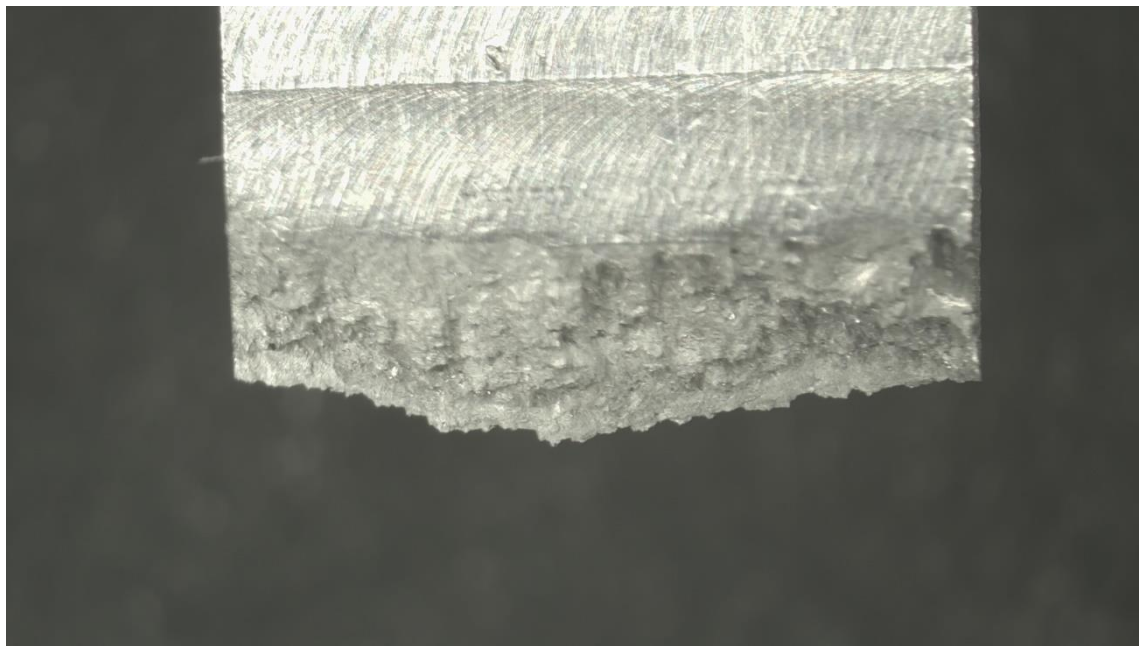


Figure 3. 26 Optically observed side view of fracture surface of specimen 3

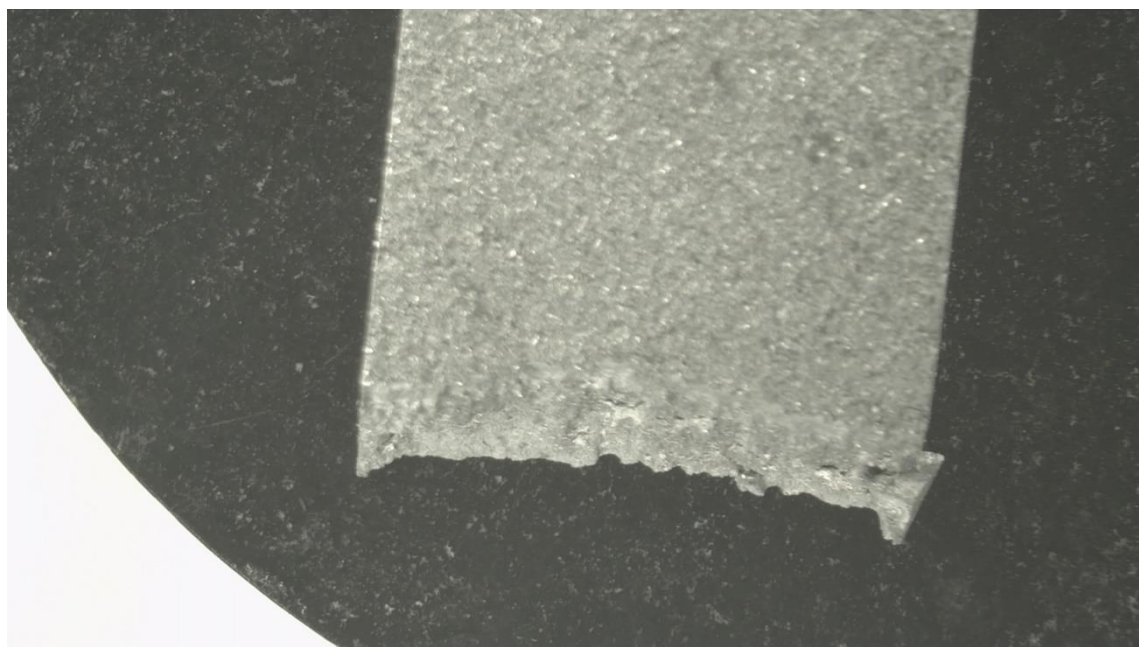


Figure 3. 27 Optically observed side view of fracture surface of specimen 3

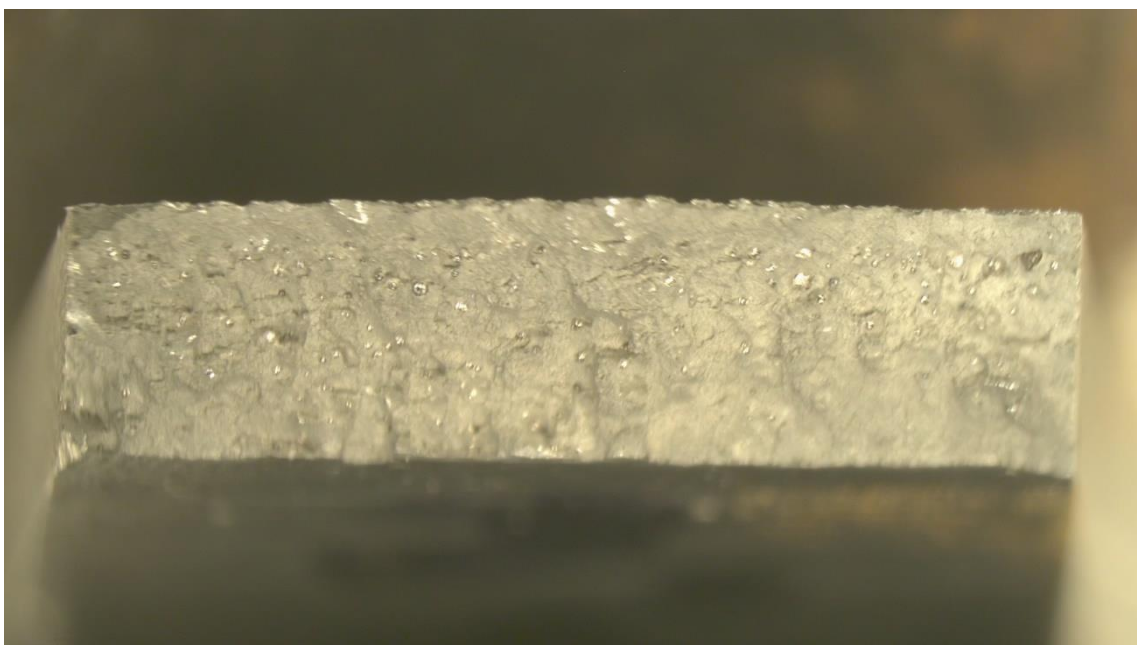


Figure 3. 28 Optically observed top view of fracture surface of specimen 3

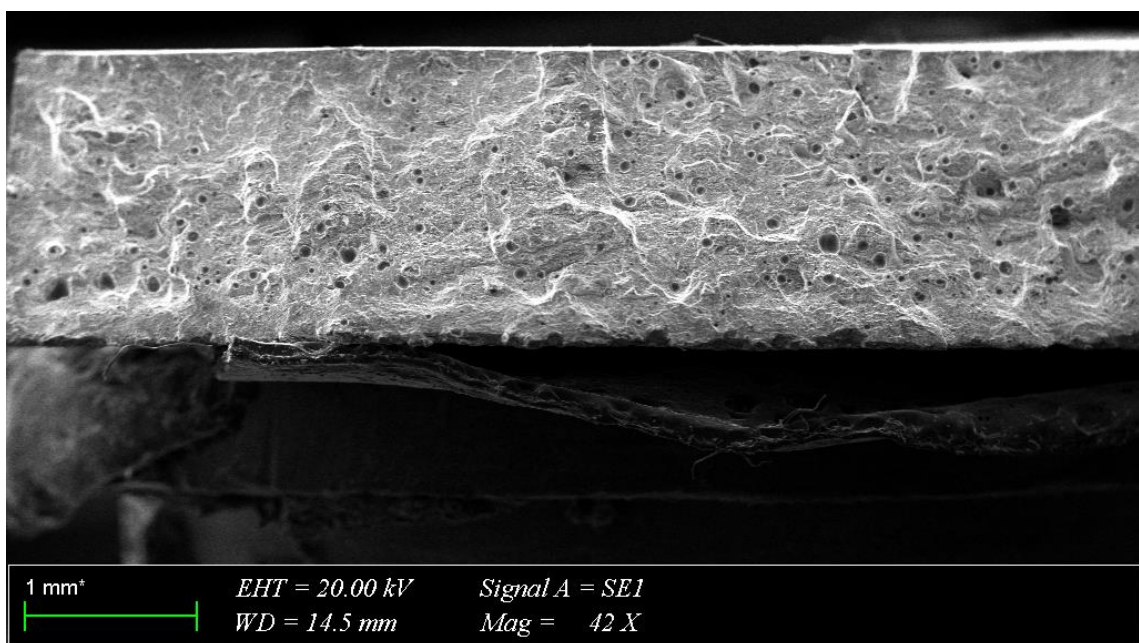


Figure 3. 29 SEM observed fracture surface of specimen 3 (42X)

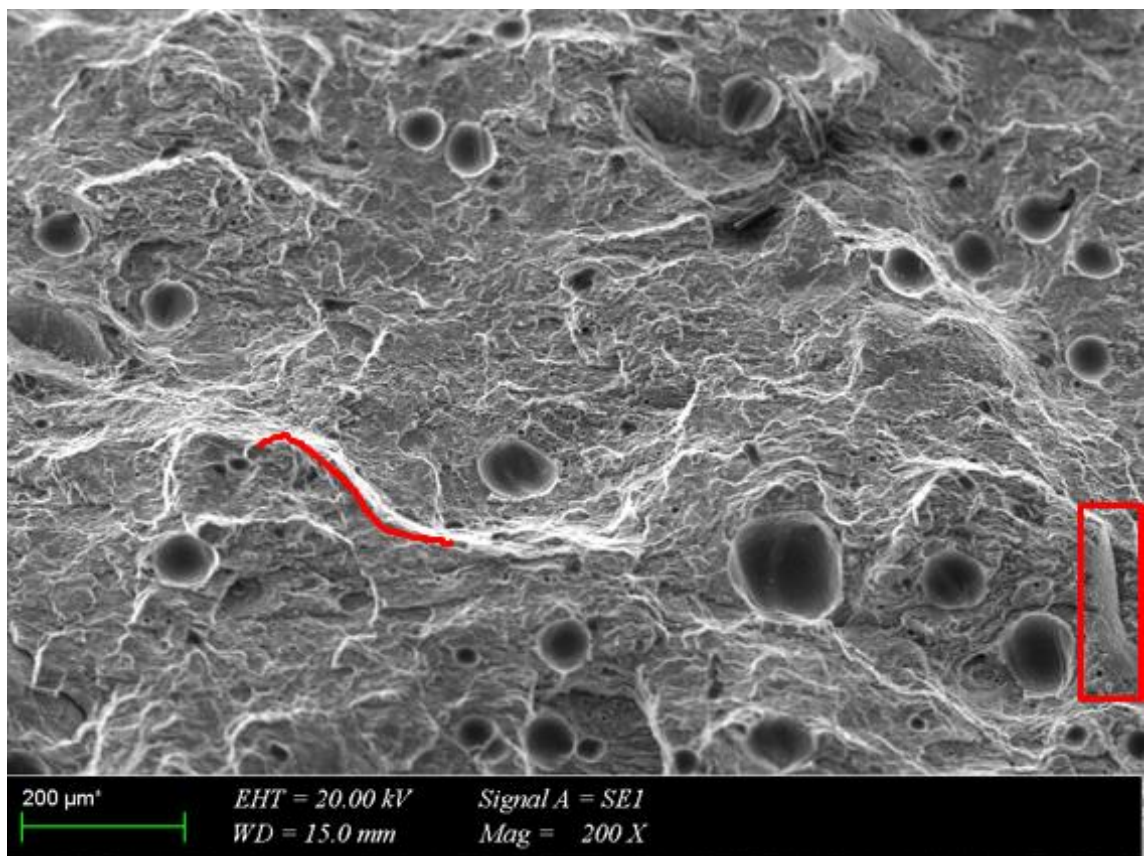


Figure 3. 30 SEM observed fracture surface of specimen 3 (200X)

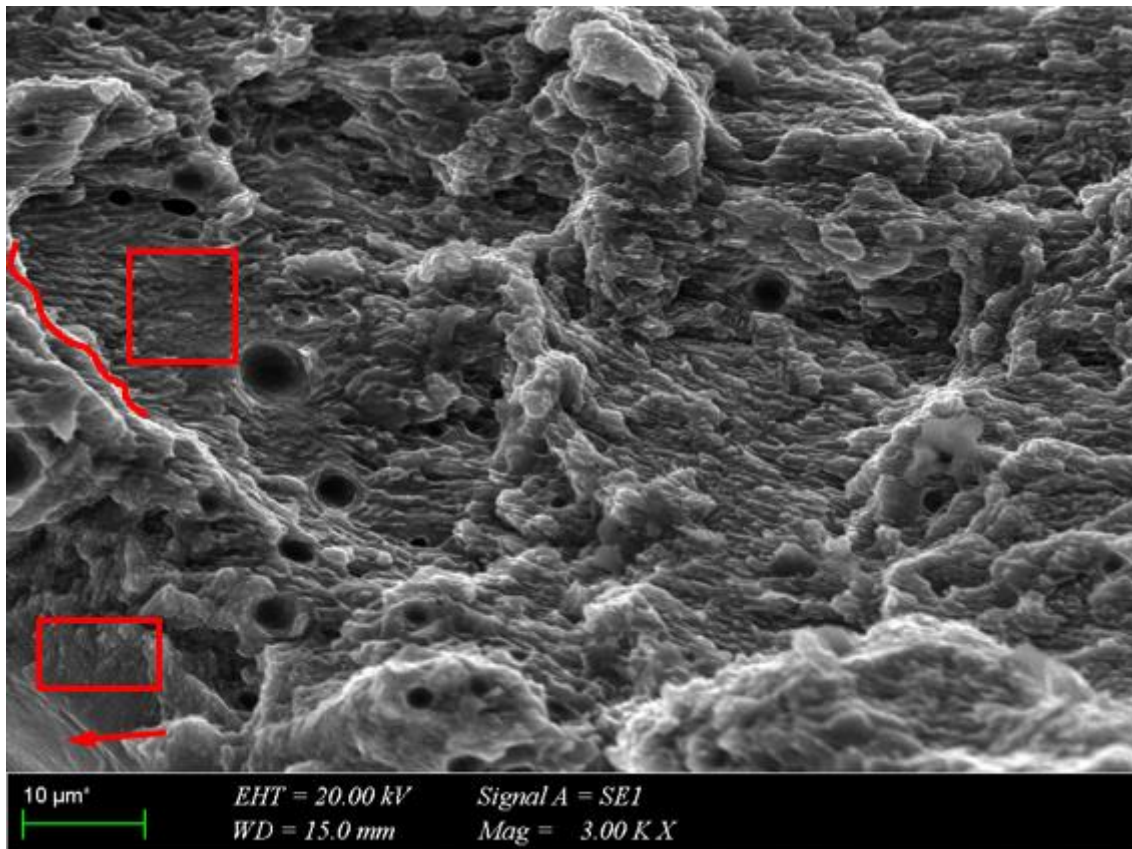


Figure 3. 31 SEM observed fracture surface of specimen 3 (3000X)

In addition to the OM observations, the above three figures show detailed scanning electron microscope images. In figure 3.30, shallow dimples, tear ridges and cleavage facets were shown. Also, figure 3.31, demonstrates river lines. In view of such information of optical and SEM, it is concluded that the fracture mechanism of specimen 3 exhibits not highly ductile or brittle but moderately ductile or brittle-ductile mixed fracture mechanism.



Figure 3. 32 Tensile specimen 4

In figure 3.32, the fracture mechanism of specimen 4 is shown. In a similar manner to specimen 3, the cross-sectional area of the specimen does not change on the macro scale. Also, the fibrous fracture with 45 degrees between the failed parts is very similar to specimen 3. However, instead of both end shear lips, at one end a shear lip is observed. Even though shear lips and 45 degrees between the failed parts, the fracture mechanism of specimen 4 is not exhibit full cup and mechanism.

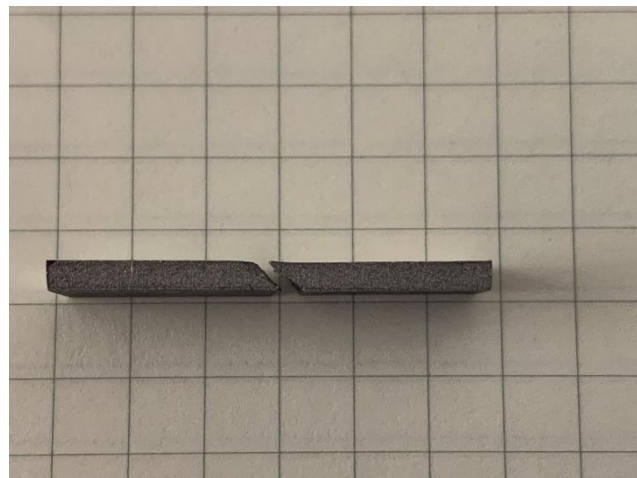


Figure 3. 33 Side view of fractured part of specimen 4



Figure 3. 34 Top view of fractured part of specimen 4

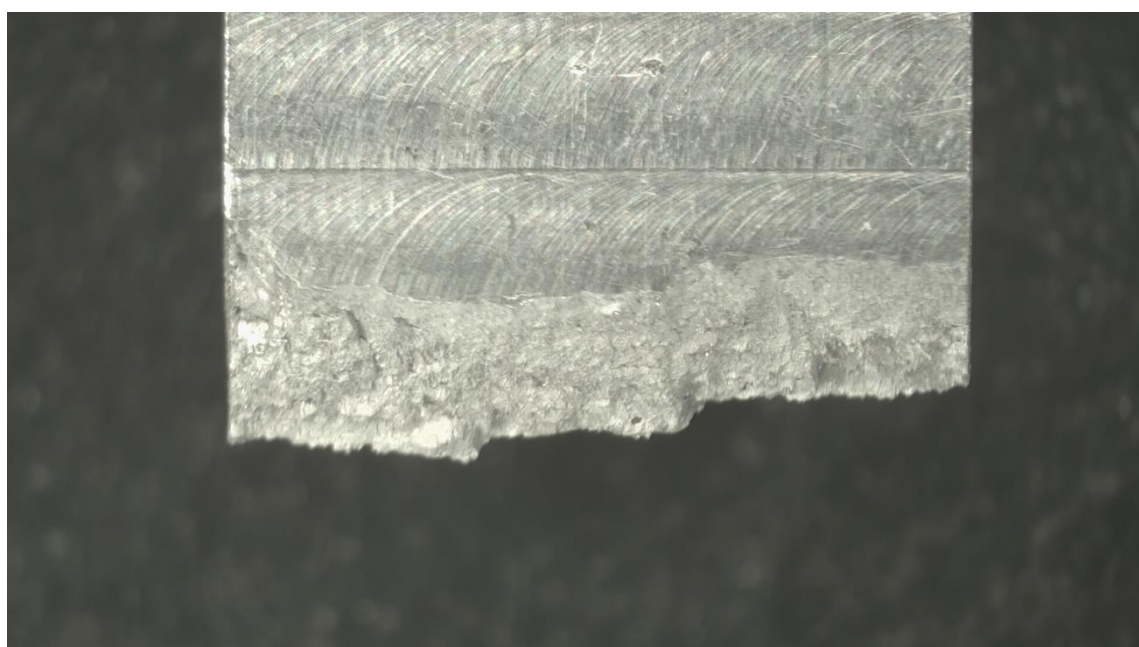


Figure 3. 35 Optically observed side view of fracture surface of specimen 4

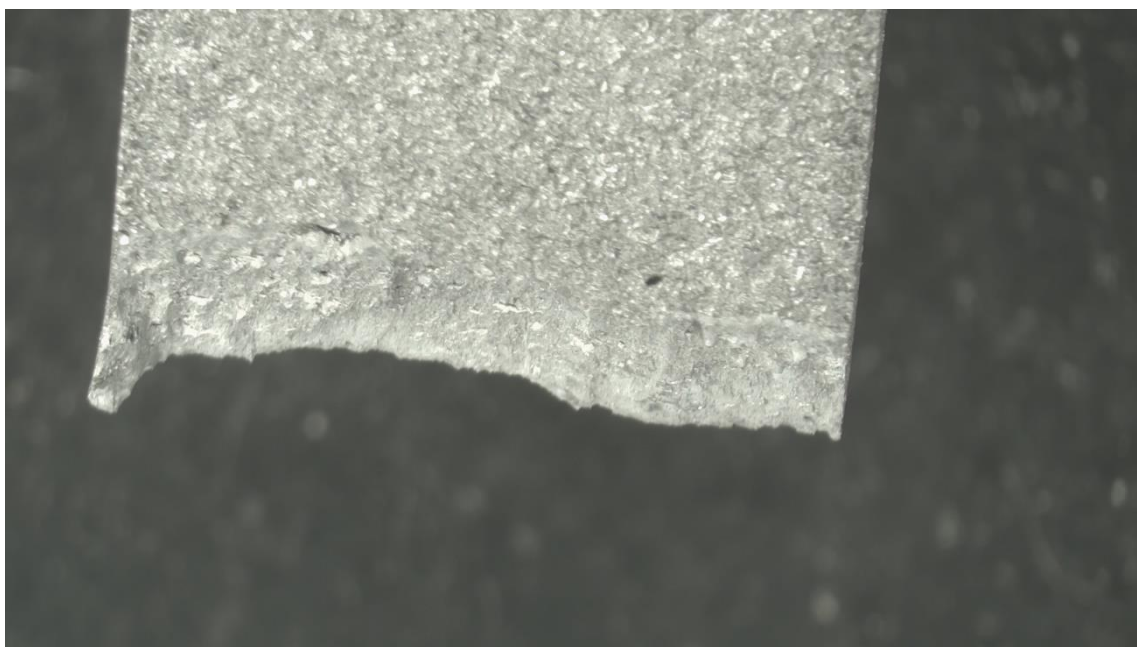


Figure 3. 36 Optically observed side view of fracture surface of specimen 4



Figure 3. 37 Optically observed top view of fracture surface of specimen 4

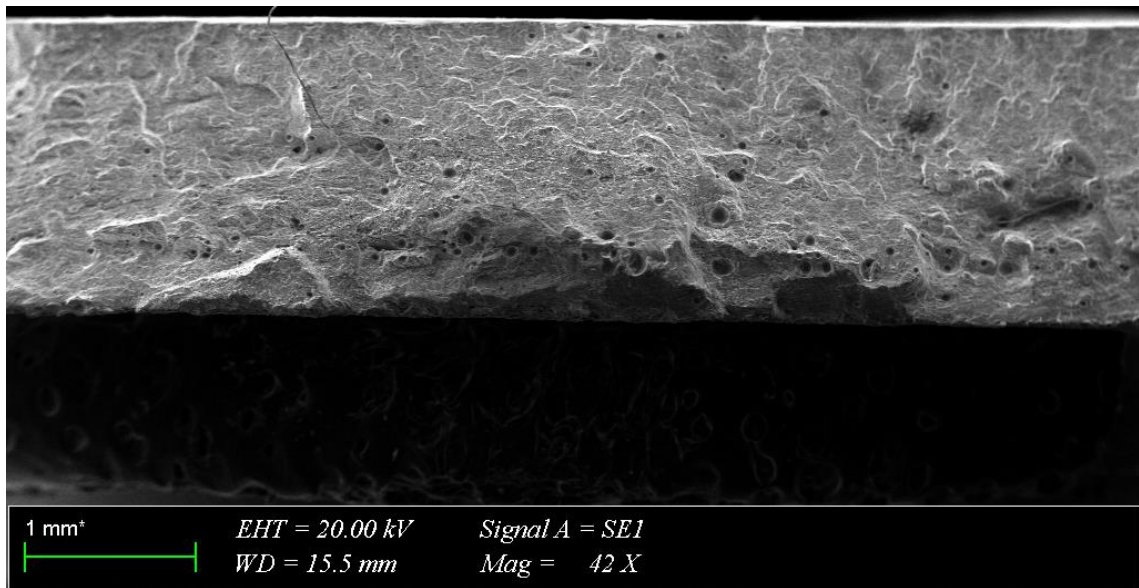


Figure 3. 38 SEM observed fracture surface of specimen 4 (42X)

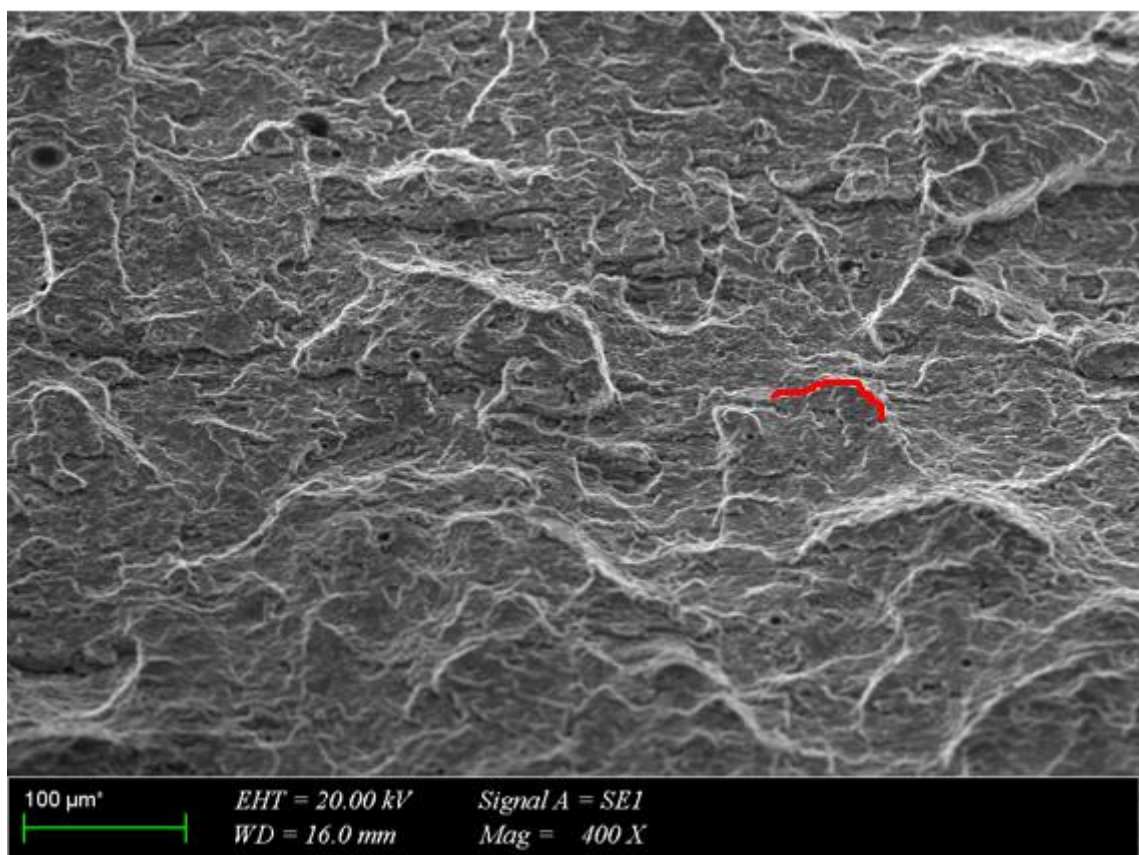


Figure 3. 39 SEM observed fracture surface of specimen 4 (400X)

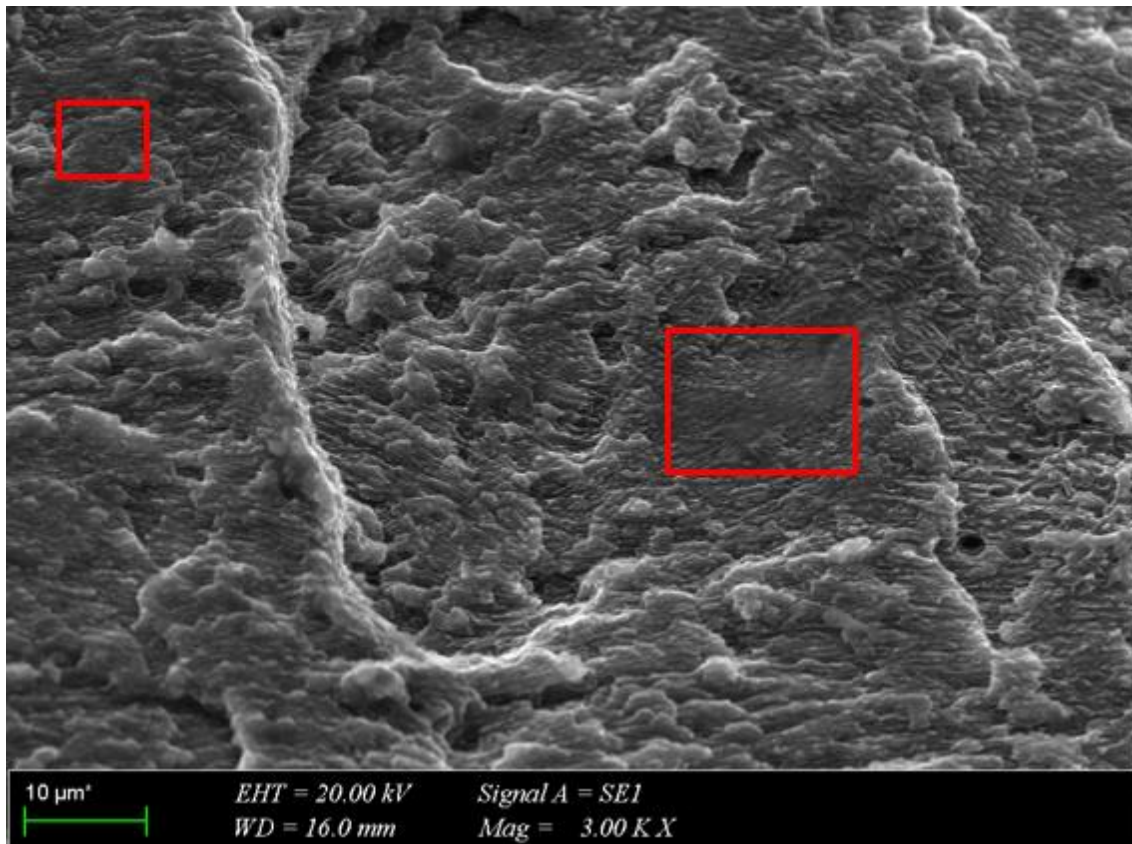


Figure 3. 40 SEM observed fracture surface of specimen 4 (3000X)

Like specimen 3, shallow dimples, tear ridges and cleavage facets, river lines shown in the above figures. As a result, fracture mechanism of specimen 4 can be regarded as moderate ductility or brittle-ductile-fracture mechanism as it is stressed above paragraph.



Figure 3. 41 Tensile specimen 5

In figure 3.41, the fracture mechanism of specimen 5 is shown. The cross-sectional area of the specimen does not change and 45 degrees between failed parts are seen. That is what is expected after specimens 3 and 4. However, shear lips and cup and cone type of fracture are not seen as much as 3 and 4.



Figure 3. 42 Side view of fractured part of specimen 5

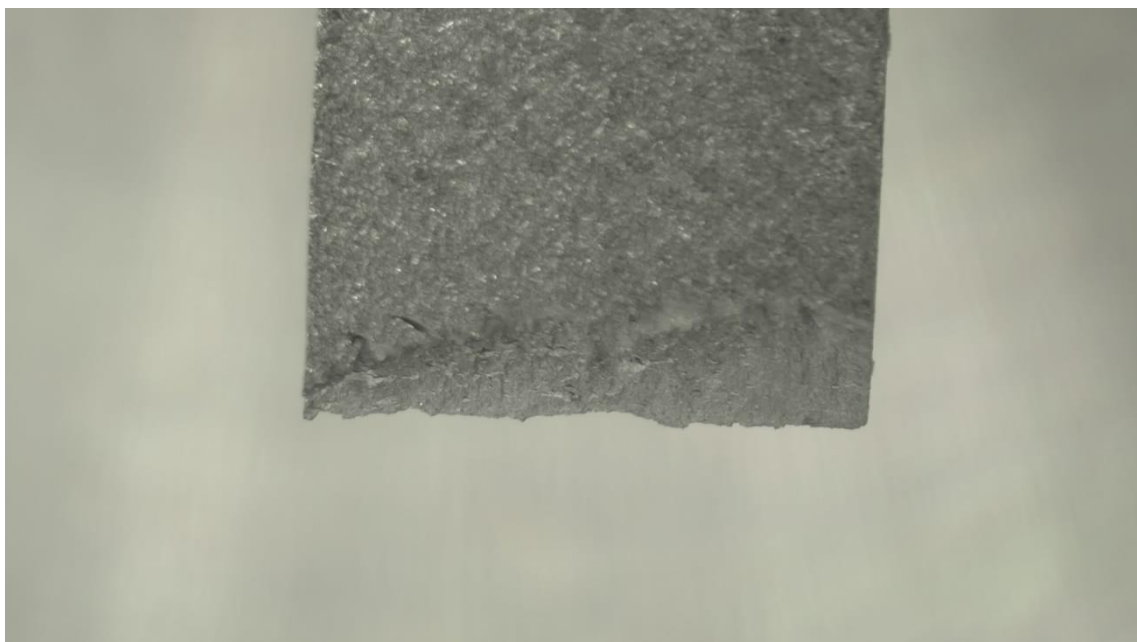


Figure 3. 43 Optically observed side view of fracture surface of specimen 5

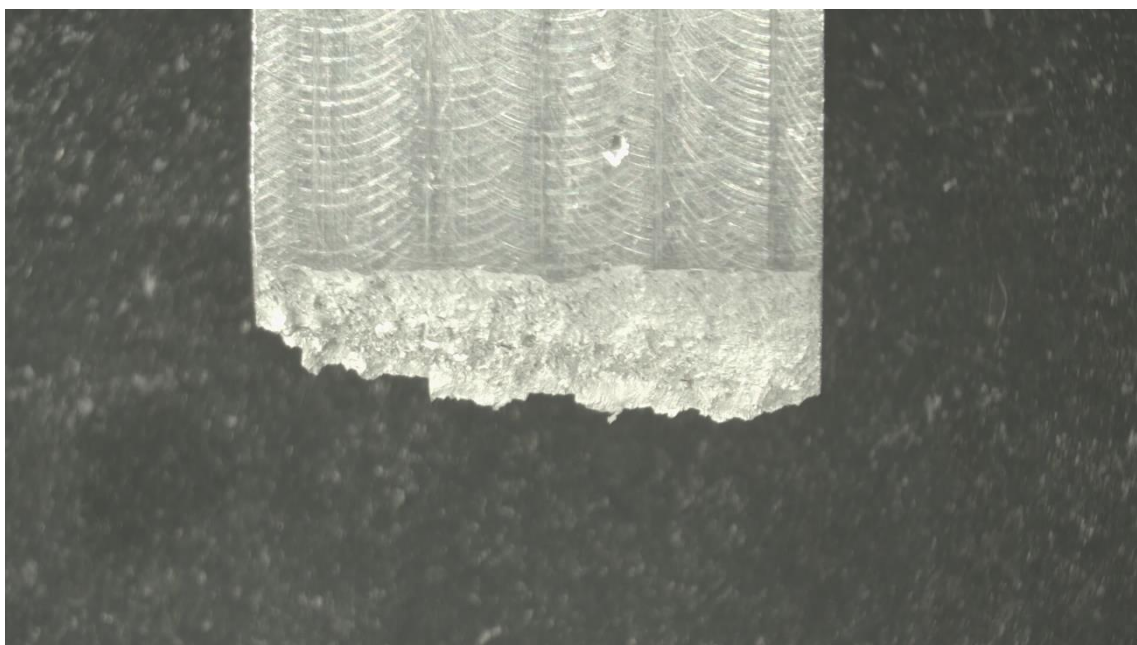


Figure 3. 44 Optically observed side view of fracture surface of specimen 5

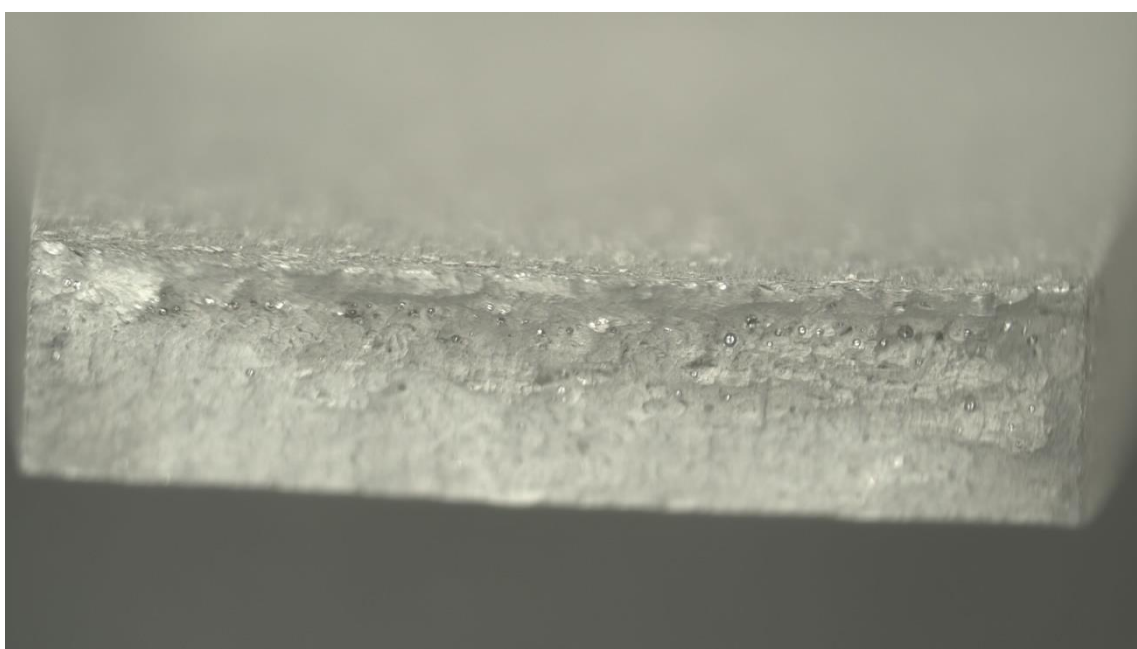


Figure 3. 45 Optically observed top view of fracture surface of specimen 5

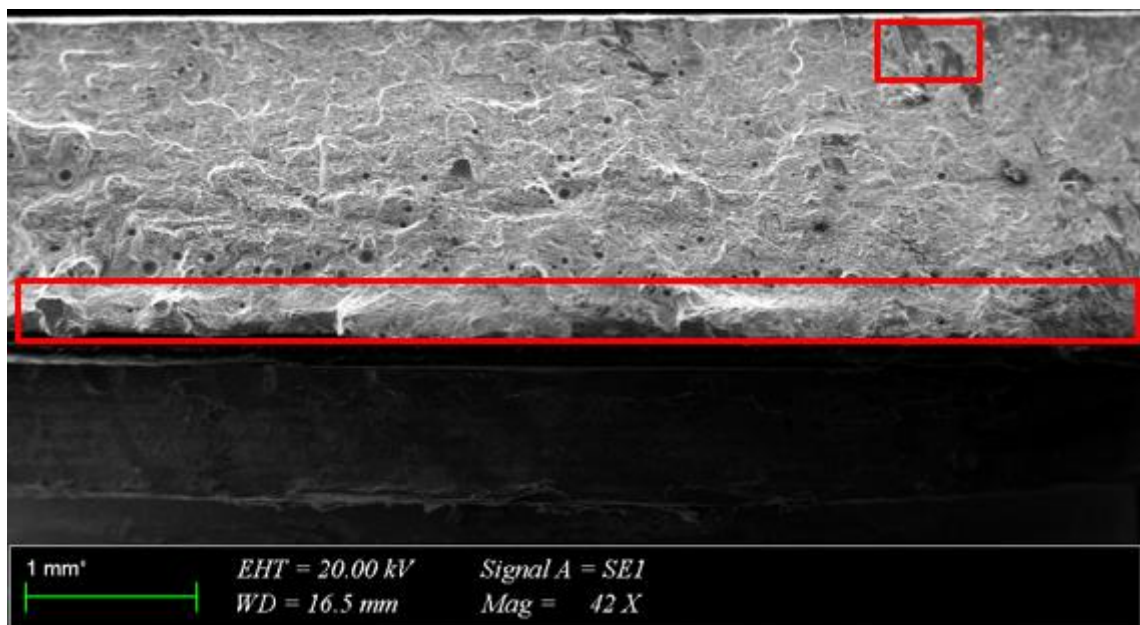


Figure 3. 46 SEM observed fracture surface of specimen 5 (42X)

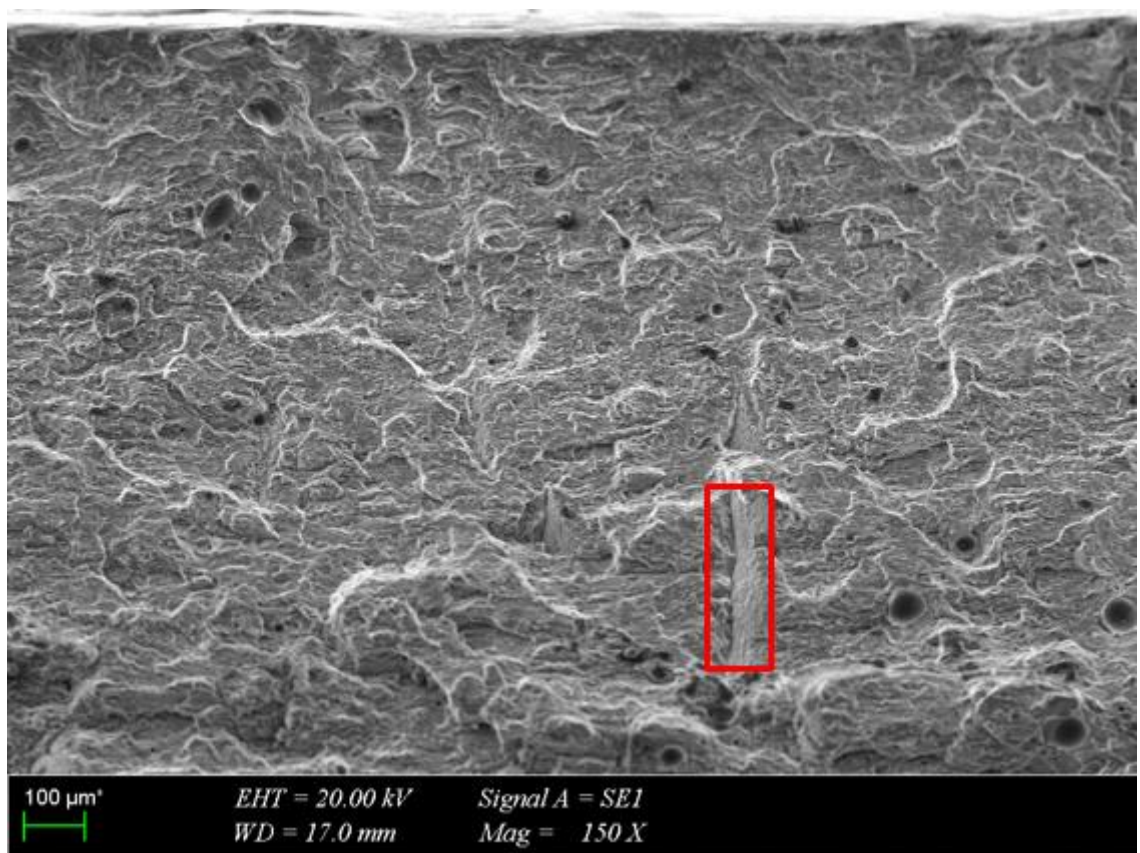


Figure 3. 47 SEM observed fracture surface of specimen 5 (150X)

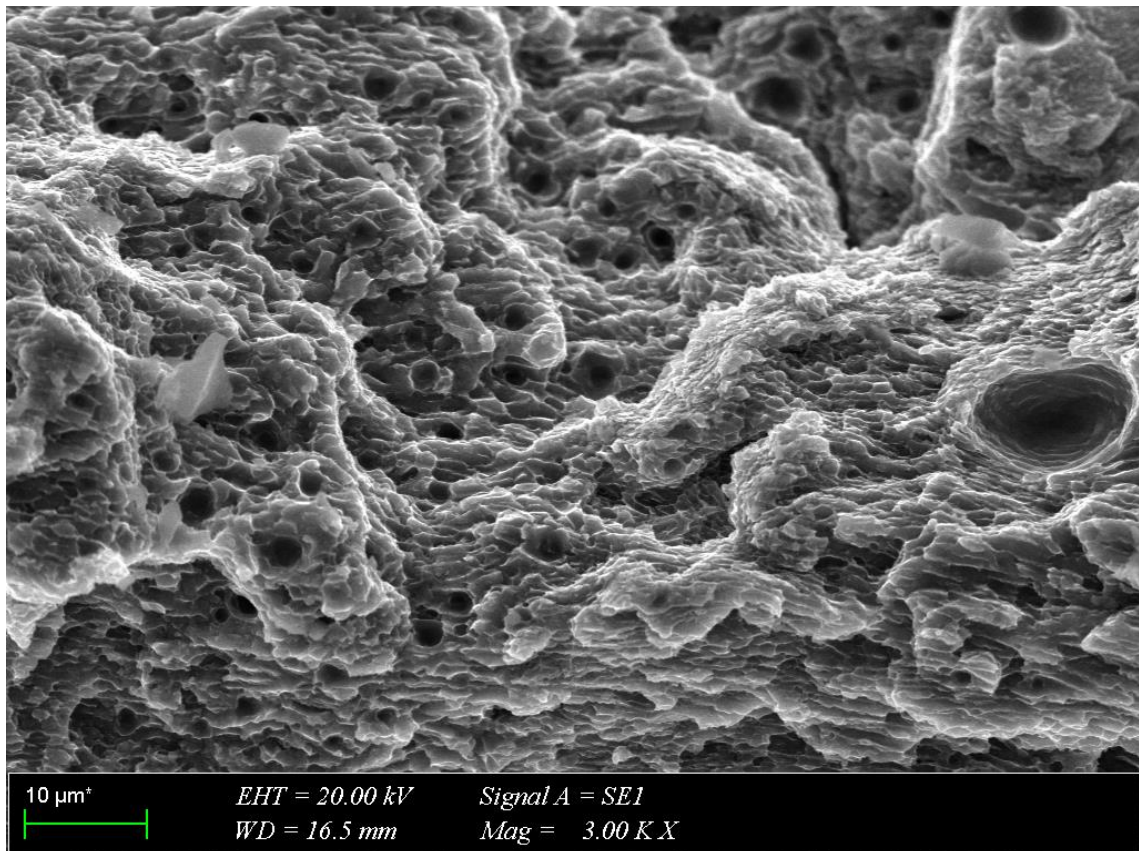


Figure 3. 48 SEM observed fracture surface of specimen 5 (3000X)

Likewise, in specimens 3 and 4, the fracture mechanism of specimen 5 can be concluded as a brittle-ductile mixed fracture or moderately ductile fracture after observing microscope images.

3.6.2. Charpy Fractures

In the figures, the fracture mechanism of Charpy test specimens 1,2 and 3 are shown, respectively. Additional to the OM, for specimens 1 and 2 SEM images were taken.



Figure 3. 49 Charpy Impact Tested Specimens

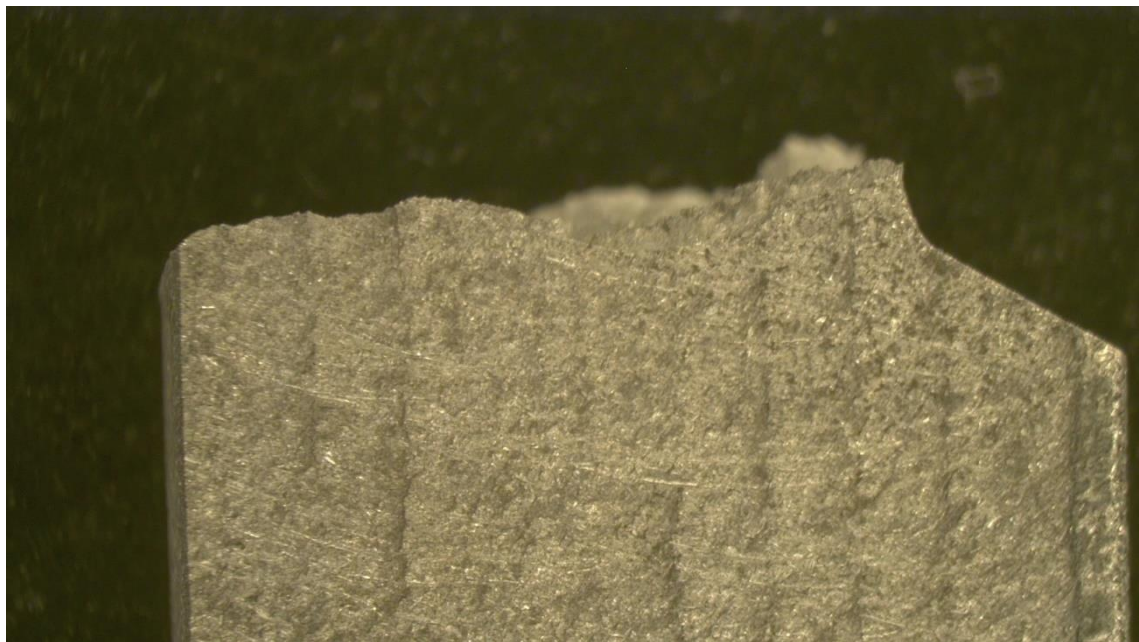


Figure 3. 50 Optically observed side view of Charpy specimen 1

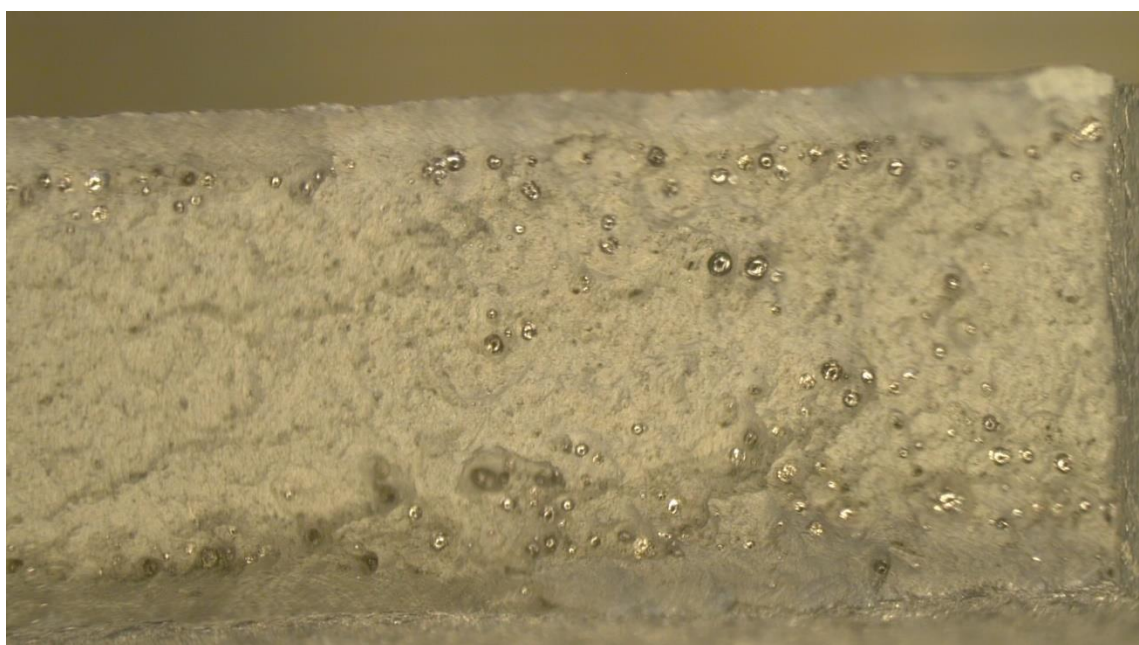


Figure 3. 51 Optically observed top view of Charpy specimen 1

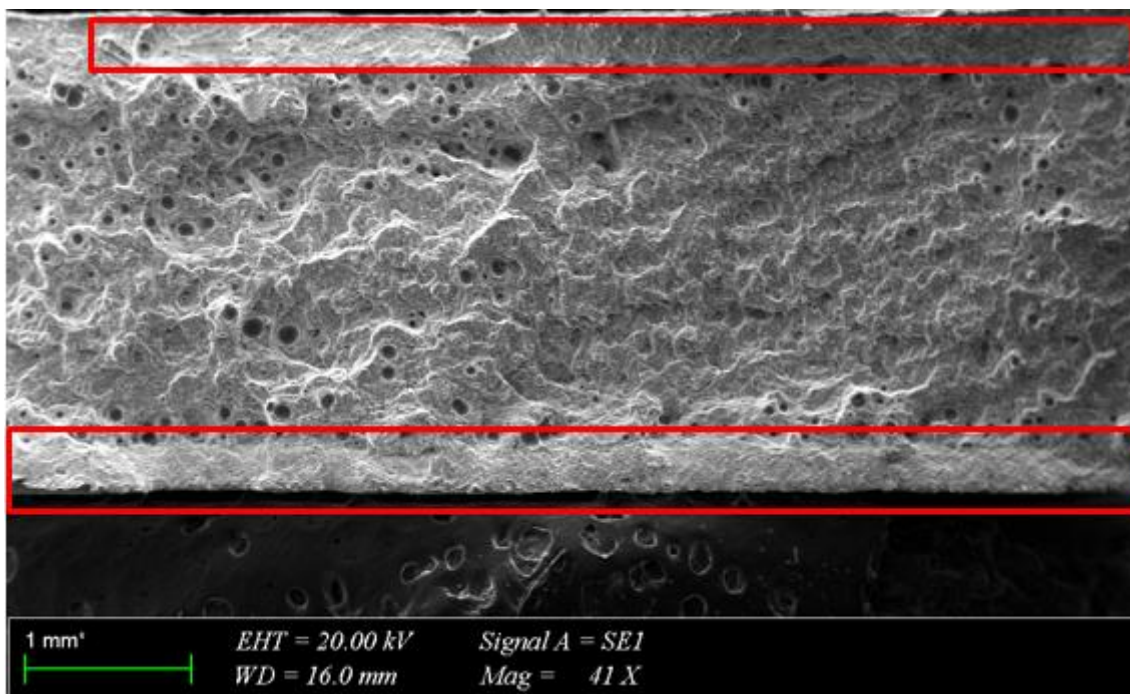


Figure 3. 52 SEM observed fracture surface of Charpy specimen 1 (41X)

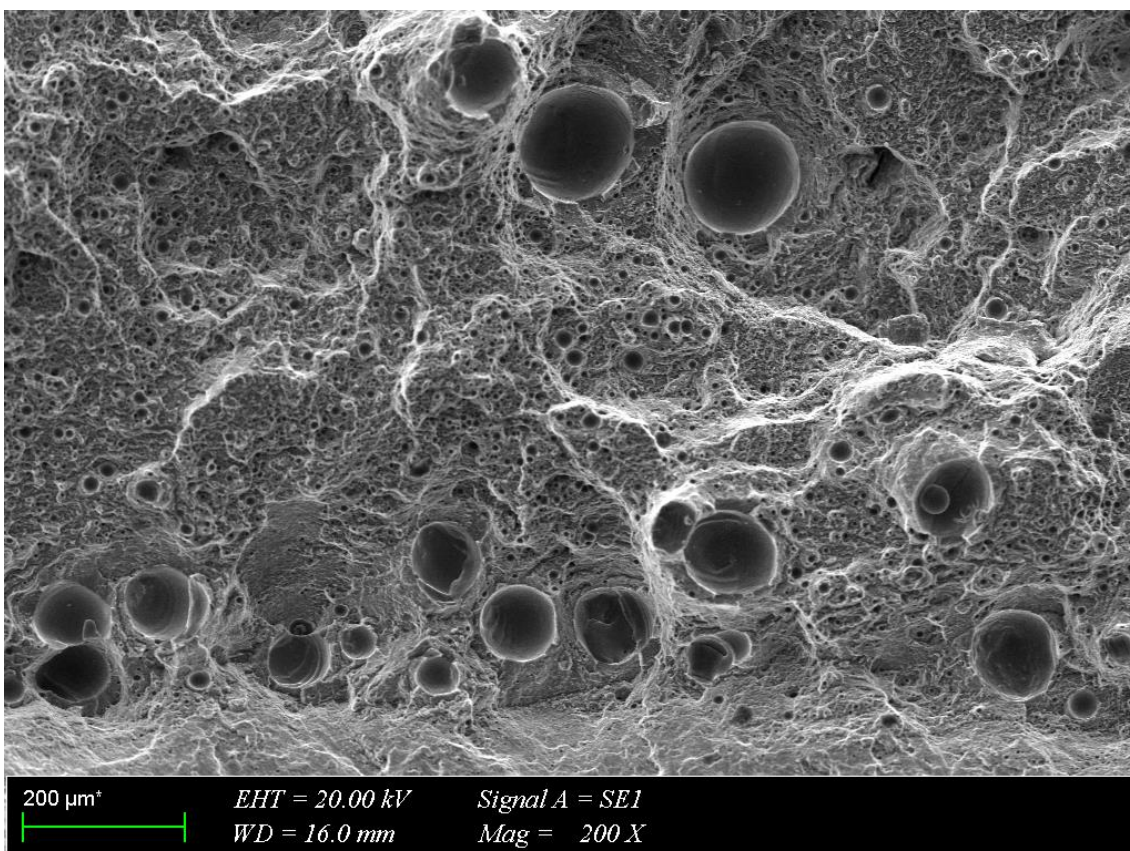


Figure 3. 53 SEM observed fracture surface of Charpy specimen 1 (200X)

In figure 3.52 of Charpy specimen 1 shows tear ridges at the bottom and the top of the part. Also, in figure 3.53 micro-voids dimples were exhibited. Moreover, the first OM image demonstrates resistance to failure.

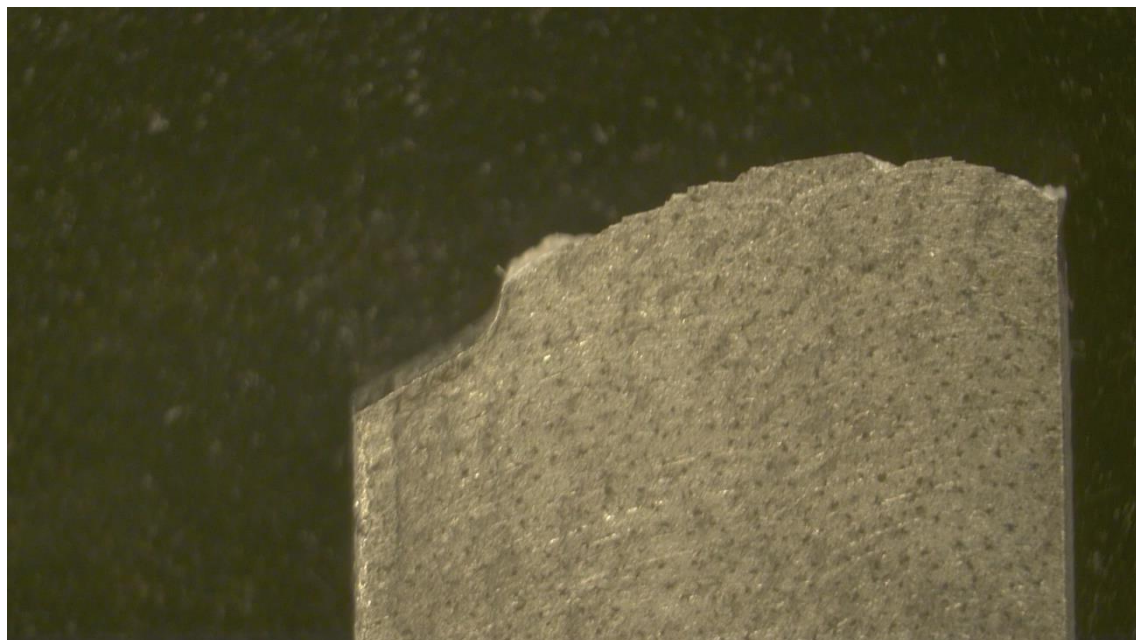


Figure 3. 54 Optically observed side view of Charpy specimen 2

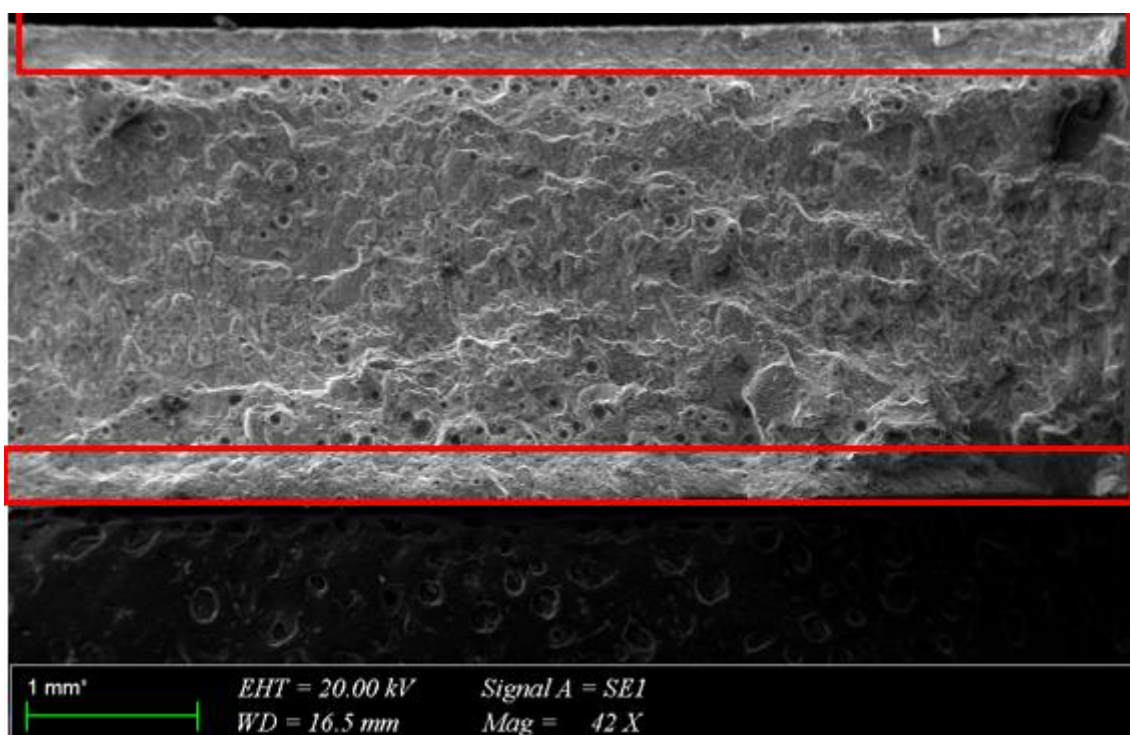


Figure 3. 55 SEM observed fracture surface of Charpy specimen 2 (42X)

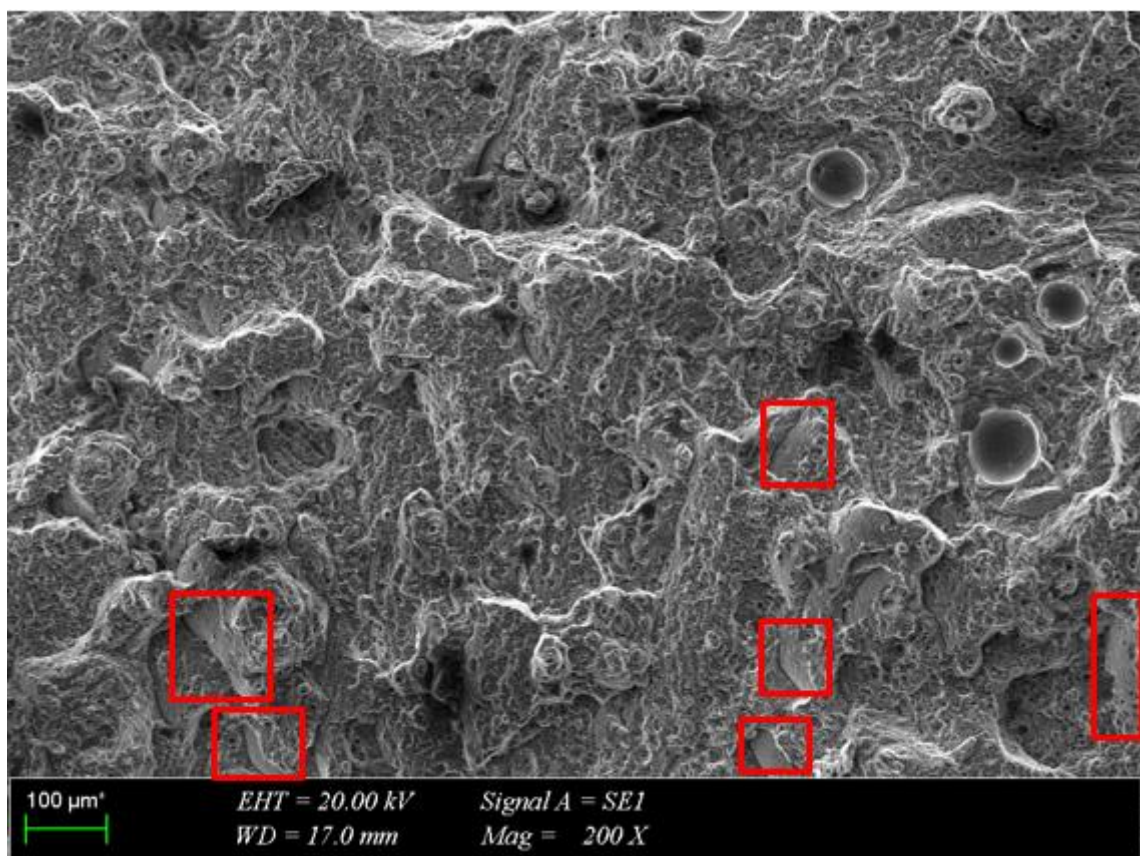


Figure 3. 56 SEM observed fracture surface of Charpy specimen 2 (200X)

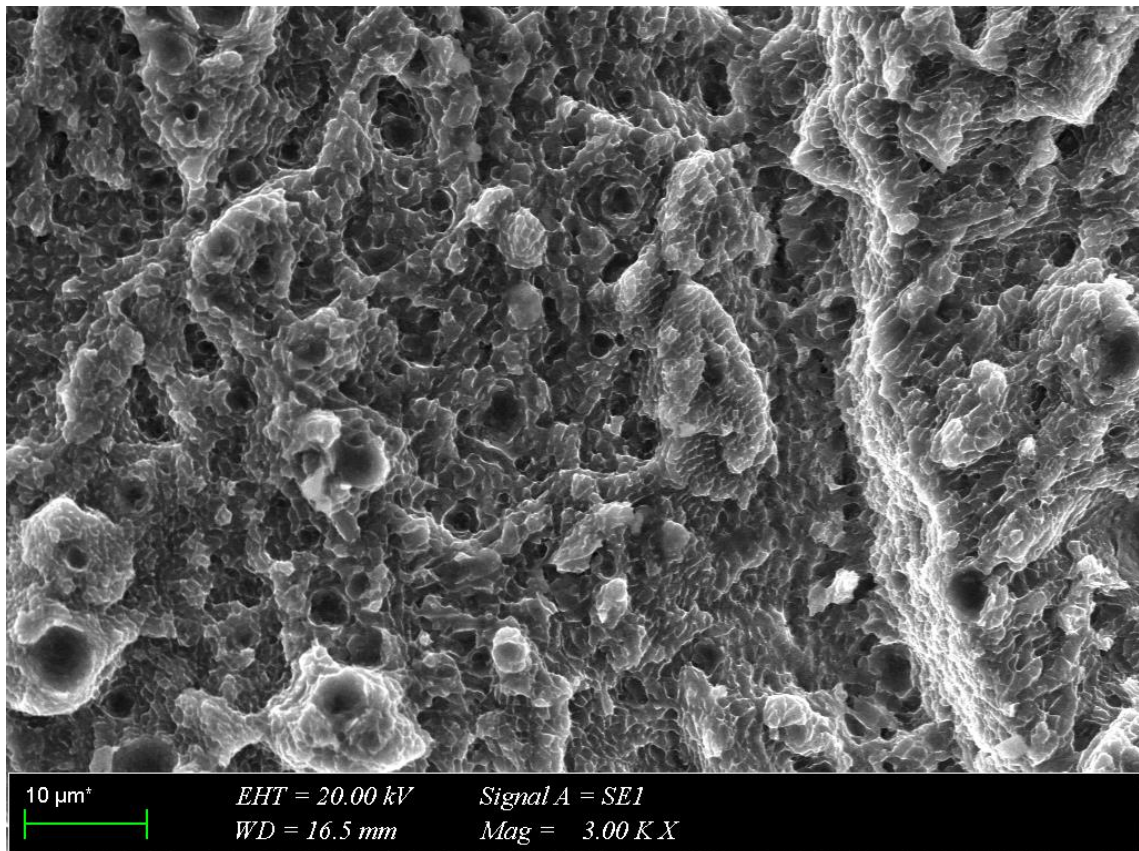


Figure 3. 57 SEM observed fracture surface of Charpy specimen 2 (3000X)

Figure 3.56 of Charpy specimen 2 shows cleavage facets, clearly. In addition, figure 3.57 demonstrates voids.

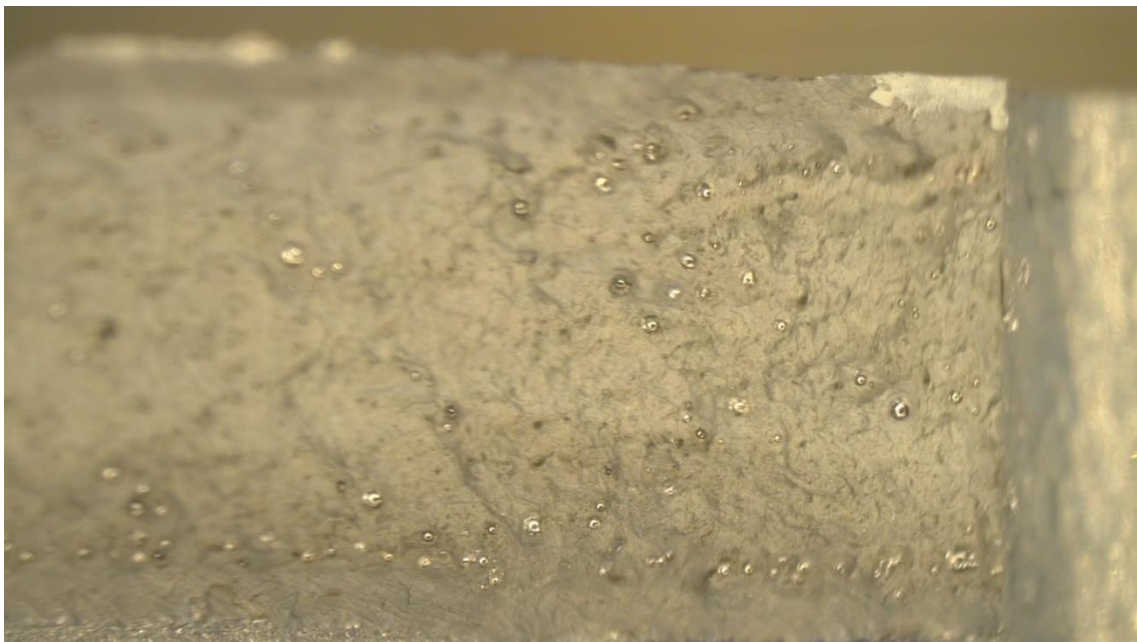


Figure 3. 58 Optically observed top view of Charpy specimen 2

From the OM observations of Charpy Specimen 3 tendency of resistance to fail can be seen.

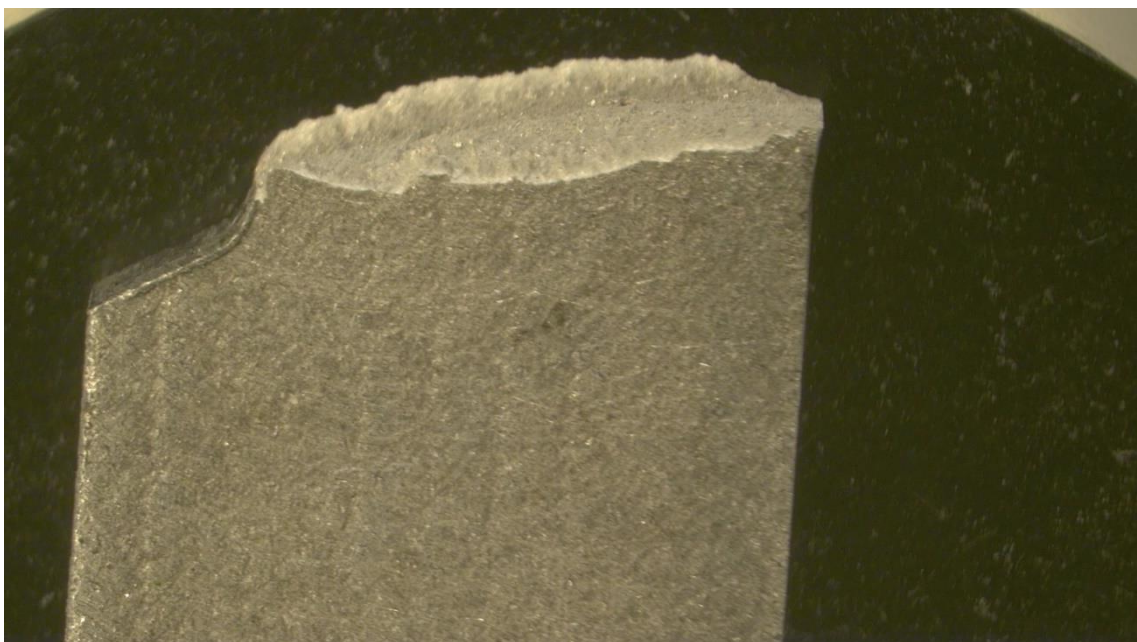


Figure 3. 59 Optically observed side view of Charpy specimen 3



Figure 3. 60 Optically observed top view of Charpy specimen 3

Fractures of Charpy tests neither exhibit completely ductile as it is seen in figure 1.30 nor brittle ductile in the same figure. Although they resist to failing which resembles a ductile manner, it cannot be classified as a completely ductile fracture because of ridges and facets. As a result, fractures of Charpy's are considered moderately ductile fractures.

4. EVALUATION of CURRENT WORK from MUDEK PERSPECTIVE

4.1. Economic Analysis

This project was supported by the Lift-Up Program Turkish Aerospace Industry, and TUBITAK 2209B. Therefore, invoiced expenses were paid by TAI.

Table 4. 1 Expenses

Wire Erosion Machining of Specimens	1180 TL
SEM Analysis	1120,45 TL
Hardness Test	557,55 TL

4.2. Real-Life Conditions

In real life, the use of AM has been increasing since the 1980s. Moreover, AM will take an essential place in industry 4.0 thanks to its innovative advantages. AM allows for easy control of the microstructure and mechanical properties. We investigated the relationship between microstructure and mechanical properties of AlSi10Mg specimens which are produced by laser PBF. In daily life, planes and automobiles require lightweight materials. That's why we used AlSi10Mg in our study. Acquiring microstructure and mechanical properties results will contribute to literature and related areas such as the automotive and aerospace industries.

4.3. Productivity

Since AM offers to adjust the more flexible microstructure and mechanical properties than conventional manufacturing methods, process parameters are vital to acquire desired material characteristics. For instance, laser power, scanning velocity, layer thickness, and hatching distance are effective parameters of the microstructure and mechanical properties. Therefore, these parameters can be changed to acquire different characteristics within this topic.

4.4. Constraints

In this study, the only but, unfortunately, very affecting factor is the number of specimens, which fell short of our expectations. Although within the scope of the thesis, specimens were provided by the Turkish Aerospace Industry, the numbers of the specimen and their dimensions were not sufficient to compare post-processed and as-built samples. Because, to have experimented with high reliability, such as tensile test and Charpy test, an experiment requires at least five samples. Therefore, the project encompasses as-built conditions in detail but does not compare post-processed and as-built samples due to the scarcity of specimen amount.



Figure 4. 1 Total weight of specimens

5. CONCLUSIONS and RECOMMENDATIONS for FURTHER WORKS

5.1. Conclusions of the Current Work

In the scope of this thesis, mechanical properties, fracture mechanism and macro- and microstructure of additively manufactured AlSi10Mg were investigated. Tensile test, Charpy impact test, density test and hardness test were applied to identify the characteristic of the material by relevant standards. To observe the microstructure of the material metallographic specimens were prepared. Then, mechanical properties were related to the microstructure of the additively manufactured AlSi10Mg.

Firstly, the tensile test and the Charpy test were applied. As a result of the tensile test, the material neither was showed completely brittle material nor ductile material. UTS was nearly located at the FS point. However, the specimens showed some resistance against breaking when they reached the plastic region. At the end of the tensile test results, the stress-strain graph showed moderately ductile or ductile-brittle mixed material properties. Average values of yield strength, ultimate tensile strength and FS were 174.83, 356.45 and 354.42 respectively, Also, mean elongation was recorded as 5.076 %. When these results were compared with as-built cast-produced AlSi10Mg, AM AlSi10Mg has higher yield strength and ultimate tensile strength which can be attributed to the manufacturing method. But, in some cases, as-built AM AlSi10Mg demonstrated less elongation than as-built cast-produced ones possibly due to process parameters of different studies. The average results after the Charpy tests were 1.4 kN maximum load, 0.102 J/cm² crack initiation resistance, 0.135 J/cm² crack propagation resistance, 0.237 J/cm² total crack resistance, 7.46 mm maximum displacement and 0.038 J/mm² absorbed energy per area. The average results of absorbed energy per area equal to as-built cast-produced ones. One of the main properties of ductile materials is absorbed energy increases as maximum displacement increases. Some of the specimens showed that some of them did not show. Hence, Charpy test results showed that ductile-brittle mixed material is similar to tensile test results.

Secondly, density of the material was measured, and hardness tests were applied. The density of the material exhibits 2.6355 and relative density is 98%. In other words, there is 2% porosity in the material. When results were compared, the average density of as-

built AM AlSi10Mg less than the density of the as-built cast-produced AlSi10Mg, that can be attributed to the porosity level which is the inherent property of the additive manufacturing process. Since our specimen thicknesses were subsized, Vickers microhardness tests were applied. The Vickers microhardness test results were compared with cast AlSi10Mg microhardness results acquired from literature. Additively manufactured AlSi10Mg Vickers microhardness results were higher than cast AlSi10Mg. Moreover, our results were validated with the other studies in the literature. The result from the hardness test can be correlated with the ultra-fine microstructure due to fast cooling thanks to the manufacturing process of the additively manufactured AlSi10Mg.

Thirdly, macro- and microstructure and fracture mechanism of the material was investigated by optical and scanning electron microscope. Microstructural observation with the optical microscope showed layer-by-layer morphology at the side view that can be attributed to the additive manufacturing process, and laser scans at the top view. In some figures, relatively large pores were shown that could be attributed to hydrogen, oxygen, and humidity levels in the manufacturing area. Also, the arrangement of laser scan tracks revealed an angled scanning direction. Besides that, SEM microstructural observations exhibit fine, coarse regions of Al-Si dendrites and heat-affected zones. Pores which were observed with the optical microscope, were investigated with EDX analysis. Oxygen and Copper were found. In addition to that, irregularly shaped pores were observed that can be attributed to the lack of fusion. When it comes to the fracture surfaces, macroscopic observation of the fracture mechanism showed that no enlargement at the cross-sectional area and 45 degrees of fracture angle was observed at all fractured parts. However, optical microscope observations presented resistance to failure like the cup-cone mechanism. Furthermore, SEM showed dimples which resemble ductile fracture mechanisms, tear ridges, river lines and cleavage facets which were found in brittle fracture mechanisms. Therefore, the fracture mechanism of additively manufactured AlSi10Mg was concluded as a ductile-brittle mixed fracture mechanism.

To conclude, AM is a new and promising method, produced materials require studies about characteristics. Results were founded in this study demonstrated that AM as-built AlSi10Mg has higher yield strength, ultimate tensile strength, microhardness but less density than as-built cast-produced AlSi10Mg. Also, fracture surfaces of as-built additively manufactured AlSi10Mg exhibited ductile-brittle mixed fracture mechanism.

Therefore, this study contributes to the literature in terms of mechanical properties, fracture mechanism and microstructure relationship of AlSi10Mg produced via laser PBF. In future studies, a comprehensive comparison of post-processed and as-built additively manufactured of AlSi10Mg can be selected as a subject.

5.2. Recommendations for Further Works

- Since process parameters such as the laser power, scanning speed, build plate temperature, hatching distance, vertical and horizontal orientation directly affect the mechanical properties and the microstructure, they can be changed and compared to each other to acquire optimized results.
- Post-processes for example, T5, T6, stress relieving and HIP can be applied to AlSi10Mg alloys produced by casting and AM. After that, mechanical properties, microstructures, and fracture surfaces can be examined.

REFERENCES

- [1] Girelli, L., Tocci, M., Gelfi, M., & Pola, A. (2019). Study of heat treatment parameters for additively manufactured AlSi10Mg in comparison with corresponding cast alloy. *Materials Science and Engineering: A*, 739, 317-328.
- [2] Dong, M., Zhou, W., Kamata, K., & Nomura, N. (2020). Microstructure and mechanical property of graphene oxide/AlSi10Mg composites fabricated by laser additive manufacturing. *Materials Characterization*, 170, 110678.
- [3] Ertuğrul, O., Öter, Z. Ç., Yılmaz, M. S., Şahin, E., Coşkun, M., Tarakçı, G., & Koç, E. (2020). Effect of HIP process and subsequent heat treatment on microstructure and mechanical properties of direct metal laser sintered AlSi10Mg alloy. *Rapid Prototyping Journal*.
- [4] Tradowsky, U., White, J., Ward, R. M., Read, N., Reimers, W., & Attallah, M. M. (2016). Selective laser melting of AlSi10Mg: Influence of post-processing on the microstructural and tensile properties development. *Materials & Design*, 105, 212-222.
- [5] Froes, F. H., & Dutta, B. (2014). *The additive manufacturing (AM) of titanium alloys* (Vol. 1019, pp. 19-25). Trans Tech Publications Ltd.
- [6] Herzog, D., Seyda, V., Wycisk, E., & Emmelmann, C. (2016). Additive manufacturing of metals. *Acta Materialia*, 117, 371-392.
- [7] Aboulkhair, N. T., Simonelli, M., Parry, L., Ashcroft, I., Tuck, C., & Hague, R. (2019). 3D printing of Aluminium alloys: Additive Manufacturing of Aluminium alloys using selective laser melting. *Progress in materials science*, 106, 100578.
- [8] Shakil, S. I., Hadadzadeh, A., Amirkhiz, B. S., Pircazi, H., Mohammadi, M., & Haghshenas, M. (2021). Additive manufactured versus cast AlSi10Mg alloy: Microstructure and micromechanics. *Results in Materials*, 10, 100178.
- [9] Everett, R. K., Duffy, M. E., Storck, S. M., & Zupan, M. (2020). A variogram analysis of build height effects in an additively manufactured AlSi10Mg part. *Additive Manufacturing*, 35, 101306.
- [10] Brandl, Erhard, et al. "Additive manufactured AlSi10Mg samples using Selective Laser Melting (SLM): Microstructure, high cycle fatigue, and fracture behavior." *Materials & Design* 34 (2012): 159-169.
- [11] Zhou, Y., Ning, F., Zhang, P., & Sharma, A. (2021). Geometrical, microstructural, and mechanical properties of curved-surface AlSi10Mg parts fabricated by powder bed fusion additive manufacturing. *Materials & Design*, 198, 109360.
- [12] Zhou, L., Mehta, A., Schulz, E., McWilliams, B., Cho, K., & Sohn, Y. (2018). Microstructure, precipitates and hardness of selectively laser melted AlSi10Mg alloy before and after heat treatment. *Materials Characterization*, 143, 5-17.

- [13] Wu, J., Wang, X. Q., Wang, W., Attallah, M. M., & Loretto, M. H. (2016). Microstructure and strength of selectively laser melted AlSi10Mg. *Acta Materialia*, 117, 311-320.
- [14] Liu, X., Zhao, C., Zhou, X., Shen, Z., & Liu, W. (2019). Microstructure of selective laser melted AlSi10Mg alloy. *Materials & Design*, 168, 107677.
- [15] Liu, M., Wei, K., Yue, X., Huang, G., Deng, J., & Zeng, X. (2022). High power laser powder bed fusion of AlSi10Mg alloy: Effect of laser beam mode. *Journal of Alloys and Compounds*, 909, 164779.
- [16] Cao, Y., Lin, X., Wang, Q. Z., Shi, S. Q., Ma, L., Kang, N., & Huang, W. D. (2021). Microstructure evolution and mechanical properties at high temperature of selective laser melted AlSi10Mg. *Journal of Materials Science & Technology*, 62, 162-172.
- [17] Uzan, N. E., Shneck, R., Yeheskel, O., & Frage, N. (2017). Fatigue of AlSi10Mg specimens fabricated by additive manufacturing selective laser melting (AM-SLM). *Materials Science and Engineering: A*, 704, 229-237.
- [18] Syed, W. U. H., Pinkerton, A. J., & Li, L. (2005). A comparative study of wire feeding and powder feeding in direct diode laser deposition for rapid prototyping. *Applied surface science*, 247(1-4), 268-276.
- [19] Leary, M. (2019). *Design for additive manufacturing*. Elsevier.
- [20] Gupta, A. K., & Taufik, M. (2021). The effect of process parameters in material extrusion processes on the part surface quality: A review. *Materials Today: Proceedings*.
- [21] Tyagi, S., Yadav, A., & Deshmukh, S. (2022). Review on mechanical characterization of 3D printed parts created using material jetting process. *Materials Today: Proceedings*, 51, 1012-1016.
- [22] Gibson, I., Rosen, D. W., Stucker, B., Khorasani, M., Rosen, D., Stucker, B., & Khorasani, M. (2021). *Additive manufacturing technologies* (Vol. 17). Cham, Switzerland: Springer.
- [23] Carlota, V. (2019, Oct 7). *The complete guide to electron beam melting (EBM) in 3d printing*. 3DNatives.
<https://www.3dnatives.com/en/electron-beam-melting100420174/#!>
- [24] ANSI-AWS A3.0-2001
- [25] Sarentica, A. (2019). Conventional heat treatment of additively manufactured AlSi10Mg.
- [26] Rosenthal, I., Stern, A., & Frage, N. (2014). Microstructure and mechanical properties of AlSi10Mg parts produced by the laser beam additive manufacturing (AM) technology. *Metallography, Microstructure, and Analysis*, 3(6), 448-453.
- [27] Rosenthal, I., Shneck, R., & Stern, A. (2018). Heat treatment effect on the mechanical properties and fracture mechanism in AlSi10Mg fabricated by additive

manufacturing selective laser melting process. *Materials Science and Engineering: A*, 729, 310-322.

[28] Tiwari, J. K., Mandal, A., Sathish, N., Agrawal, A. K., & Srivastava, A. K. (2020). Investigation of porosity, microstructure and mechanical properties of additively manufactured graphene reinforced AlSi10Mg composite. *Additive Manufacturing*, 33, 101095.

[29] Saba, N., Jawaid, M., & Sultan, M. T. H. (2019). An overview of mechanical and physical testing of composite materials. *Mechanical and physical testing of biocomposites, fibre-reinforced composites and hybrid composites*, 1-12.

[30] Princeton Edu (2022, June). *Notch, notch toughness*.

<https://www.princeton.edu/~maelabs/mae324/glos324/notch.htm>

[31] GuideByTips (2018, July 23). *Difference between izod and charpy impact test*.

<https://guidebytips.com/difference-between-izod-and-charpy-impact-test/>

[32] Girelli, L., Giovagnoli, M., Tocci, M., Pola, A., Fortini, A., Merlin, M., & La Vecchia, G. M. (2019). Evaluation of the impact behaviour of AlSi10Mg alloy produced using laser additive manufacturing. *Materials Science and Engineering: A*, 748, 38-51.

[33] Giovagnoli, M., Tocci, M., Fortini, A., Merlin, M., Ferroni, M., Migliori, A., & Pola, A. (2021). Effect of different heat-treatment routes on the impact properties of an additively manufactured AlSi10Mg alloy. *Materials Science and Engineering: A*, 802, 140671.

[34] *TS EN ISO 6892-1*

[35] *DIN 50125*

[36] *ASTM E8 – 04*

[37] Yilmaz, N. D., & Khan, G. A. (2019). Flexural behavior of textile-reinforced polymer composites. In *Mechanical and Physical Testing of Biocomposites, Fibre-Reinforced Composites and Hybrid Composites* (pp. 13-42). Woodhead Publishing.

[38] MechanicalC (2022, June). *Mechanical properties of materials*. <https://mechanicalc.com/reference/mechanical-properties-of-materials>

[39] Wei, P., Wei, Z., Chen, Z., Du, J., He, Y., Li, J., & Zhou, Y. (2017). The AlSi10Mg samples produced by selective laser melting: single track, densification, microstructure and mechanical behavior. *Applied surface science*, 408, 38-50.

[40] Yayla, P. (2019). *Kırılma mekaniği*. Birsen Yayinevi.

[41] Ansari, P., & Salamci, M. U. (2022). On the selective laser melting based additive manufacturing of AlSi10Mg: The process parameter investigation through multiphysics simulation and experimental validation. *Journal of Alloys and Compounds*, 890, 161873.

[42] SLM Solutions (2020, May). *Material data sheet*.

https://www.slm-solutions.com/fileadmin/Content/Powder/MDS/MDS_Al-Alloy_AlSi10Mg_0520_EN.pdf

- [43] Ngnekou, J. N. D., Nadot, Y., Henaff, G., Nicolai, J., Kan, W. H., Cairney, J. M., & Ridosz, L. (2019). Fatigue properties of AlSi10Mg produced by additive layer manufacturing. *International Journal of Fatigue*, 119, 160-172.
- [44] Tang, M., & Pistorius, P. C. (2019). Fatigue life prediction for AlSi10Mg components produced by selective laser melting. *International journal of fatigue*, 125, 479-490.
- [45] Raja, A., Cheethirala, S. R., Gupta, P., Vasa, N. J., & Jayaganthan, R. (2022). A Review on the Fatigue behaviour of AlSi10Mg alloy fabricated using Laser Powder Bed Fusion technique. *Journal of Materials Research and Technology*.
- [46] Paul, M. J., Liu, Q., Best, J. P., Li, X., Kruzic, J. J., Ramamurty, U., & Gludovatz, B. (2021). Fracture resistance of AlSi10Mg fabricated by laser powder bed fusion. *Acta Materialia*, 211, 116869.
- [47] Olympus Ims (2022, June). *Surface roughness measurement—parameters*. [https://www.olympus-ims.com/en/metrology/surface-roughness-measurement-portal/parameters/#!cms\[focus\]=cmsContent14708](https://www.olympus-ims.com/en/metrology/surface-roughness-measurement-portal/parameters/#!cms[focus]=cmsContent14708)
- [48] Macías, J. G. S., Elangeswaran, C., Zhao, L., Buffière, J. Y., Van Hooreweder, B., & Simar, A. (2021). Fatigue crack nucleation and growth in laser powder bed fusion AlSi10Mg under as built and post-treated conditions. *Materials & Design*, 210, 110084.
- [49] Syed, W. U. H., Pinkerton, A. J., & Li, L. (2005). A comparative study of wire feeding and powder feeding in direct diode laser deposition for rapid prototyping. *Applied surface science*, 247(1-4), 268-276.
- [50] Unionfab (n. d.). *Selective laser melting (SLM)*.
<https://www.unionfab.com/service/selective-laser-melting/>
- [51] Poligon Mühendislik (n. d.). *DLMS*.
<https://www.poligonmuhendislik.com/hizmetlerimiz/uretim/hizli-prototipleme/dmls>
- [52] Test-Equip (n. d.). *Micro vickers hardness tester*.
<https://www.testequip.com.au/micro-vickers-hardness-tester-future-tech-fm-series>
- [53] E Mat Tech (n. d.). *Aluminum Alloy*.
<https://emattech.com/aluminum-alloy/>
- [54] Marmara Edu (n. d.). *Basma Çekme Cihazı*.
http://dosya.marmara.edu.tr/eng/me/ekme_Cihaz_.pdf
- [55] Doc Player (n. d.). *Mmt310 malzemelerin mekanik davranışları*.

<https://docplayer.biz.tr/12701986-Mmt310-malzemelerin-mekanik-davranisi-1-deformasyon-ve-kirılma-mekanizmalarına-giriş.html>

[56] Lee, W. B. (Ed.). (2012). *Advances in engineering plasticity and its applications*. Elsevier.

[57] Material Properties (n. d.). *What is fracture of material*.

<https://material-properties.org/what-is-fracture-of-material-fracture-mechanics-definition/>

[58] Slide Serve (2014, Sep 22). *Failure of metals*.

<https://www.slideserve.com/neila/chapter-8-failure-of-metals>

[59] Inspection for Industry (n. d.). *What is destructive testing*.

<https://www.inspection-for-industry.com/destructive-testing.html>

[60] Spectrographic (n. d.). *Nikon epiphot metallurgical microscope*.

<https://spectrographic.co.uk/products/nikon-epiphot-metallurgical-microscope>

[61] Microscope Central (n. d.). *Nikon SMZ1500 Stereo Microscope*.

<https://microscopecentral.com/products/nikon-smz1500-stereo-microscope-on-post-stand-7-5x-112x>

[62] Sientro International Campus (n. d.). *Scanning electron microscope zeiss evo ma10*.

<https://www.ilsentierocampus.com/en/microscopy/scanning-electron-microscope/>

[63] Zyguła, K., Nosek, B., Pasiowiec, H., & Szysiak, N. (2018). Mechanical properties and microstructure of AlSi10Mg alloy obtained by casting and SLM technique. *World Scientific News*, 104, 456-466.

[64] Zhang, Z., Liu, M. Y., Breton, F., & Chen, X. G. (2018, June). Microstructure and mechanical properties of AlSi10Mg permanent mould and high pressure vacuum die castings. In *Proceedings of the 16th International Aluminum Alloys Conference (ICAA16), Montreal, QC, Canada* (pp. 17-21).